Towards Spin-Multiphoton Entanglement from a Quantum Dot

Master's Thesis

Written by *Simon Refshauge Pabst*

1st March 2021

Supervised by
Prof. Peter Lodahl & Dr. Alexey Tiranov

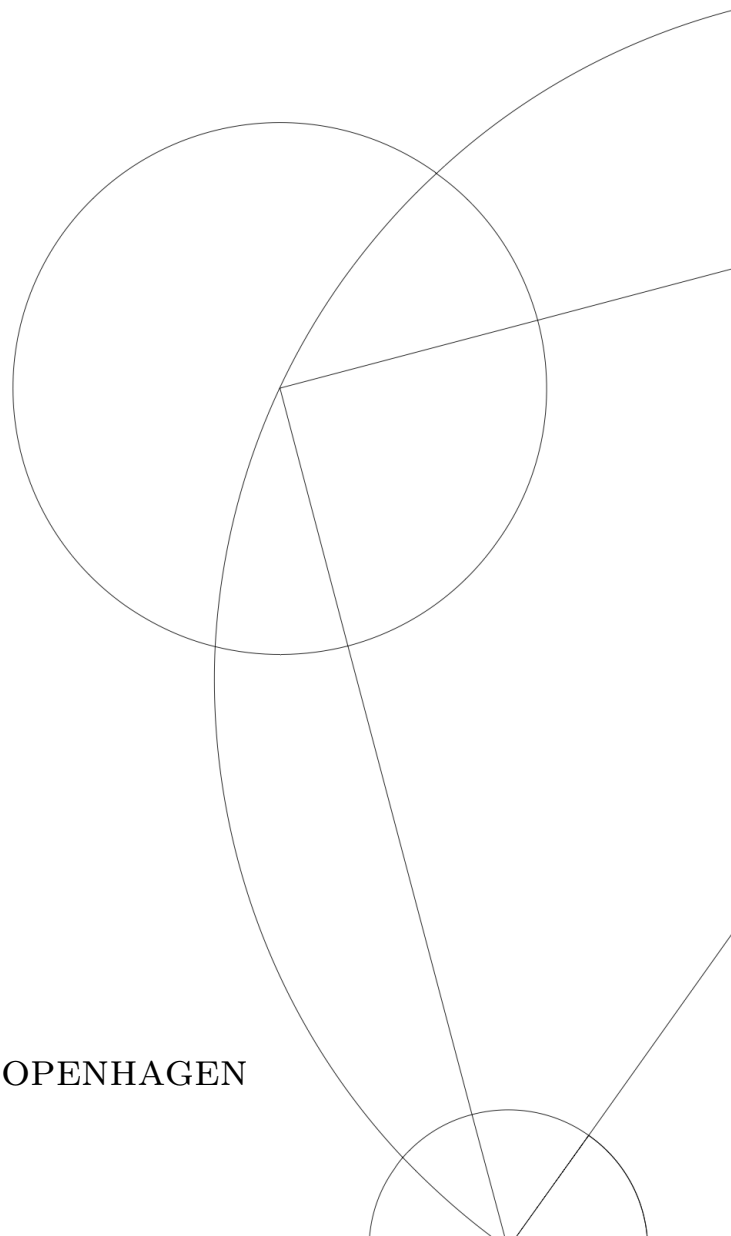

University of Copenhagen

UNIVERSITY OF COPENHAGEN

Faculty:	Faculty of Science
Institute:	Niels Bohr Institute
Department:	Quantum Photonics
Author:	Simon Refshauge Pabst
Email:	szl778@alumni.ku.dk

Title:	Towards Spin-Multiphoton Entanglement from a Quantum Dot

Supervisors:	Prof. Peter Lodahl & Dr. Alexey Tiranov
Handed in:	01.03.2021
Defended:	26.03.2021

Abstract

Over the past few decades, the field of quantum information has experienced an increasing interest owing to a wide range of new ideas and promising applications for future technologies. Based on the laws dictated by quantum mechanics, various protocols and quantum algorithms has been developed with the ability to solve problems more efficiently than its classical counterpart. In order to realize most of these proposals an essential tool is required, namely quantum entanglement.

In this thesis, the main ingredients towards spin-multiphoton entanglement will be presented, employing time-bin encoded photonic qubits and a hole-spin residing in a solid-state quantum dot embedded in a photonic crystal waveguide.

A theoretical introduction to spin manipulation schemes will be given, along with an outline of the photonic nanostructure making the positive trion X^+ a promising candidate for spin-photon entanglement. The main focus of the thesis concerns the creation and detection of the photonic qubits, using a self-stabilizing interferometer with the ability to scale the number of photons employed in an entanglement sequence. The quality of the single-photon emitter will be assessed by two parameters; the single-photon purity and the indistinguishability. The former yields a single-photon purity of $g^{(2)}(0) = 0.018 \pm 0.003$, while the latter demonstrates visibilities up to $\mathcal{V} = 95.5 \pm 0.7$ %, making the quantum dot a source of high-quality photons. All findings are presented in the context of an ideal multi-partite entanglement protocol generating GHZ- and one-dimensional Cluster-states.

Preface

This thesis is the product of 12 months of research carried out at the Niels Bohr Institute, University of Copenhagen, under the supervision of professor Peter Lodahl and Dr. Alexey Tiranov. It represents 45-ECTS points and is part of the requirements to achieve the Master of Science (M.Sc.) in Physics at the University of Copenhagen.

First and foremost, I would like to thank Peter Lodahl for the introduction to Quantum Optics back in 2018, and since then giving me the opportunity to write my thesis in the Quantum Photonics group. I would also like to express my sincere gratitude to Alexey Tiranov for the continuous assistance and guidance throughout the project. Furthermore, I would like to thank Martin Hayhurst Appel for sharing his immense knowledge about the laboratory and the many instructive discussions.
To my office mates, thank you for all the good times in FK10 and always creating a nice and enjoyable work environment.
I also wish to thank everyone in the Quantum Photonics group for the scientific talks and presentations, including those who has helped me during the last 12 months or otherwise given me constructive feedback.
Finally, I would like to thank my family and especially my girlfriend Laura for all the love and support you have shown me, not only during the last year, but throughout my entire time of study. Thank you!

Contents

Chapter 1

Introduction

Some of the most central and widely used theories in the field of physics, such as Newton's Mechanics or Einstein's Relativity, were mostly formulated by individuals. The development of Quantum Theory however, has been an ongoing venture lead by many great physicists. Particularly, during the last century numerous new discoveries has been made, including the probabilistic and quantized nature of systems at atomic scale - hence the name *Quantum* Mechanics. These new ideas initiated a paradigm shift in physics, where light now could be understood as quanta called *photons*, atoms having discrete energy levels and the fact that light-matter interactions are quantized.

In more recent years, starting around the early 1980s, proposals have been made whereby the use of quantum mechanical phenomena such as the superposition principle and entanglement could be utilized to make a quantum computer, which potentially could solve various problems more efficient than its classical counterpart [1]. A such device would operate on the principles of quantum mechanics, replacing the classical bit with a quantum bit, also known as a *Qubit* - a two-level quantum system. Many promising candidates have been considered, including Ion Trap Qubits, Superconducting Qubits and Quantum Dots (QDs) [1] - the latter being investigated in this thesis. Utilizing this modern technology governed by the laws of quantum mechanics, quantum cryptography[1] and quantum algorithms[2] has been proposed, enabling methods of secure data transfer and faster data processing [4].

Key ingredient towards realizing almost any operational quantum information processing system is the ability to manipulate, store and transfer information. As already alluded to, QDs have demonstrated to be useful candidates in this endeavour [5]. Utilizing the spin-state of an electron or hole residing in a QD, naturally constitutes a two-level quantum system, which can be manipulated through optical techniques [6]. However, realizing long distance quantum communication requires a robust way of transferring information, an obstacle which can be solved using photons. Linking the "stationary qubit", i.e. the spin-state in a QD, to a "flying" qubit, i.e. single photons, forms a promising system for

[1] The first quantum cryptography protocol was presented by Charles Bennett and Gilles Brassard in 1984. It is more commonly known as the BB84-Protocol [2].

[2] Some of the most well known quantum algorithms include Shor's integer factoring algorithm and Grover's search algorithm [3].

applications in quantum communication [6]. Central to most of these applications is the quantum phenomenon known as *entanglement*.

This thesis investigates the main ingredients towards spin-photon entanglement using time-bin encoded photonic qubits and the spin degree of freedom of a QD embedded in a photonic crystal waveguide. The theoretical framework for coherent spin manipulation will be introduced along with an analysis of a Time-bin Interferometer used to generate and detect the photonic qubits. These aspects will be presented in the context of an entanglement protocol enabling multi-photon entangled states. Furthermore, the properties of the QD operating as a single-photon source will be characterized, based on the single-photon purity and indistinguishability.

The outline of this thesis is as follows:

- *Chapter 2*: The theoretical background of the physical system containing the QD will be presented. This includes an introduction to excitation and charging schemes, together with a derivation of the optical selection rules. Furthermore, a brief description of the photonic nanostructure will be given with focus of the photonic crystal waveguide in which the QD is embedded. Finally, the concepts behind optical spin pumping and rotating will be reviewed, which makes up an essential part of the entanglement protocol.

- *Chapter 3*: This chapter seeks to give an introduction to quantum entanglement, with focus on multi-partite entangled state such as the *GHZ*- and *Cluster*-states. Furthermore, a protocol for sequential generation of time-bin entangled photons will be review along with a paragraph addressing the obstacles towards entanglement verification.

- *Chapter 4*: A theoretical and experimental characterization of the Time-bin Interferometer is presented, with focus on its application towards the generation of photonic qubits. The central figures of merit are derived, relating the main working principles of the interferometer to the entanglement protocol.

- *Chapter 5*: The properties of the optical excitation pulse will be investigated, followed by a characterization of the single-photon source. The latter includes an estimation of the single-photon purity using photon statistics together with an analysis of the indistinguishability based on two-photon interference.

- *Chapter 6*: The final conclusion and outlook is presented.

Chapter 2

Theoretical Background of the Physical System

This chapter seeks to give an introduction to a particular set of single-photon emitters, namely solid-state quantum dots (QDs). The latter is embedded in a photonic crystal waveguide which constitutes the physical system of the spin-qubit utilized for the entanglement protocol presented in this work. The advantageous properties of the photonic environment will be addressed along with techniques to excite and charge the QD. The final sections of this chapter includes a derivation of optical transition rules and spin manipulation schemes.

2.1 Introduction to Quantum Dots

A QD consists of several thousand atoms confined in a small dot-like shape spanning tens of nanometers. Its optical properties resemble that of a single atom, resulting in the nickname "artificial atom". This work will investigate solid-state QDs comprised of Indium Arsenide (InAs) dots embedded in Gallium Arsenide (GaAs). In comparison, both materials are part of the III-V semiconductor group, having direct bandgaps and same zinc-blende crystal structure [6].
The most common way of producing InGaAs QDs is through the Stranski-Krastanov method, where so-called self-assembled QDs are grown. Employing molecular-beam epitaxy, a thin membrane of InAs, also known as the *wetting layer*, is transferred onto a flat GaAs substrate [7]. After approximately 1.5 monolayers of InAs, the formation of small InAs-islands randomly form on the GaAs surface [6], see Fig. 2.1 (a). This process is a consequence of the mismatch in lattice constants between the two materials as InAs has a 7% larger lattice constant than GaAs, which introduces strain to the local system. Eventually islands of self-assembled QDs form, whereby the binding energy is minimized. Stranski-Krastanov QDs are generally pyramid-shaped with spatial-dimensions ranging from $1 - 10$ nm in height and $10 - 70$ nm in-plane. Due to different bandgap energies between the QD and its surrounding medium, quantum confinement of electrons is achievable, yielding discrete energy levels along the growth/z-direction, see Fig. 2.1 (b). This is analogous to the well-known finite potential well. Typically, the wavelength of the low-energy transition of InAs dots are around 850-1000 nm, depending on the size and specific composition [5].

Protecting the QDs from oxidation and unwanted interaction with the environment, a capping layer of GaAs is grown on top. Finally, the system is embedded into a *p-i-n* diode structure, placing doped layers above and below the sample, allowing an electric field to be applied across the QD [7]. This enables both deterministic charging of the QD and tuning of resonance frequency due to the Quantum-confined Stark effect [8]. For good coherence properties, most experiments using QDs are carried out at liquid helium temperatures ($\approx$ 4 Kelvin), thus reducing thermal noise including the suppression of phonon interactions.

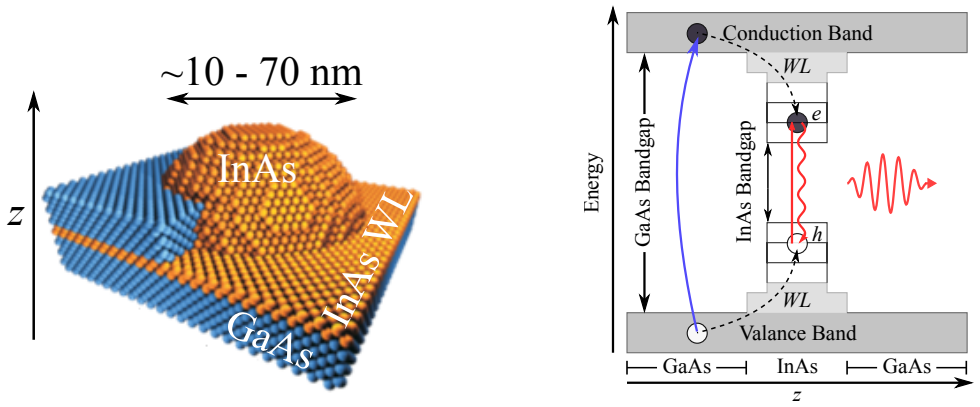

(a) Island shaped QD.

(b) Excitation schemes.

Figure 2.1: (a) Quantum dot consisting of a InAs dot embedded in GaAs. The flat layer in between GaAs is the wetting layer (WL). (b) The formation of a potential well with discrete energy levels in both the conduction- and valence-band due to the difference in bandgap-energy between GaAs and InAs. ABB- and resonant-excitation illustrated by the blue and red arrow, respectively. The former excites an electron residing in the surrounding material and decays non-radiatively into the potential well. In both cases, a photon is emitted upon recombination. Illustration on the left from Ref. [9], with slight modifications.

2.1.1 Excitation and Charging of Quantum Dots

Optical excitation of a QD can be achieved through various techniques, depending on the frequency of the incoming light. In the case of an incident photon with a frequency matching the energy difference between the valence- and conduction band, *resonant excitation* is achievable, see Fig. 2.1 (b). During this process, an electron residing in the valence band is excited to the lowest conduction band, creating an electron–hole pair [5]. Upon recombination a photon is emitted, a process know as *resonance fluorescence* (RF). Due to the larger bandgap energy of GaAs, the emitted photon can propagate freely through the material. Increasing the excitation frequency further, the QD is excited to a higher energy state, i.e. an excited excitonic state - a process known as *quasi-resonant* excitation (or sometimes *p-shell* excitation - analogous to the convention in atomic physics).
Finally an *above-band-gap* (ABB) laser can be employed, shown as the blue arrow in Fig. 2.1 (b). Here the laser-frequency is comparable with the bandgap energy of the surrounding material (GaAs in this case), thus exciting a nearby electron. Through non-radiative decay the electron eventually falls back into the potential well of the QD.

The creation of an electron–hole pair is known as a *neutral exciton* X^0, having *lifetimes*, i.e. the average time before recombination, of approximately 1 ns in bulk [10]. Both ABB- and resonant-excitation will be utilized for the entanglement protocol presented in this thesis.

Next to consider is the charging of a neutral QD, i.e. a system containing fully occupied states in the valence band and an empty conduction band.
Loading the neutral QD with an additional electron in the conduction band, makes the system negatively charged. Through optical excitation, one may excite an additional electron to the conduction band, creating a *negative trion* X^-, consisting of two electrons and a hole. Likewise, the system becomes positively charged, if an electron is removed from the valence band of a neutral QD. This results in the creation of a *positive trion* X^+ upon excitation, composed of two holes and an electron. Experimentally, this can be realized through the use of an ABB-laser and tuning the bias voltage V_{Bias} across the *p-i-n* diode structure, briefly introduced in previous section.
A detailed description of the diode structure is beyond the scope of this thesis, however the main idea in regards to QD charging can be understood by considering Fig. 2.2 (a). Here, the energy level of the conduction band can be adjusted with respect to the Fermi surface, by altering the bias voltage V_{Bias} across the QD [8]. Thus, lowering the conduction band below the Fermi energy, enables a single electron to occupy the conduction band, whereby the QD becomes negatively charged. Due to the Coulomb force additional electrons are repelled, a phenomenon known as *Coulomb Blockade* [8]. However, increasing the bias voltage further and thereby overcoming the coulomb blockade, the QD can be charged with additional electrons. The same principle applies for positive charging, except the bias voltage is lowered instead, thus raising the valence band above the Fermi energy level.

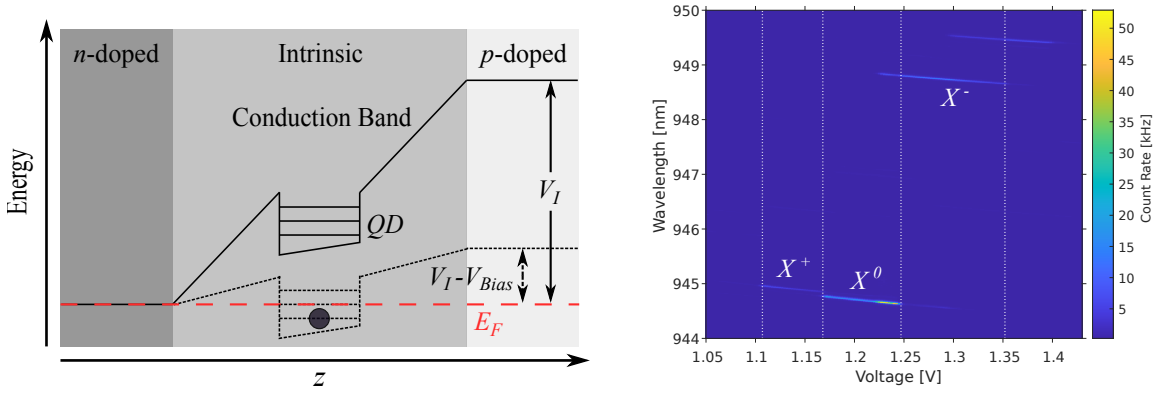

(a) Charging of QD.

(b) QD spectrum at varying bias voltages.

Figure 2.2: (a) Charging scheme for a QD in a *p-i-n* diode structure. The QD is neutral, when no external voltage is applied. Tuning the bias voltage V_{Bias}, and thereby altering the energy bands in respect to the Fermi energy level E_F, allows charging of the QD. (b) Photoluminescence spectrum from the QD as a function of the applied bias voltages. The positive trion X^+ under consideration in this thesis can be optically excited in the range of $V_{Bias} \approx 1.1 - 1.17$ V, emitting photons at wavelengths around 945 nm. Figure (b) is reproduced from Supplementary Material of Ref. [11], with slight modifications.

Figure 2.2 (b) shows the photoluminescence from the QD utilized in this thesis, where the QD is excited by a laser tuned to its p-shell resonance at 924.4 nm[1]. Dependent on the applied bias voltages, the spectrum of the photoluminescence changes. Looking closely, four distinct plateaus emerge, three of them being of interests to the charging scheme discussed above. Centered around $V_{Bias} \approx 1.2$ V the X^0 appears, while the X^+ (X^-) becomes visible for lower (higher) voltages. Due to a larger effective dephasing time T_2^*, the hole-spin, that is X^+, constitutes the physical system used for the entanglement protocol studied in this work[2]. A further investigation of the X^+ properties will be presented in Section 2.2.1.

2.1.2 Optical Transition and Selection Rules

Utilizing a QD as a single-photon source, requires knowledge about the optical transitions and their respective selection rules. As a result, a slightly more comprehensive description of the valence- and conduction-band is required.
In most III-V semiconductors the valence band is split into three degenerate sub-bands at the Γ-point, i.e. for wavevector $\vec{k} = 0$. Each band is defined by its total angular momentum J and the corresponding z-projection J_z. Thus, transitions to the lowest conduction (C) band ($J = 1/2$, $J_z = \pm 1/2$) are possible from

(i) The Heavy-hole (HH) band ($J = 3/2$, $J_z = \pm 3/2$),

(ii) The Light-hole (LH) band ($J = 3/2$, $J_z = \pm 1/2$),

(iii) The Split-off (SO) band ($J = 1/2$, $J_z = \pm 1/2$),

which are all depicted in Fig. 2.3. As a consequence of the spin-orbit interaction, the energy of the SO-band is suppressed by the spin-orbit splitting energy Δ_{SO}, thus partially lifting the degeneracy[3] [6]. In the following, the SO-band will be neglected, since it is non-crucial for the further analysis.

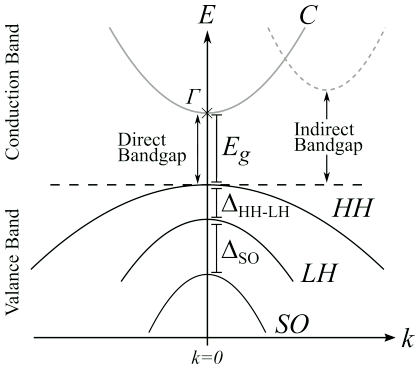

Figure 2.3: Bandstructure for a QD as a function of the energy E and wavevector $\vec{k}$. The maximum (minimum) of the valence (conduction) band are located at the Γ-point, i.e. at $\vec{k} = 0$. The degeneracy of the valence bands are lifted due to the spin-orbit splitting energy Δ_{SO} and the strain induced in the QD, Δ_{HH-LH}.

[1] See supplementary material in Ref. [11] for more information.

[2] Experiments reveal that the electron spin is more sensitive to the nuclear spin bath, having T_2^*-times of just a few nano-seconds [6].

[3] According to Ref. [12], the spin-orbit splitting energy is in the order of ≈ 0.34 eV for GaAs.

The remaining two bands (HH and LH) are degenerate in bulk, but due to the induced strain and strong vertical confinement in the QD, the degeneracy is lifted by $\Delta_{HH-LH} > 10$ meV [13], lowering the energy of the light-hole band as shown in Fig. 2.3. Thus, the minimal energy transitions arise from the heavy-hole band located nearest to the Fermi level, to the lowest conduction band. However, a small coupling to the light-hole band may occur, known as hole-mixing[4].

In order to derive the optical selection rules, the electron (or hole) wavefunction is required. In a heterojunction, such as InGaAs QD embedded in GaAs, the wavefunctions can be derived using the *envelope function formalism* [14].
In this formalism the electron/hole wavefunction contains a rapidly varying *Bloch* function modulated by an *envelope* function, the latter obeying the effective mass equation. The Bloch functions arise from the periodic potential in the crystal lattice, while the envelope function is a result of a slowly varying perturbation of the crystal lattice potential [5]. Denoting the envelope function $|F_n\rangle$ and the Bloch function $|u_{n,k}\rangle$, the wavefunction of an electron (or hole), is given by

$$|\psi_n\rangle = |F_n\rangle\,|u_{n,0}\rangle\,|\alpha_n\rangle\,, \tag{2.1.1}$$

where the Bloch function is evaluated at $\vec{k} = 0$, $|\alpha_n\rangle$ is the spin-state of the electron/hole and the subscript $n = \{c, v\}$ denotes the conduction- and valence-band, respectively.
Estimating the shape, i.e. the symmetry or parity, of the Bloch functions is sufficient in regards to the selection rules. The Bloch functions possesses the same symmetry as the atomic orbitals, meaning that the conduction band is formed from s-type orbitals (i.e. *even* functions) while the valence band is formed from a linear combination of p-type orbitals [5]. Defining the electron's wavevector to be oriented along the z-direction, the Bloch functions (incl. spin-state) for the HH- and conduction-band are

$$|u_{HH,0}\rangle_z\,|\alpha_v\rangle = |J = 3/2, J_z = 3/2\rangle\,|\uparrow\rangle = -\frac{1}{\sqrt{2}}\left(|u_x\rangle + i\,|u_y\rangle\right)|\uparrow\rangle\,, \tag{2.1.2}$$

$$|\bar{u}_{HH,0}\rangle_z\,|\bar{\alpha}_v\rangle = |J = 3/2, J_z = -3/2\rangle\,|\downarrow\rangle = \frac{1}{\sqrt{2}}\left(|u_x\rangle - i\,|u_y\rangle\right)|\downarrow\rangle\,, \tag{2.1.3}$$

$$|u_{c,0}\rangle_z\,|\alpha_c\rangle = |J = 1/2, J_z = 1/2\rangle\,|\uparrow\rangle = |u_s\rangle\,|\uparrow\rangle\,, \tag{2.1.4}$$

$$|\bar{u}_{c,0}\rangle_z\,|\bar{\alpha}_c\rangle = |J = 1/2, J_z = -1/2\rangle\,|\downarrow\rangle = |u_s\rangle\,|\downarrow\rangle\,, \tag{2.1.5}$$

where $|u_s\rangle$ denotes functions with even parity in all directions, while $|u_x\rangle$ and $|u_y\rangle$ expresses odd parity in the x/y-direction. Furthermore, $|\alpha_n\rangle$ and $|\bar{\alpha}_n\rangle$ indicate spin-up and spin-down, respectively.
In the dipole approximation, the minimal-coupling Hamiltonian inducing optical transitions can be written as [5]

$$\hat{H}(\vec{r}_0, t) = -\frac{q}{m_e}\hat{p}\cdot\vec{A}(\vec{r}_0, t), \tag{2.1.6}$$

where $\hat{p} = -i\hbar\boldsymbol{\nabla}$ is the momentum operator and $\vec{A}(\vec{r}_0, t)$ is the vector potential of the E-field evaluated at position $\vec{r}_0$. Furthermore, q is the elementary charge and m_e the electron

[4]Hole-mixing will briefly be discussed at the end of this section. Otherwise, it will be neglected throughout this thesis.

rest mass. The transition between two states is therefore given by

$$\langle \psi_f | \, \hat{H}(\vec{r}_0, t) \, | \psi_i \rangle \propto \langle F_f | F_i \rangle \, \langle u_f | \, \hat{p} \cdot \vec{A}(\vec{r}_0, t) \, | u_i \rangle \, \langle \alpha_f | \alpha_i \rangle \tag{2.1.7}$$

$$= \langle F_f | F_i \rangle \, \vec{A}(\vec{r}_0, t) \cdot \langle u_f | \, \hat{p} \, | u_i \rangle \, \langle \alpha_f | \alpha_i \rangle \, , \tag{2.1.8}$$

where the slowly varying envelope function is unaffected by the momentum operator, hence only contributes to the transition amplitude. From Eq. 2.1.8 a general set of optical selection rules appears

(i) The Envelope functions must have same parity,

(ii) The Bloch functions must have opposite parity,

(iii) Spin most remain unchanged.

In order to derive the specific selection rules for a given state, the matrix element $\langle u_f | \, \hat{p} \, | u_i \rangle$ requires further investigation. Thus, a few symmetry relations and definitions regarding the momentum operator $\hat{p}$ acting on the Bloch functions are useful. They can be summarized to [12]

$$(1) \qquad \langle u_s | \, \hat{p}_i \, | u_j \rangle = 0, \qquad \text{for } i \neq j, \tag{2.1.9}$$

$$(2) \qquad \langle u_s | \, \hat{p} \, | u_i \rangle = \langle u_s | \, \hat{p}_i \, | u_i \rangle \equiv \mathcal{P}, \tag{2.1.10}$$

$$(3) \qquad \langle u_s | \, \hat{p} \, | \bar{u}_i \rangle = 0, \tag{2.1.11}$$

where $i = \{x, y, z\}$ and $\mathcal{P}$ is the *momentum matrix element*, a quantity defined by the bulk semiconductor. The second and third relation are directly related to (ii) and (iii) specified in the general selection rules. The specific optical transition rules for a given spin-state residing in the valence band, can now be derived.
For an electron with spin-up $|\uparrow\rangle$ residing in the *HH*-band, the optical transition rule to the conduction band is therefore given by

$${}_z\langle \alpha_c, u_c | \hat{H}(\vec{r}_0, t) \, | u_{HH}, \alpha_v \rangle_z \propto -\frac{1}{\sqrt{2}} \, \langle \uparrow | \, \langle u_s | \, \hat{p}(|u_x\rangle + i \, |u_y\rangle) \, | \uparrow \rangle \tag{2.1.12}$$

$$= -\frac{1}{\sqrt{2}} \, (\langle u_s | \, \hat{e}_x \hat{p}_x + \hat{e}_y \hat{p}_y + \hat{e}_z \hat{p}_z (|u_x\rangle + i \, |u_y\rangle)) \tag{2.1.13}$$

$$= -\frac{1}{\sqrt{2}} \, (\langle u_s | \, \hat{e}_x \hat{p}_x \, | u_x \rangle + \langle u_s | \, i \hat{e}_y \hat{p}_y \, | u_y \rangle)) \tag{2.1.14}$$

$$= -\frac{\mathcal{P}}{\sqrt{2}} \, (\hat{e}_x + i \hat{e}_y) \, , \tag{2.1.15}$$

where $\hat{e}_{i=\{x,y,z\}}$ are Cartesian units vectors. From Eq. 2.1.15, the transition has a circularly polarized dipole moment. In this particular case, the polarization is left-handed, σ^+.
For spin-down $|\downarrow\rangle$ the matrix element takes the form

$${}_z\langle \bar{\alpha}_c, \bar{u}_c | \, \hat{H}(\vec{r}_0, t) \, | \bar{u}_{HH}, \bar{\alpha}_v \rangle_z \propto \frac{\mathcal{P}}{\sqrt{2}} \, (\hat{e}_x - i \hat{e}_y) \, , \tag{2.1.16}$$

resulting in right-handed polarization, σ^-. Additionally, due to the third selection rule regarding spin-conservation, the following two transitions are not allowed

$$ {}_z\langle\bar{\alpha}_c, \bar{u}_c|\, \hat{H}(\vec{r}_0, t)\, |u_{HH}, \alpha_v\rangle_z = {}_z\langle\alpha_c, u_c|\, \hat{H}(\vec{r}_0, t)\, |\bar{u}_{HH}, \bar{\alpha}_v\rangle_z = 0, \tag{2.1.17} $$

since $\langle\downarrow|\uparrow\rangle = \langle\uparrow|\downarrow\rangle = 0$.

Until now, the derivation of the optical selection rules has been restricted to neutral excitons. However, as discussed in Section 2.1.1, charging of QDs can be realized through e.g. ABB-excitation. As a consequence of the Pauli exclusion principle, two quasi-particles with same spin cannot occupy the same state in either the conduction or valence band.
Thus, in the ideal case where no hole-mixing occurs, the selection rules from the HH-band can be summarized to

$$ \text{(i)} \qquad |\uparrow\rangle_z \overset{\sigma^+}{\longleftrightarrow} |\uparrow\downarrow, \Uparrow\rangle_z \qquad \text{and} \qquad |\downarrow\rangle_z \overset{\sigma^-}{\longleftrightarrow} |\uparrow\downarrow, \Downarrow\rangle_z\,, \tag{2.1.18} $$

$$ \text{(ii)} \qquad |\Downarrow\rangle_z \overset{\sigma^+}{\longleftrightarrow} |\Uparrow\Downarrow, \downarrow\rangle_z \qquad \text{and} \qquad |\Uparrow\rangle_z \overset{\sigma^-}{\longleftrightarrow} |\Uparrow\Downarrow, \uparrow\rangle_z\,, \tag{2.1.19} $$

for (i) an electron or (ii) a hole residing in the heavy-hole valence band [6], where $\Uparrow$ ($\Downarrow$) denotes hole spin-up(down). Hence, only vertical transitions are allowed, while the diagonal/cross transitions are suppressed, see Fig. 2.4 (a).
As a final remark, it should be noted, that including the LH-component from the valence band, the diagonal transitions given by

$$ |\uparrow\rangle_z \longleftrightarrow |\uparrow\downarrow, \Downarrow\rangle_z \qquad \text{and} \qquad |\downarrow\rangle_z \longleftrightarrow |\uparrow\downarrow, \Uparrow\rangle_z\,, \tag{2.1.20} $$

are weakly allowed, due to hole-mixing [6]. In addition to this, the Zeeman splitting energy Δ_{Zm}, induced by an external magnetic field, is much smaller than the heavy-light-hole splitting ($\Delta_{Zm} \ll \Delta_{HH-LH}$) for any realistic experiment [13]. It can thus be assumed, that hole-mixing in independent of the magnitude of the B-field. A further analysis of hole-mixing is beyond the scope of this thesis, and henceforth only transitions from the HH-band will be considered.

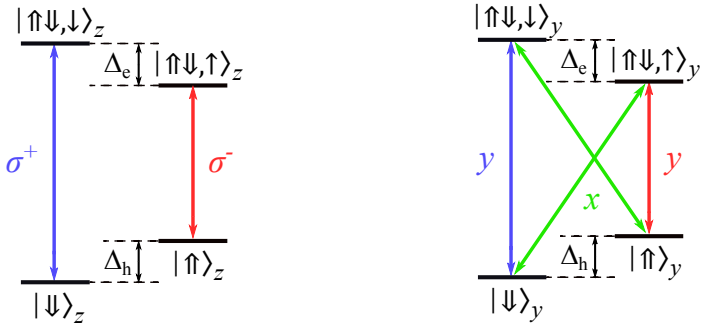

(a) Faraday geometry. (b) Voigt geometry.

Figure 2.4: Optical selection rules for a positive trion X^+, with hole(electron) energy splitting $\Delta_h(\Delta_e)$, due to an external magnetic field. (a) Selection rules in Faraday geometry, where *only* the vertical transitions are allowed, using circular polarized light. (b) Selection rules in Voigt geometry ($\vec{B} = B_y$), where the both vertical *and* diagonal transitions are accessible by y- and x-polarized light, respectively.

Optical Selection Rules in Voigt Geometry

So far, the optical selection rules were derived with an underlying assumption of an out-of-plane magnetic field oriented along with the Bloch functions, i.e. in the z/growth-direction of the QD. This configuration is also known as *Faraday* geometry, lifting the otherwise degenerate electron (or hole) pairs, due to the *Zeeman*-effect. However, the optical selection rules depend on the orientation of external magnetic field. For the purposes of this work, an in-plane magnetic field will be utilized, known as *Voigt* geometry. More precisely, the B-field is oriented in the y-direction whereby the eigenstates of the spin in the y-basis becomes a mixture of the eigenstates in the z-direction [6].
Consequently, the allowed transitions for a hole spin residing in the *HH*-valence band are expressed by

$$|\Downarrow\rangle_y \overset{y}{\longleftrightarrow} |\Uparrow\Downarrow,\downarrow\rangle_y \qquad \text{and} \qquad |\Uparrow\rangle_y \overset{y}{\longleftrightarrow} |\Uparrow\Downarrow,\uparrow\rangle_y\,, \tag{2.1.21}$$

for the vertical transitions, whereas the diagonal transitions are given by

$$|\Downarrow\rangle_y \overset{x}{\longleftrightarrow} |\Uparrow\Downarrow,\uparrow\rangle_y \qquad \text{and} \qquad |\Uparrow\rangle_y \overset{x}{\longleftrightarrow} |\Uparrow\Downarrow,\downarrow\rangle_y\,, \tag{2.1.22}$$

using the formalism developed in previous section. These transitions are depicted in Fig. 2.4 (b), along with the energy level diagram of the X^+.

In summary, the optical transitions rules in Voigt geometry differ from Faraday geometry in two distinct ways. Firstly, the transitions are no longer accessible by circular polarized light, but linear polarization has to be applied instead. Secondly and most importantly, the diagonal transitions are now allowed. The latter will come in handy once spin-flip processes has to be implemented, which will be discussed in Section 2.3, since it plays an important role in regards to the pulse sequence utilized for spin-photon entanglement.

2.2 Photonic Nanostructures

A central advantage of self-assembled semiconductor QDs is the efficient integration into photonic nanostructures. Numerous photonic nanostructures exists, including photonic cavities and nanophotonic waveguides - the latter being of interest in this work. Embedding semiconductor QDs into nanophotonic waveguides enables manipulation of light-matter interactions and routing of photons [5], which forms a promising system for many applications.

The projected Local Density of Optical States (LDOS) is a central quantity affecting the local light-matter interaction, including the spontaneous emission rate. In general, the density of optical states is a measure of optically accessible modes in a certain infinitesimal frequency range, i.e. between ω and $\omega + d\omega$. The LDOS is highly dependent on the orientation of the transition dipole moment $\hat{e}_d$ and the position of the emitter $\vec{r}_0$ in respect to the photonic nanostructure. Mathematically, the LDOS defines the total number of optical states at frequency ω, summarized over all available modes $\mathbf{k}$ with eigenfrequency $\omega_{\mathbf{k}}$, which takes the form

$$\rho(\vec{r}_0, \omega, \hat{e}_d) = \sum_{\mathbf{k}} |\hat{e}_d \cdot \vec{u}^*_{\mathbf{k}}(\vec{r}_0)|^2 \, \delta(\omega - \omega_{\mathbf{k}}), \tag{2.2.1}$$

where $\vec{u}_{\mathbf{k}}(\vec{r}_0)$ denotes normalized Bloch functions in which the electric field is expanded [5]. From Eq. 2.2.1, it becomes apparent that the LDOS is conditioned on the dipole moment projected onto the direction of the electric field - hence the name. Based on the LDOS, an expression for the spontaneous decay rate can be derived, which is proportional to

$$\gamma_{rad}(\vec{r}_0, \omega, \hat{e}_d) \propto |\langle u^*_{HH}| \mathbf{r} |u_c\rangle|^2 |\langle F^*_{HH}|F_c\rangle|^2 \rho(\vec{r}_0, \omega, \hat{e}_d), \tag{2.2.2}$$

where $\langle u^*_{HH}| \mathbf{r} |u_c\rangle$ is the dipole matrix element between the conduction- and *HH*-band, while F denotes the slowly-varying envelope functions, previously introduced in Section 2.1.2. The resulting emission spectrum becomes Lorentzian, with a central frequency ω and a Full-Width-of-Half-Maximum (FWHM) of γ_{rad}.
Thus, the ability to tailor and engineer photonic nanostructures and thereby modifying the environment, i.e. LDOS, effectively alters the radiative process of the emitter. This phenomenon is also known as the *Purcell Effect* and its significance to the decay rates of the X^+ will become apparent in the following section.

2.2.1 Photonic Crystal Waveguide

In general, a photonic crystal (PhC) consists of an inhomogeneous dielectric medium with a periodic structure, effectively varying the refractive index on length scales determined by the optical wavelength [5]. Typically, photonic crystals are made from semiconductor materials, e.g. Gallium Arsenide (GaAs) or Silicon (Si), having large refractive indices, $n \approx 3.5$ [5]. Introducing periodic pattern of air holes ($n_{\text{air}} \approx 1$) into a N-dimensional ($N = \{1, 2, 3\}$) structure of e.g. GaAs, causes Bragg reflection - mimicking that of a Bragg mirror. Thus, a certain range of frequencies are prevented from propagating, resulting in the creation of a *photonic bandgap*. A more comprehensive description of PhCs can be found in Section III of Ref. [5], however, this work will be restricted to a two-dimensional PhC - more precisely a membrane of GaAs confined to the xy-plane, and hence no periodicity in the z-direction.

Introducing a 1D line-defect, i.e. a row of missing air holes, in the GaAs PhC membrane results in a *Photonic Crystal Waveguide* (PCW). The PCW allows for discrete modes, residing within the photonic bandgap and thus confined due to the Bragg reflection, to propagate along the line-defect. Placing an emitter inside the PCW is thus advantageous, since it enables photon routing whilst enhancing the waveguide mode coupling, due to the photonic environment.
The corresponding coupling efficiency is generally described by the so-called β-factor. Letting γ_{WG} be the rate of spontaneous photon emission into the desired waveguide mode, the β-factor reads

$$\beta(\omega) = \frac{\gamma_{WG}}{\gamma_{WG} + \gamma_{Loss}}, \tag{2.2.3}$$

where $\gamma_{Loss} = \gamma_{ng} + \gamma_{nrad}$ is the total decay rate into undesired modes [5]. Here γ_{ng} denotes the decay rate into non-guided modes, while γ_{nrad} is the rate of intrinsic non-radiative recombination. Near unity β-factors have been demonstrated for PCWs [15], which also constitutes the physical setup enclosing the QD studied in this work - the topic of the following section.

Positive Trion in a PCW

The QD used in this study is an InGaAs dot manufactured by the Stranski-Krastanov method which is kept at 4 K using an attoDRY 1000 Cryostat from Attocube [16]. This cryostat is equipped with vector magnet, whereby each component of the magnetic field can be controlled individually[5]. In other words, one can choose between Faraday- or Voigt-geometry by adjusting the vector magnet. Furthermore, one may alter the bias voltage due to the *p-i-n* diode structure and hence charge the QD. Experimentally however, it turns out that solely altering the bias voltage is not sufficient for the creation of X^+. An ABB-laser has to be employed, once the bias voltage is tuned to the right interval, recall Fig. 2.2 (b). In this particular case, the ABB-laser is tuned to a wavelength of 830 nm and applied over a duration of 100 ns in order to initialise X^+ whereby the electron closet to the Fermi surface is removed from the local system.

The photonic nanostructure, in which the QD is embedded, consists of a two-sided PCW with grating couplers at each end, see Fig. 2.5. The gratings enables in- and out-coupling of the light propagating within the PCW. However, for the purposes of this work, the QD is solely excited from above, i.e. free space excitation, focusing the laser directly onto the QD. The corresponding selection rules for a positively charged QD in Voigt geometry has already been studied in Section 2.1.2, but the effects of the PCW is yet to be investigated. This has been done by M.H. Appel *et al.* [11] (2021), examining the spin-photon interface of this specific QD. Thus, an extensive treatment on the properties and effects of the photonic environment will be omitted here, as it is beyond the scope of this study.
Nonetheless, it is worth discussing one crucial figure of merit, namely the *cyclicity* - here defined as the ratio between the decay rates of the x- and y-polarized linear dipoles, $C = \gamma_y/\gamma_x$. In bulk these are identical, yielding a cyclicity of $C = 1$. However, as stated in Section 2.2 the photonic environment of the PCW may selectively enhance or suppresses the decay rates - a property utilized in this work.

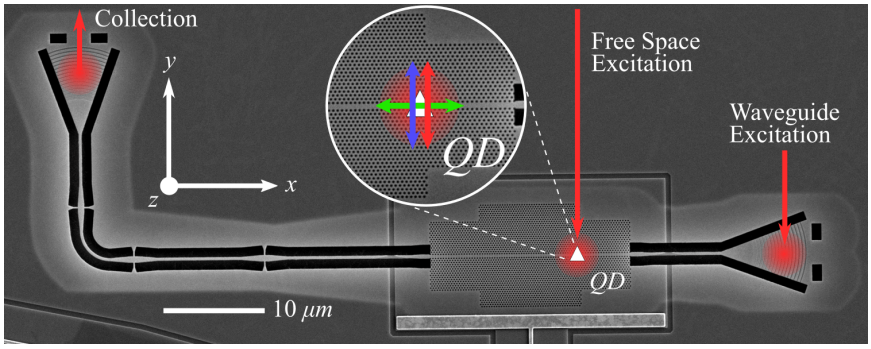

Figure 2.5: Scanning electron microscope image of a two-sided PCW, with grating couplers at each end. The QD is excited from free space, while the QD fluorescence is collected by the grating coupler on the left. The ideal orientation of the linear dipoles are shown in the circular insert. Note, the color-coding of the linear dipoles is equivalent to the transitions shown in Fig. 2.4 (b). Image: Ref. [11], with slight modifications.

[5]A total of ±5 T in the z-direction (out-of-plane) and ±2 T in x- and y-direction (in-plane) can be achieved, while no more than a total of 2 T can be reached if either the x- or y-component is active.

As it will become apparent in Section 2.3, Voigt geometry is required in order to perform coherent spin rotations. As a consequence, vertical and diagonal transitions are accessible, as opposed to Faraday geometry. Thus, if one wishes to drive a specific transition, without the population decaying to an unwanted state, a high cyclicity is necessary.
From Ref. [11], the cyclicity of X^+ is estimated to $C^{(+)} = \gamma_y/\gamma_x \approx 15$ in Voigt geometry, making it a well-suited candidate for the entanglement protocol presented in the next Chapter[6]. Along with the cyclicity, several other important properties of X^+ are summarized in Table 2.1, which will be introduced in the chapters to come.

Properties of Charged QD in PCW	X^+
Cyclicity, $C = \gamma_y/\gamma_x$	$C^{(+)} = 14.7 \pm 0.2$
Lifetime of Charged QD, Γ	$\Gamma^{(+)} > 16$ μs
Radiative Decay Rate, γ_0	$\gamma_0^{(+)} = (3.07 \pm 0.06)$ ns^{-1}
Effective Dephasing Time, T_2^*	$T_2^{*(+)} = (21.4 \pm 0.7)$ ns
Central Frequency, ν_0	$\nu_0^{(+)} = 317.23$ THz
Linewidth (FWHM), $\Delta\nu_0$	$\Delta\nu_0^{(+)} = 1045$ MHz
Ground state splitting, Δ_h	$\Delta_h^{(+)} = 7.29$ GHz
Spin Pumping Fidelity, F_{SP}	$F_{SP}^{(+)} = 98.6\%$
Spin Rotation Fidelity, $F_{SR,\pi}$	$F_{SR,\pi}^{(+)} = 91\%$

Table 2.1: This table provides an overview of the properties of the X^+ embedded in a PCW with an in-plane magnetic field in the y-direction. All values are from Ref. [11], characterizing the specific QD utilized in this thesis.

2.3 Spin Manipulation and Dynamics

In this section, the main focus will be directed towards the manipulation and dynamics of the hole-spin, which constitutes the "stationary" qubit employed in the spin-photon entanglement protocol presented in the following chapter. In the context of qubits, the hole-spin $|\Uparrow\rangle$ ($|\Downarrow\rangle$) corresponds to logical $|0\rangle$ ($|1\rangle$) or vice versa. Thus, the state describing the spin-qubit can be expressed by a superposition between the two ground states of the X^+, taking the form

$$|\psi\rangle = \cos(\theta/2)\,|\Uparrow\rangle + \sin(\theta/2)e^{i\phi}\,|\Downarrow\rangle\,, \tag{2.3.1}$$

where $0 \leq \theta \leq \pi$ alters the probability amplitude and $0 \leq \phi < 2\pi$ defines the relative phase between the two states. Geometrically, a two-level quantum system is typically represented by a vector mapping out a sphere of unit radius - the so-called *Bloch sphere*, see Fig. 2.6. The surface of the sphere corresponds to *pure* states, whereas the interior represents *mixed* states[7].

[6] See Section 3.3 for the specific protocol.
[7] Pure- and mixed-states will be introduced in Section 3.1.

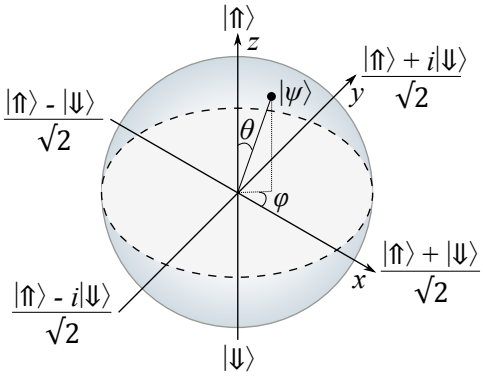

Figure 2.6: A geometrical representation of the two-level spin-state using the Bloch sphere (or sometimes in the context of optics, Poincaré sphere). The sphere has unit radius and the total quantum state is given by $|\psi\rangle$, uniquely defined by θ and ϕ.

Crucial for any qubit is the ability to initialize, manipulate and read-out the given state. The focus of this section is the realization of these processes, through the use of *Optical Spin Pumping* (OSP) and *Raman* transitions. The former will be utilized for spin initialization and read-out, while the latter enables spin rotation and thereby alter the amplitude and phase parameter by rotating θ and ϕ, respectively.

2.3.1 Optical Spin Pumping

In this section the concept behind optical spin pumping will be presented, with special focus on a positively charged trion X^+ embedded in a PCW, since this constitutes the physical system under consideration in this work. In Section 2.1.2 the optical transition rules were discussed for both Faraday and Voigt geometry, the latter being employed in this thesis.

Applying an in-plane magnetic field, i.e. Voigt geometry, makes the vertical transitions accessible by linear polarized light, while splitting the hole and trion levels due to the Zeeman effect. Consequently, a four-level system appears, where the resulting energy levels and transitions can be summarized by Fig. 2.7.

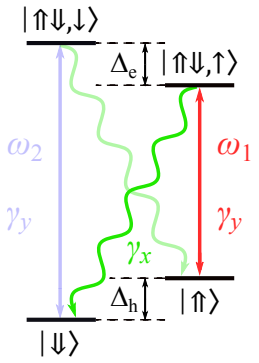

Figure 2.7: Optical spin pumping for a positive trion X^+ in Voigt geometry, with the magnetic field oriented in the y-direction. Driving the low-energy transition (red) eventually shelves the hole-spin in $|\Downarrow\rangle$, as a result of a decay via the diagonal (green) path.

Resonantly driving the low-energy transition, $|\Uparrow\rangle \rightarrow |\Uparrow\Downarrow,\uparrow\rangle$, by y-polarized light[8] populates the trion state. Due to the cyclicity $C = \gamma_y/\gamma_x \approx 15$ induced by the PCW, the trion state $|\Uparrow\Downarrow,\uparrow\rangle$ is most likely to decay back to $|\Uparrow\rangle$ with the decay rate γ_y. However, driving the transition until the trion decays via $|\Uparrow\Downarrow,\uparrow\rangle \rightarrow |\Downarrow\rangle$ effectively creates a three-level Λ-system, where the $|\Downarrow\rangle$ acts as a dark state. Ideally, the state is now shelved from any further interaction and thus not accessible by the pumping laser. In similar way, pumping the high energy transition shelves the opposite spin-state $|\Uparrow\rangle$. Measuring the resonance fluorescence from the driven transition, the timescale of the spin-pumping process can be extracted[9].
Experimentally, OSP can be utilized for spin initialization, which in this work results in the hole-spin being prepared and initialized in $|\Downarrow\rangle$. From Table 2.1, this technique can be performed with close to unity probability.

2.3.2 Coherent Spin Rotation

The ability to control and manipulate the spin-state is an essential tool towards realizing the entanglement protocol presented in this thesis. Thus, this section will give an introduction to *Raman* transitions, utilized for optical spin control between two ground states. Starting with a three-level Λ-system, the goal is to derive a scheme for which only the ground states $\{|g_1\rangle, |g_2\rangle\}$ are coupled, whereby the excited state $\{|e\rangle\}$ works as an auxiliary (or intermediate) state. It will be shown, that under the right conditions, the Λ-system can therefore effectively be reduced to a two-level system. In the context of the positive trion, the two ground states correspond to $\{|\Downarrow\rangle, |\Uparrow\rangle\}$, while the excited state is given by $\{|\Uparrow\Downarrow,\uparrow\rangle\}$.
Using Raman transitions for coherent spin rotations, both the vertical and diagonal transitions are required in order to couple the ground states. Thus, it is convenient to work in Voigt geometry, as it makes both transition types accessible[10].

Raman Transitions

In the physical system, forming a Λ-configuration, the ground states $\{|g_1\rangle, |g_2\rangle\}$ are coupled to the excited state $\{|e\rangle\}$ via two optical fields with angular frequency ω_{g_n}. Both frequencies are far-off detuned by Δ_n compared to the resonance frequency $\omega_{0_{gn}}$ of each transition, thus avoiding to drive the population into the excited state, see Fig. 2.8. As a consequence, the spontaneous emission from the excited state can be ignored, as it otherwise would destroy the quantum coherence [17]. Furthermore, it is assumed that the ground state splitting Δ_g is much smaller than the optical transitions, $\Delta_g \ll \omega_{g_n}$, whereby the detunings Δ_n are roughly equal, $\delta = \Delta_2 - \Delta_1 \approx 0$. For simplicity, the excited state energy is set to zero, $E_e = 0$.

[8] With respect to the PCW-coordinates system defined in Section 2.2.1, Fig. 2.5.
[9] For the purposes of this work, a pumping laser is applied over a duration of 200 ns.
[10] See the final paragraph of Section 2.1.2 for the optical selection rules in Voigt geometry.

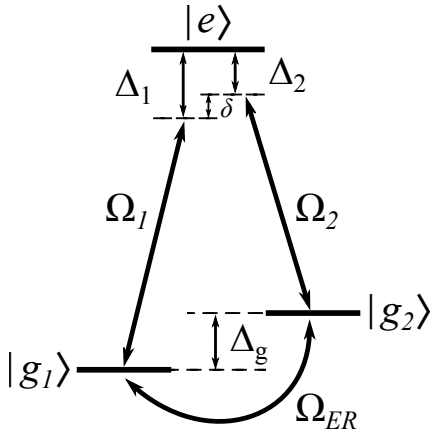

Figure 2.8: Raman transitions for optical spin control in a three-level Λ-configuration. Two far-off detuned frequencies ω_{g_n}, each with a Rabi-frequency Ω_n, couples to an intermediate state $|e\rangle$. Given proper conditions, the system can be reduced to an effective two-level configuration consisting of $|g_1\rangle$ and $|g_2\rangle$, coupled by an effective Rabi-frequency Ω_{ER}.

Under these assumptions, the evolution and dynamics of the system can be derived[11]. Having two monochromatic lasers, each with angular frequency ω_{g_n}, the combined E-field in the *Dipole approximation*[12] is given by

$$\vec{E}(t) = E_1 \cos(\omega_{g_1} t)\hat{\epsilon}_1 + E_2 \cos(\omega_{g_2} t)\hat{\epsilon}_2 \tag{2.3.2}$$

$$= \vec{E}^{(+)}(t) + \vec{E}^{(-)}(t), \tag{2.3.3}$$

where $\hat{\epsilon}_n$ is the unit-polarization vectors of the two fields with amplitude E_n and $\vec{E}^{(\pm)}(t)$ is the positive/negative rotation parts of the E-field, taking the form

$$\vec{E}^{(\pm)}(t) = \frac{1}{2}\left(\sum_n E_n e^{(\mp i\omega_{g_n} t)}\hat{\epsilon}_n\right). \tag{2.3.4}$$

With the energy of the excited state being zero, the 3-level Λ-system is described by the *Free Emitter* Hamiltonian expressed as

$$\hat{H}_0 = -\hbar\omega_{0_{g_1}} |g_1\rangle \langle g_1| - \hbar\omega_{0_{g_2}} |g_2\rangle \langle g_2|. \tag{2.3.5}$$

Furthermore, the coupling between the emitter and optical field is given by the *Interaction* Hamiltonian, which in the dipole approximation and *Rotating-wave approximation*[13] (RWA)

[11] The following derivation is partially based on Section 6.1 in Ref. [17].

[12] In the dipole approximation, the spatial dependence of the optical field is ignored. This assumption is based on the optical wavelength being much larger than the size of the atom(or, in this case the QD), and thus any variations of the optical field over the length-scale of the atom is neglected.

[13] In the case where the resonance frequency $\omega_{0_{gn}}$ of the emitter and the optical frequency of the input field ω_{g_n} fulfills the following requirement; $\left|\omega_{g_n} - \omega_{0_{gn}}\right| \ll \omega_{g_n} + \omega_{0_{gn}}$, the rotating-wave approximation can be assumed. In the context of the interaction between emitter, i.e. dipole operator $d^{(\pm)} \sim e^{\mp i\omega_{0_{gn}} t}$, and optical field, the fast oscillating terms, i.e. $e^{\pm i(\omega_{g_n} + \omega_{0_{gn}})t}$ are ignored (their average value set to zero), while the slow oscillation terms, $e^{\pm i(\omega_{g_n} - \omega_{0_{gn}})t}$ are kept. Physically, the fast oscillating terms corresponds to absorption(emission) of a photon as the emitter decays(is excited). Thus, in Eq. 2.3.6 the two terms $\hat{d}^{(\pm)} \cdot \hat{E}^{(\pm)}$ are left out.

takes the form

$$\begin{aligned}\hat{H}_I &= -\hat{d}\cdot\hat{E} \\ &\approx -\left(\hat{d}^{(+)}\cdot\hat{E}^{(-)}+\hat{d}^{(-)}\cdot\hat{E}^{(+)}\right),\end{aligned} \tag{2.3.6}$$

where $\hat{d}=-qr$ is the dipole operator, expressed by the charge q and position $\hat{r}$. As for the E-field, the dipole operator can be decomposed to a positive and negative part

$$\begin{aligned}\hat{d} &= \hat{d}^{(+)}+\hat{d}^{(-)} \\ &= \sum_n \langle g_n|\,\hat{d}\,|e\rangle\,\hat{\sigma}_{g_n,e}+\sum_n \langle g_n|\,\hat{d}\,|e\rangle\,\hat{\sigma}^{\dagger}_{e,g_n},\end{aligned} \tag{2.3.7}$$

where $\hat{\sigma}_{g_n,e}=|g_n\rangle\langle e|$ is the atomic annihilation operator and $\hat{\sigma}^{\dagger}_{e,g_n}=|e\rangle\langle g_n|$ the creation operator. Thus, the interaction Hamiltonian can be expressed by

$$\hat{H}_I=\sum_n\frac{\hbar\Omega_n}{2}\left(e^{i\omega_{g_n}t}\hat{\sigma}_{g_n,e}+e^{-i\omega_{g_n}t}\hat{\sigma}^{\dagger}_{e,g_n}\right), \tag{2.3.8}$$

where $\Omega_n=-\frac{\langle e|\hat{d}\cdot\hat{\epsilon}_n|g_n\rangle E_n}{\hbar}$ is the *Rabi*-frequency of the nth transition. This parameter describes the strength of the emitter-field interaction and denotes the angular frequency whereby the population oscillates between two states.
Finally, transforming into the *rotating frame* of the laser field, for which the E-field transforms according to $\tilde{E}_n^{(\pm)}\equiv\vec{E}_n^{(\pm)}e^{\pm i\omega_{g_n}t}$, enables the free emitter Hamiltonian to be written as

$$\tilde{H}_0=\hbar\Delta_1\,|g_1\rangle\langle g_1|+\hbar\Delta_2\,|g_2\rangle\langle g_2|, \tag{2.3.9}$$

whereby the energy of the ground states are increased by a factor of $\hbar\omega_{g_n}$. Consequently, the interaction Hamiltonian simplifies to

$$\tilde{H}_I=\sum_n\frac{\hbar\Omega_n}{2}\left(\hat{\sigma}_{g_n,e}+\hat{\sigma}^{\dagger}_{e,g_n}\right). \tag{2.3.10}$$

Thus, the combined Hamiltonian of the system, expressed in the rotating frame of the applied field, takes the form

$$\begin{aligned}\tilde{H} &= \tilde{H}_0+\tilde{H}_I \\ &= \hbar\Delta_1\,|g_1\rangle\langle g_1|+\hbar\Delta_2\,|g_2\rangle\langle g_2|+\sum_n\frac{\hbar\Omega_n}{2}\left(\hat{\sigma}_{g_n,e}+\hat{\sigma}^{\dagger}_{e,g_n}\right).\end{aligned} \tag{2.3.11}$$

The stage is now set, to look at the time-evolution of the system, by solving the time-dependent Schrödinger equation

$$i\hbar\frac{\partial}{\partial t}\,|\Psi(t)\rangle=\tilde{H}\,|\Psi(t)\rangle, \tag{2.3.12}$$

for which $|\Psi(t)\rangle$ represents the total state given by

$$|\Psi(t)\rangle=c_{g_1}(t)\,|g_1\rangle+c_{g_2}(t)\,|g_2\rangle+c_e(t)\,|e\rangle, \tag{2.3.13}$$

where $c_n(t)$ are the time-dependent probability amplitudes for each eigenstate. Inserting the total Hamiltonian into the time-dependent Schrödinger equation gives

$$\begin{aligned} i\hbar\frac{\partial}{\partial t}\left|\Psi(t)\right\rangle &= \hbar\Delta_1 c_{g_1}(t)\left|g_1\right\rangle + \hbar\Delta_2 c_{g_2}(t)\left|g_2\right\rangle \\ &+ \frac{\hbar\Omega_1}{2}\left(c_e(t)\left|g_1\right\rangle + c_{g_1}(t)\left|e\right\rangle\right) + \frac{\hbar\Omega_2}{2}\left(c_e(t)\left|g_2\right\rangle + c_{g_2}(t)\left|e\right\rangle\right). \end{aligned} \tag{2.3.14}$$

Projecting onto with $\langle g_1|$, $\langle g_2|$ and $\langle e|$, the equations of motion are given by

$$i\hbar\frac{\partial}{\partial t}c_{g_1}(t) = \frac{\hbar\Omega_1}{2}c_e(t) + \hbar(\Delta_1 - \Delta)c_{g_1}(t), \tag{2.3.15}$$

$$i\hbar\frac{\partial}{\partial t}c_{g_2}(t) = \frac{\hbar\Omega_2}{2}c_e(t) + \hbar(\Delta_2 - \Delta)c_{g_2}(t), \tag{2.3.16}$$

$$i\hbar\frac{\partial}{\partial t}c_e(t) = \frac{\hbar\Omega_1}{2}c_{g_1}(t) + \frac{\hbar\Omega_2}{2}c_{g_2}(t) - \hbar\Delta c_e(t), \tag{2.3.17}$$

where all energies are shifted by a factor of $-\hbar\Delta$, where $\Delta \equiv (\Delta_1 + \Delta_2)/2$. In the limit of $|\Delta| \gg \Omega_n$, the excited state can adiabatically be eliminated, i.e. one may assumed that $\dot{c}_e(t) = 0$. Consequently, Eq. 2.3.17 can be expressed as

$$c_e(t) = \frac{\Omega_1}{2\Delta}c_{g_1}(t) + \frac{\Omega_2}{2\Delta}c_{g_2}(t). \tag{2.3.18}$$

Removing the energy shift of $-\hbar\Delta$, the equations of motion can be reduced to

$$\begin{aligned} i\hbar\dot{c}_{g_1}(t) &= \frac{\hbar\Omega_1}{2}c_e(t) + \hbar\Delta_1 c_{g_1}(t) \\ &= \frac{\hbar\Omega_{ER}}{2}c_{g_2}(t) + \left(\hbar\omega_{\mathrm{S},1} + \hbar\Delta_1\right)c_{g_1}(t), \end{aligned} \tag{2.3.19}$$

and

$$\begin{aligned} i\hbar\dot{c}_{g_2}(t) &= \frac{\hbar\Omega_2}{2}c_e(t) + \hbar\Delta_2 c_{g_2}(t) \\ &= \frac{\hbar\Omega_{ER}}{2}c_{g_1}(t) + \left(\hbar\omega_{\mathrm{S},2} + \hbar\Delta_2\right)c_{g_2}(t), \end{aligned} \tag{2.3.20}$$

which now resemble that of a two-level system. Furthermore, Ω_{ER} is the *Effective Rabi* frequency (or sometimes Raman frequency), while $\omega_{S,n}$ is the optical *AC-Stark* shift

$$\Omega_{ER} = \frac{\Omega_1\Omega_2}{2\Delta}, \qquad \omega_{S,n} = \frac{\Omega_n^2}{4\Delta}. \tag{2.3.21}$$

As a result of the incident field, the energy levels are slightly shifted due to the Stark effect. Taking this into account, the effective two-level system is said to be in resonance, if the following condition is satisfied

$$\delta_{ER} \equiv \delta + \delta_S = 0, \tag{2.3.22}$$

where $\delta_S = \omega_{S,2} - \omega_{S,1}$ denotes the effective detuning from the AC-Stark shift.
Finally, the equations of motion can hence be generated by the *Effective Raman* Hamiltonian, taking the form

$$\hat{H}_{ER} = \sum_n \left(\hbar(\Delta_n + \omega_{S,n})\left|g_n\right\rangle\left\langle g_n\right|\right) + \frac{\hbar\Omega_{ER}}{2}\left(\sigma_{ER} + \sigma_{ER}^\dagger\right), \tag{2.3.23}$$

where $\sigma_{ER} = |g_1\rangle\langle g_2|$ and $\sigma_{ER}^{\dagger} = |g_2\rangle\langle g_1|$ is the Raman annihilation and creation operator, respectively. Thus, given the proper conditions, a three-level Λ-system can effectively be reduced to a two-level system. This technique can efficiently be employed for the coherent spin rotations between the ground states $|\Uparrow\rangle$ and $|\Downarrow\rangle$. Previous studies has successfully implemented this method into their experiments, revealing close to unity fidelities on π-rotations with an effective Rabi-frequency of $\Omega_{ER} \approx 150$ MHz [18].

2.4 Summary

Various techniques and properties of the solid-state QD has be presented in this chapter. In summary, the principles behind excitation and charging schemes has been review, followed by a derivation of optical selection rules in different geometries, depending on the orientation of the external magnetic field. The main focus has been directed towards a positively charged trion state X^+ embedded in a PCW. The latter enables high cyclicity in the order of $C^{(+)} \approx 15$ between the low-energy transition $|\Uparrow\rangle \leftrightarrow |\Uparrow\Downarrow, \uparrow\rangle$ for an in-plane magnetic field, i.e. Voigt geometry. In return, the diagonal transitions of the four-level energy diagram are accessible, whereby coherent spin rotations can be implemented through the use of Raman transitions. In short, the ability to control and manipulate the hole-spin while utilizing the benefits of the photonic environment, i.e. the enhanced cyclicity, provides a promising system towards realizing spin-photon entanglement. The latter is the subject of the following chapter.

Chapter 3

Quantum Entanglement

"I would not call that *one* but rather *the* characteristic trait of quantum mechanics, the one that enforces its entire departure from classical lines of thought."[19]

— E. Schrödinger, 1935

In the quote above, Schrödinger is referring to the quantum mechanical phenomenon called *entanglement*. In the following chapter the definition and applications of entanglement will be reviewed. Furthermore, multi-partite entangled states will be introduced, including Greenberger–Horne–Zeilinge (GHZ) and Cluster states. The experimental protocol for multi-photon entanglement generation using a QD embedded into a nanostructure will be presented, along with methods of certifying entanglement based on a limited number of measurement settings.

3.1 Introduction to Quantum States

In quantum mechanics, a closed system is described by a *state*. Following Dirac notation, a state is a vector, usually denoted $|\psi\rangle$, defined in the *Hilbert* space, $\mathcal{H}$ (or *State* space), spanning the complex numbers, $\mathbb{C}$.
In the case where a quantum system is completely known, the corresponding state is said to be a *pure* state [20]. However, some quantum states are constructed by a statistical mixture of pure state - also known as *mixed* states. A pure quantum states is thus represented by a *ray* in the Hilbert space, while mixed states are described by the *density matrix*, ρ.

3.1.1 The Density Matrix

The density matrix (or density operator) is a useful tool to describe a system, where the total state defining the entire system is only partially known. Suppose the system can be decomposed into i-subsystems, each represented by $|\psi_i\rangle$ with a corresponding probability p_i, then the density matrix is defined as the sum over the outer product of the *ensemble* of pure states $\{p_i, |\psi_i\rangle\}$, which takes the form [20]

$$\rho \equiv \sum_i p_i \left|\psi_i\right\rangle \left\langle\psi_i\right|, \tag{3.1.1}$$

where $\sum_i p_i = 1$ for proper normalization. Any non-negative operator with unit trace $\mathrm{Tr}[\rho] = 1$, is a density operator [21]. From the definition of the density matrix, a system described by a pure state fulfils the relation $\rho^2 = \rho$. Using this formalism, it can be determined if a system is in a pure- or mixed-state depending on the following criteria

$$\mathrm{Tr}[\rho^2] = \begin{cases} 1 & \text{Pure state,} \\ < 1 & \text{Mixed state.} \end{cases} \tag{3.1.2}$$

The physical interpretation of the density matrix becomes more clear once the *density matrix elements* $\rho_{n,m} \equiv \langle n| \rho |m\rangle$ are considered. Here, the diagonal elements $\rho_{n,m}$ (for $n = m$) provides the probability of being in the nth state, thus referred to as *populations*. On the other hand, the off-diagonal elements $\rho_{n,m}$ (for $n \neq m$) are known as *coherences*, as they provide information about the relative phase between two different elements of the density matrix [17].

The Reduced Density Matrix

In the analysis of a large quantum system, composed of multiple subsystem, it can often be desirable to focus at a given subset of interest. Suppose two subsystems A and B makes up a composite quantum system, spanning the Hilbert space $\mathcal{H} = \mathcal{H}_A \otimes \mathcal{H}_B$, described by

$$\rho_{AB} = \rho_A \otimes \rho_B, \tag{3.1.3}$$

where $\otimes$ is the tensor product, then the *reduced density matrix* for system A takes the form

$$\rho_A \equiv \mathrm{Tr}_B[\rho_{AB}] = \sum_{j=1}^{d_B} \left(I_A \otimes \langle b_j|\right) \rho_{AB} \left(I_A \otimes |b_j\rangle\right). \tag{3.1.4}$$

where Tr_B is the partial trace over system B [20]. Furthermore, I_A denotes the identity operator of Hilbert space $\mathcal{H}_A$, while $\{|b_j\rangle\}$ are the basis vectors of subsystem B with the dimensions $d_B = \dim\mathcal{H}_B$. Thus, this formalism provides a useful tool when investigating a composite quantum system, where only a subsystem are to be examined.

3.2 Quantum Entanglement and Multi-Partite States

Quantum entanglement is often considered the "most quantum-like" phenomenon in quantum mechanics, having no classical analog. It can only be created, if the involving systems interact with each other, and has many applications in the field of quantum information. Perhaps some of the most notable applications include *superdense coding* ([22], [23]), *quantum teleportation* [24] and *quantum cryptography* [25] e.g. quantum key distribution (QKD), which in the area of quantum commutation traditionally involves Alice (the transmitter) and Bob (the receiver). Each and every one of these subjects are very interesting, uncovering new possibilities and technologies. This however, is unfortunately left to the reader to explore, as it is outside the limits of this work[1].

[1] For instance, see Ref. [4] or Ref. [20] for more information on the topics regarding Quantum Information.

Nevertheless, central to all these applications is the use of quantum entanglement between various states. Thus, this section seeks to give an overview of both bipartite and multi-partite entangled states, along with its properties - starting with the bare definition.

3.2.1 Definition of Quantum Entanglement

Quantum states are said to be entangled, if they are *non-separable*. In other words, given two entangled subsystems A and B, *quantum correlations* will be demonstrated upon measurement[2]. Mathematically, a bipartite quantum system of two pure states, $|\psi\rangle_A \in \mathcal{H}_A$ and $|\psi\rangle_B \in \mathcal{H}_B$, is thus entangled if and only if it *cannot* be written as a product state

$$|\psi\rangle_{AB} = |\psi\rangle_A \otimes |\psi\rangle_B \,, \tag{3.2.1}$$

for $|\psi\rangle_{AB} \in \mathcal{H}_A \otimes \mathcal{H}_B$. This definition can be extended to a more general statement, using the density matrix formalism introduced in Section 3.1. Letting $\rho^{(AB)}$ denote the density operator of a composite quantum system of two mixed states, it is said to be *separable* if and only if it can be expressed as

$$\rho^{(AB)} = \sum_i p_i \rho_i^{(A)} \otimes \rho_i^{(B)}, \tag{3.2.2}$$

otherwise $\rho^{(AB)}$ *is* entangled [26]. This statement can be generalized to a N-partite state, which is said to be *fully separable* if and only if

$$\rho = \sum_i p_i \rho_i^{(1)} \otimes ... \otimes \rho_i^{(N)}, \qquad |\psi\rangle = |\psi\rangle_1 \otimes ... \otimes |\psi\rangle_N \,, \tag{3.2.3}$$

for a mixed- and pure-state, respectively.
Furthermore, a pure bipartite quantum system is considered to be *maximally* entangled if the reduced density operator of either subsystem is maximally mixed and hence proportional to the identity operator [4]. An example of such states are the *Bell* states.

The Bell States

Perhaps the simplest and most renowned quantum states, containing two maximally entangled qubits, are the four Bell states

$$\left|\Phi^{\pm}\right\rangle_{AB} = \frac{1}{\sqrt{2}} \left(|0_A 0_B\rangle \pm |1_A 1_B\rangle\right), \tag{3.2.4}$$

$$\left|\Psi^{\pm}\right\rangle_{AB} = \frac{1}{\sqrt{2}} \left(|0_A 1_B\rangle \pm |1_A 0_B\rangle\right), \tag{3.2.5}$$

all being pure quantum states, i.e. the density matrix upholds $\rho_{AB}^2 = \rho_{AB}$. The reduced density matrix however, is a mixed state as $\mathrm{Tr}[\rho_{\{A,B\}}^2] < 1$, meaning not all information can be obtained about each subsystem A or B, as opposed to the complete system given by the Bell states[3] [20]. This counter-intuitive nature is yet an other striking feature of quantum mechanics, revealing non-classical correlations of entangled quantum states.

[2] It should be noted, that even though two system are separable, that can still be correlated.
[3] See Appendix A.1 for a small derivation proving these claims.

3.2.2 Multi-Partite Entangled Quantum States

Until now, entangled states involving only two particles has been considered. However, numerous multi-partite entangled states can be constructed, like the W state[4], *Cluster* state and *GHZ* state. The focus in the thesis will be the generation of N-qubit Cluster- and GHZ-states. Protocols has been proposed, employing multi-partite entangled states such as the GHZ state for quantum communication [27] and quantum metrology [28], while the Cluster states can be utilized for measurement-based quantum computation ([29], [30]). These states are hence promising candidates for future applications in quantum information processing.

Greenberger–Horne–Zeilinger (GHZ) State

The Greenberger–Horne–Zeilinger state (GHZ state) is a particular quantum state, which involves $N \geq 3$ subsystems. In the case of N qubits, the GHZ state takes the form

$$|\mathrm{GHZ}^{(N)}\rangle = \frac{1}{\sqrt{2}}\left(|0\rangle^{\otimes N} + |1\rangle^{\otimes N}\right), \tag{3.2.6}$$

where $|0\rangle$ and $|1\rangle$ represents the logical states of the qubits. Clearly, the simplest GHZ state contains $N = 3$ qubits

$$|\mathrm{GHZ}^{(3)}\rangle = \frac{1}{\sqrt{2}}\left(|000\rangle + |111\rangle\right), \tag{3.2.7}$$

which can be considered a generalization of the Bell states, being maximally entangled as well [26]. A remarkable characteristic of the GHZ state can be observed if one writes up the reduced density matrix, tracing out one subsystem

$$\rho_{AB}^{(GHZ)} = \mathrm{Tr}_C[\rho_{ABC}^{(GHZ)}] = \mathrm{Tr}_C\left[|\mathrm{GHZ}^{(3)}\rangle\langle\mathrm{GHZ}^{(3)}|\right], \tag{3.2.8}$$

leaving the state $\rho_{AB}^{(GHZ)}$ fully separable, and hence no longer entangled[5].

Cluster State

The Cluster state is an entangled quantum state that can be regarded as an ensemble of qubits positioned in a d-dimensional lattice ($d = 1, 2, 3$) at site $i \in \mathbb{Z}^d$ [31]. For the purposes of this work, only one-dimensional Cluster states will be considered, to which the generalized N-qubit state can be expressed as

$$|\mathrm{CS}^{(N)}\rangle = \frac{1}{2^{N/2}}\bigotimes_{i=1}^{N}\left(|0\rangle_i\,\sigma_z^{(i+1)} + |1\rangle_i\right), \tag{3.2.9}$$

applying the Pauli matrix $\sigma_z = \begin{pmatrix} 1 & 0 \\ 0 & -1 \end{pmatrix}$ to the subsequent qubit $(i+1)$, while $\sigma_z^{(N+1)} \equiv 1$ being a convention. In contrast to the GHZ state, the Cluster state requires a minimum

[4]The W state is a three qubit entangled state of the form $|W\rangle = \frac{1}{\sqrt{3}}(|001\rangle + |010\rangle + |100\rangle)$.

[5]In comparison, the reduced density matrix for the W state $\rho_{AB}^{(W)} = \mathrm{Tr}_C\left[|\mathrm{W}\rangle\langle\mathrm{W}|\right]$, remains entangled under this operation, making it more robust against losses [26].

of $N/2$ local measurements for the state being completely disentangled - a figure of merit defined by Briegel *et al.* (Ref. [31]) as its *persistency of entanglement*. In this sense, the entanglement of the Cluster state is considered "more" entangled than most known N-qubit states, e.g. the GHZ states. Another term defined by Briegel *et al.*, is the so-called *maximal connectedness*, whereby a state is said to be maximally connected if any two qubits of a quantum state deterministically can be projected into a Bell state by local measurements on a subset of the other qubits. For a concrete example, consider the simplest two qubit Cluster state taking the form

$$|\mathrm{CS}^{(2)}\rangle = \frac{1}{2}\left[(|0\rangle_1 \sigma_z^{(2)} + |1\rangle_1)(|0\rangle_2 + |1\rangle_2)\right] \tag{3.2.10}$$

$$= \frac{1}{2}\left(|0\rangle_1 |0\rangle_2 - |0\rangle_1 |1\rangle_2 + |1\rangle_1 |0\rangle_2 + |1\rangle_1 |1\rangle_2\right) \tag{3.2.11}$$

$$= \frac{1}{\sqrt{2}}\left(|0-\rangle + |1+\rangle\right), \tag{3.2.12}$$

where the subscripts are omitted in the final expression and $|\pm\rangle = \frac{1}{\sqrt{2}}(|0\rangle \pm |1\rangle)$. This is a maximally entangled state, where the latter forms a Bell state by unitary basis change; $\{|-\rangle, |+\rangle\} \to \{|0\rangle, |1\rangle\}$. Furthermore, if one considers the three qubit Cluster state

$$|\mathrm{CS}^{(3)}\rangle = \frac{1}{2^{3/2}}\left(|000\rangle + |100\rangle - |001\rangle - |101\rangle - |010\rangle - |011\rangle + |110\rangle + |111\rangle\right) \tag{3.2.13}$$

$$= \frac{1}{\sqrt{2}}(|+0-\rangle - |-1+\rangle), \tag{3.2.14}$$

the latter forms a GHZ state up to local unitary transformations. It should be noted, that for $N > 3$, the $|\mathrm{CS}^{(N)}\rangle$ is *not* equivalent to $|\mathrm{GHZ}^{(N)}\rangle$.
Having introduced the various multi-partite entangled states under consideration in this thesis, the attention can now be directed towards the creation of such states, i.e. the entanglement protocol.

3.3 Multi-Partite Entanglement Protocol

Based on the paper by K. Tiurev *et al.* [32], this section aims to present an entanglement protocol that generates multi-photon entangled states, i.e. GHZ and Cluster states, while being compatible with a QD embedded into photonic nanostructures. In other words, this protocol leans on the working principle of a so-called *photonic machine gun*, that is a system generating a steady stream of entangled photons, originally proposed by Lindner and Rudolph [33].
In this work, the following protocol relies on the entanglement between a "stationary" qubit and stream of "flying" qubits, realized by a hole-spin $\{|\Uparrow\rangle, |\Downarrow\rangle\}$ in a positive charged trion X^+ and the time-bin encoding of early/late photons $\{|e\rangle, |l\rangle\}$. The creation, manipulation and dynamics of the spin-qubit are examined in Chapter 2, while the generation of the photonic-qubit will be introduced in Chapter 4.
Before considering the individual steps of the entanglement protocol, it can be divided into three parts: (i) Initialization of the QD and its spin, (ii) the main sequence for entanglement generation and (iii) final spin rotation and readout.

Experimentally, the former is realized through the charging principle presented in Section 2.1.1 using an above-band (ABB) laser, while the spin is initialized via optical spin pumping (OSP), described in Section 2.3.1. All coherent spin rotations performed in part (ii) and (iii) are accomplished using Raman transitions, which is covered in Section 2.3.2. In Fig. 3.1 the pulse sequence is presented, along with an energy diagram for X^+, showing the corresponding transitions/rotations.

The ideal protocol for sequential generation of time-bin entangled photons are as follows:

(i) Spin Initialization:

0. Charge the QD to a positive trion X^+ and initialize the hole-spin, using an ABB-laser and OSP on the low energy transition $|\Uparrow\rangle \leftrightarrow |\Uparrow, \Downarrow, \uparrow\rangle$, respectively.
1. Rotate the ground state spin into an equal superposition $|\Psi\rangle = \frac{1}{\sqrt{2}}(|\Uparrow\rangle + |\Downarrow\rangle)$, using a $\pi/2$-rotation pulse on the $|\Uparrow\rangle \leftrightarrow |\Downarrow\rangle$ transition.

(ii) Main Sequence:

2. Apply a π-pulse, which resonantly drives the optical transition $|\Uparrow\rangle \leftrightarrow |\Uparrow\Downarrow, \uparrow\rangle$, resulting in the generation of a photon in the early time-bin $|e\rangle$ upon emission.
3. Flip the ground states $\{|\Uparrow\rangle, |\Downarrow\rangle\}$ by a π-rotation pulse.
4. Repeat step 2, thus generating a photon in the late time-bin $|l\rangle$.
5. - For GHZ state: Repeat step 3.
   - For Cluster state: Apply a $\pi/2$-rotation around x or y axis (or the Hadamard gate) between the two ground states $\{|\Uparrow\rangle, |\Downarrow\rangle\}$.
6. Repeat steps 2-5 N-times to create a N-photon entangled state.

(iii) Spin Readout:

7. Rotate the spin by an arbitrary angle $\Phi \in \{\theta, \phi\}$ on the Bloch sphere (see Fig. 2.6), dependent on the basis to be measured, and perform the spin-readout, i.e. pump the low energy transition (as in step 0).

Going through steps 0-5 of the protocol for the GHZ state, the initial state $|\Psi\rangle_i$ evolves as

$$|\Psi\rangle_i \xrightarrow{0} |\Downarrow\rangle, \quad \text{ABB and OSP} \tag{3.3.1}$$

$$\xrightarrow{1} \frac{1}{\sqrt{2}}(|\Uparrow, \emptyset\rangle + |\Downarrow, \emptyset\rangle), \quad \text{Spin rotating } \pi/2\text{-pulse} \tag{3.3.2}$$

$$\xrightarrow{2} \frac{1}{\sqrt{2}}(|\Uparrow, e\rangle + |\Downarrow, \emptyset\rangle), \quad \text{Optical } \pi\text{-pulse} \tag{3.3.3}$$

$$\xrightarrow{3} \frac{1}{\sqrt{2}}(|\Downarrow, e\rangle - |\Uparrow, \emptyset\rangle), \quad \text{Spin rotating } \pi\text{-pulse} \tag{3.3.4}$$

$$\xrightarrow{4} \frac{1}{\sqrt{2}}(|\Downarrow, e\rangle - |\Uparrow, l\rangle), \quad \text{Optical } \pi\text{-pulse} \tag{3.3.5}$$

$$\xrightarrow{5} \frac{1}{\sqrt{2}}(|\Uparrow, e\rangle + |\Downarrow, l\rangle), \quad \text{Spin-photon Bell state} \tag{3.3.6}$$

where $|\emptyset\rangle$ denotes the photon vacuum state. Thus, going through the protocol ones effectively creates a spin-photon Bell state, where $\{|\Uparrow\rangle, |e\rangle\}$ and $\{|\Downarrow\rangle, |l\rangle\}$ represent the logical states $|0\rangle$ and $|1\rangle$, respectively.

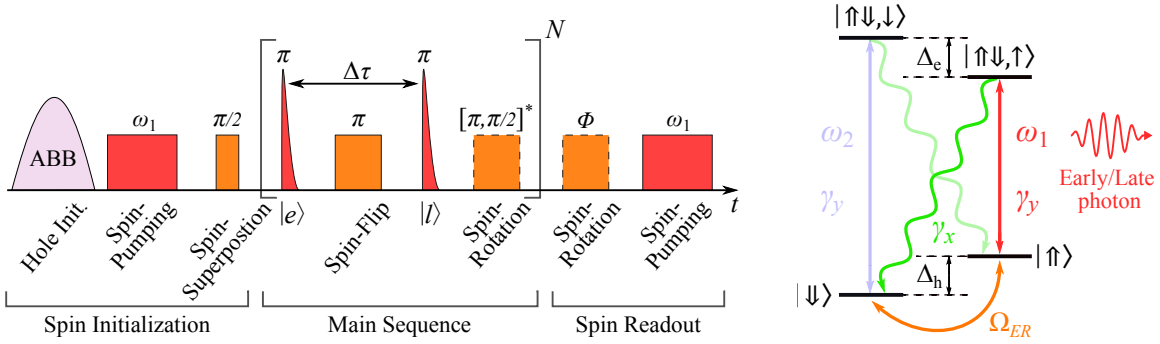

(a) Multi-partite Entanglement Protocol.
*$\pi(\pi/2)$ spin rotation for GHZ(Cluster)-state.

(b) Energy Diagram for X^+.

Figure 3.1: (a) Pulse sequence for multi-partite entanglement protocol generating GHZ- and Cluster-states. The time difference $\Delta\tau \approx 11.83$ ns is set by the spatial difference between the two paths of the Time-bin Interferometer (See Chapter 4), effectively creating an early and late pulse. Repeating the main sequence (marked by the brackets) N-times, produces a $N+1$ qubit GHZ- or Cluster-state. (b) Corresponding energy diagram for the positively charged trion, X^+. The spin rotations are driven with an effective Rabi frequency Ω_{ER} (orange), while the optical transition $|\Uparrow\rangle \leftrightarrow |\Uparrow\Downarrow,\uparrow\rangle$ are addressed by a laser with an angular frequency ω_1 (red).

3.4 Entanglement Detection and Fidelity Estimation

This section addresses some of the obstacles towards certifying and characterizing multi-partite entanglement using only a limited number of measurement. Based on the latter, one may determine the fidelity or construct a lower bound, dependent on the given quantum state under consideration.

3.4.1 Fidelity of Quantum States

The *fidelity* is a way of quantifying the indistinguishably between two quantum systems. In the case of two pure states $|\psi\rangle$ and $|\phi\rangle$, the fidelity takes the form

$$\mathcal{F} = |\langle\phi|\psi\rangle|^2, \tag{3.4.1}$$

with the bounds $0 \leq \mathcal{F} \leq 1$. For $\mathcal{F} = 1$ there is complete *overlap* and thus the two states are identical [21]. If however, the systems are expressed by two density operators ρ and σ, the fidelity is defined as [4]

$$\mathcal{F}(\rho,\sigma) = \left(\mathrm{Tr}\left\{\sqrt{\rho^{1/2}\sigma\rho^{1/2}}\right\}\right)^2, \tag{3.4.2}$$

being symmetric for ρ and σ, i.e. $\mathcal{F}(\rho,\sigma) = \mathcal{F}(\sigma,\rho)$. This expression can be simplified, given one of the two states is pure. Assuming $\rho = |\psi_\rho\rangle\langle\psi_\rho|$ to be a pure state, the fidelity can be reduced to

$$\mathcal{F}(\rho,\sigma) = \langle\psi_\rho|\,\sigma\,|\psi_\rho\rangle\,. \tag{3.4.3}$$

Typically, experiments seek to create a pure multi-partite entangled state $|\psi_\rho\rangle$, e.g. a GHZ- or Cluster-state. However, due to noise and imperfections associated with all experiments, the state produced will be a mixed state σ_{exp}, differing from the desired state. The challenge is thus to reconstruct the density matrix σ_{exp} from experimental data and subsequently quantify the fidelity using Eq. 3.4.3.

3.4.2 Fidelity Bounds

A complete characterization of a given quantum system requires a sequence of identical measurements performed in various sets of bases. This process is also known as a *quantum state tomography*, whereby the entire density matrix can be reconstructed, i.e. full knowledge about the quantum state can be gained. However, the amount of resources required for the full quantum tomography scales exponentially with the number of particles involved, and it is therefore very difficult and time consuming to perform, making it close to impossible for a large system. Thus, one needs to explore alternative ways to quantify the quantum state for realistic experiments.

The following paragraphs serves as a brief introduction to some of the alternative ways of certifying multi-partite states. However, a comprehensive description is outside the scope of this thesis, but the reader may find more information on this topic in Ref. [34].

Fidelity of the GHZ state

Following Gühne *et al.* [35] the fidelity of a N-qubit GHZ state can be determined using only $N+1$ measurement settings, whereby the number of measurement scales linear opposed to exponential. This is realised by N measurement settings on the x-y-plane of the Bloch sphere, and one measurement setting in $(\sigma_z)^{\otimes N}$, i.e. the z-axis of the Bloch sphere. The in-plane measurement should be performed according to the following relation

$$\mathcal{M}_k = \left[\cos\left(\frac{k\pi}{N}\right)\sigma_x + \sin\left(\frac{k\pi}{N}\right)\sigma_y\right]^{\otimes N}, \tag{3.4.4}$$

where $k = 1, ..., N$ and $\sigma_{\{x,y,z\}}$ denotes the Pauli matrices.
An experimental demonstration of this particular measurement scheme can be found in Ref. [36], aiming to produce a ten-photon GHZ-state and Ref. [37] seeking twelve-photon entanglement. Based on the set of measurements, the corresponding fidelity can be derived, whereby an genuinely multi-partite entangled state yields an average fidelity above one half, $\bar{F} > 1/2$ [38]. Thus, this scheme provides a method of characterizing a multi-partite GHZ state, using only limited number of measurement settings.

Fidelity of the Cluster state

Estimating the fidelity of Cluster states has proven more difficult and is currently a work in progress by e.g. K. Tiurev *et al.* [39], examining the possibilities to provide a fidelity bound

based on a limited number of measurement settings. However, an entanglement *witness*, i.e. an indication of entanglement, can be extracted using only two measurement settings independent on the number of qubits involved

$$(1)\ \ \{\sigma_x^{(i)}, \sigma_z^{(i+1)}, \sigma_x^{(i+2)}, \sigma_z^{(i+3)}, ...\}, \qquad (2)\ \ \{\sigma_z^{(i)}, \sigma_x^{(i+1)}, \sigma_z^{(i+2)}, \sigma_x^{(i+3)}, ...\}, \tag{3.4.5}$$

where i denotes the qubit number [38]. Thus, a measurement sequence of this type projects the qubits into the z- and x-basis by turn. A similar scheme can be applied to the GHZ states, where the qubits are projected into the *same* basis in both sequences, i.e. $\{\sigma_x^{(i)}, \sigma_x^{(i+1)}, \sigma_x^{(i+2)}, \sigma_x^{(i+3)}, ...\}$ and $\{\sigma_z^{(i)}, \sigma_z^{(i+1)}, \sigma_z^{(i+2)}, \sigma_z^{(i+3)}, ...\}$, which resembles the measurement settings introduced in previous paragraph.

3.5 Summary

Two types of multi-partite entangled states were introduced in this chapter, namely the GHZ- and the Cluster-state. The fidelity of the former can be determined using $N + 1$ measurement settings, while the latter proves to be more demanding. However, one may construct an entanglement witness based on only two measurement settings.
Both states can be realized through the use of the entanglement protocol given in Section 3.3, which depends on the principles introduced in Chapter 2, apart form the optical π-pulses - these are the main subject of the next chapter.

Chapter 4

Characterization of the Time-bin Interferometer

The main focus of this chapter includes the theoretical analysis together with a physical characterization of the time-bin interferometer (TBI), operating as a double-pass Franson interferometer. In regards to the entanglement protocol, this chapter considers the creation and manipulation of the time-encoded photonic qubits.
The workings of the TBI can be composed into two distinct parts: The *excitation*- and *detection*-interferometer. The former creates the optical π-pulses used to excite the QD (as discussed in Section 3.3), while the latter enables detection and analysis of the photonic qubits, based on the spin-state of the QD.
Key applications and corresponding settings of the TBI will be presented, along with measurements showing agreement between the physical model and the experimental setup. A detailed description of the interferometer is given in Section 4.2 and 4.3, while a full schematic drawing can be found in Appendix B.1.

4.1 Introduction to the Time-bin Interferometer

This section seeks to give a brief introduction to photonic qubits, with focus on time-bin encoding. Furthermore, the *Jones formalism* will be presented, being central to the physical analysis of the TBI.

4.1.1 Time-bin Encoded Qubits

As stated in the introduction of this thesis, one requires a robust way of transferring information over a great distance in order to realize many applications proposed in the field of quantum communication. To this aim, the photon naturally poses a suitable candidate, not only due to its inherent speed, but also its ability to realize a two-level system in several ways, e.g. encoding the information in its polarization $\{|H\rangle, |V\rangle\}$, frequency $\{|\omega_0\rangle, |\omega_1\rangle\}$ or photon-number $\{|\emptyset\rangle, |1\rangle\}$. In this work however, the photonic qubit is time-bin encoded, i.e. the information is encoded in the arrival time $\{|e\rangle, |l\rangle\}$, where $e(l)$ denotes the early(late) photon. This method has a few advantages; for instance, given a photon is lost or otherwise not detected, the corresponding state is not valid and can therefore be discarded, as

opposed to the photon-number encoding. Here, a lost photon would influence the state - it is hard to distinguish a vacuum state $|\emptyset\rangle$ and the original state $|1\rangle$, if a photon was lost. Furthermore, though polarization encoding is typically the method of choice in free-space optics, due to the many ways of effective manipulation of the polarization, it is not very convenient if ones wishes to use optical fibers. Even for polarization maintaining fibers, it is difficult to preserve the correct polarization over a long distance. This however, is not an issue if one uses the time-bin encoded method, making it well suited for fiber-based applications.

4.1.2 Jones Formalism and Phase Retarders

A convenient way of expressing the polarization state of an electric field, is through the use of the so-called Jones vector formalism (or Jones calculus). This formalism will be used to characterize the performance of the TBI using classical fields, where fully polarized light[1] is represented by a Jones vector, while linear optical components such as mirrors, lenses and waveplates, are expressed by Jones matrices. For a given E-field the Jones vector has the form

$$\vec{E} = \begin{pmatrix} E_H \\ E_V \end{pmatrix}, \tag{4.1.1}$$

where E_H is the horizontal and E_V is the vertical component. The Jones matrices $\mathbf{M}_J$ are thus operators acting on the input vector, that is $\vec{E}_{\text{Out}} = \mathbf{M}_J \vec{E}_{\text{In}}$. Crucial for the analysis of the TBI are the following matrices:

$$M_{\text{LP}}(\theta) = e^{-i\pi/4} \begin{pmatrix} \cos^2(\theta) & \cos(\theta)\sin(\theta) \\ \cos(\theta)\sin(\theta) & \sin^2(\theta) \end{pmatrix}, \tag{4.1.2}$$

$$M_{\text{HWP}}(\theta) = e^{-i\pi/2} \begin{pmatrix} \cos^2(\theta) - \sin^2(\theta) & 2\sin(\theta)\cos(\theta) \\ 2\sin(\theta)\cos(\theta) & \sin^2(\theta) - \cos^2(\theta) \end{pmatrix}, \tag{4.1.3}$$

$$M_{\text{QWP}}(\theta) = e^{-i\pi/4} \begin{pmatrix} \cos^2(\theta) + i\sin^2(\theta) & (1-i)\sin(\theta)\cos(\theta) \\ (1-i)\sin(\theta)\cos(\theta) & i\cos^2(\theta) + \sin^2(\theta) \end{pmatrix}, \tag{4.1.4}$$

$$M_{\text{ABM}}(\theta, \phi, \Phi) = e^{-i\Phi/2} \begin{pmatrix} \cos^2(\theta) + e^{i\Phi}\sin^2(\theta) & (1-e^{i\Phi})e^{-i\phi}\cos(\theta)\sin(\theta) \\ (1-e^{i\Phi})e^{i\phi}\cos(\theta)\sin(\theta) & e^{i\Phi}\cos^2(\theta) + \sin^2(\theta) \end{pmatrix}, \tag{4.1.5}$$

where $M_{\text{LP}}(\theta)$ describes a Linear Polarizer (LP) with the angle of transmission at θ from horizontal, $M_{\text{HWP}}(\theta)$ ($M_{\text{QWP}}(\theta)$) denotes a Half-waveplate (Quarter-waveplate) with fast axis angled at θ w.r.t. horizontal and finally $M_{\text{ABM}}(\theta, \phi, \Phi)$ corresponds to any arbitrary birefringent material acting as phase retarder. The latter being described by the retardation Φ between fast and slow axis, ϕ denotes the circularity ($\phi = 0$ for linear retarders) and θ is the angle between fast axis w.r.t. horizontal.
The final Jones matrix that needs introduction is that of the Beam-splitter (BS)

$$M_{\text{BS}} = \begin{pmatrix} t & r'e^{i\xi_2} \\ re^{i\xi_1} & t' \end{pmatrix}, \tag{4.1.6}$$

[1] For random/partial polarized light can be described using Mueller Calculus.

where $\{t, t', r, r'\}$ are real numbers describing the reflection/transmission amplitudes, while $\{e^{i\xi_1}, e^{i\xi_2}\}$ denotes the phase difference between the reflected and transmitted part from a given input port [40]. In the case of a perfect 50/50 BS, the amplitudes and phase parameters takes the following values: $\{t, t', r, r'\} = 1/\sqrt{2}$ and $\{\xi_1, \xi_2\} = \pi/2$.

So far, the vector space has been restricted to two dimensions, namely the two basis states for the polarization. However, including the two temporal modes, e.g. early and late mode, gives a four-dimensional vector space. As a consequence, the E-field vector introduces at the beginning of this section needs to be redefined. Given two temporal modes a and b, with each their polarization degree of freedom (H or V), the total E-field takes the form

$$\vec{E} = \begin{pmatrix} a_H \\ b_H \\ a_V \\ b_V \end{pmatrix}, \tag{4.1.7}$$

which shall be used during the analysis of the detection interferometer (Section 4.3.1).

The Electro-Optic Modulator

At the centre of the detection interferometer is a resonant Electro-Optic Modulator (EOM). This device enables polarization modulation of the incoming light, by applying an AC-voltage across an optically active crystal within the EOM. As a result, the birefringence of the crystal can be changed due to the Pockels effect. The refractive index for light polarized parallel and perpendicular to the optical axis of the crystal can therefore be altered by varying the amplitude of the electric field [41]. In this particular setup, a resonant EOM from QUBIG[42] with a Lithium Tantalate (LT) crystal angled at 45 degrees w.r.t. horizontal is used. From Eq. 4.1.5 describing an arbitrary birefringent material, the corresponding Jones matrix for the EOM reads

$$M_{\text{EOM}}(\Phi) = M_{\text{ABM}}(\theta = 45^o, \phi = 0, \Phi) = \frac{e^{-i\Phi/2}}{2} \begin{pmatrix} 1 + e^{i\Phi} & 1 - e^{i\Phi} \\ 1 - e^{i\Phi} & 1 + e^{i\Phi} \end{pmatrix}. \tag{4.1.8}$$

It is worth noting, that for $\Phi = \pm\pi$ or $\Phi = \pm\pi/2$, the EOM acts as a half-waveplate (HWP) or quarter-waveplate (QWP) angled at $\theta = \pm\pi/4$ w.r.t horizontal, respectively. Furthermore, for $\Phi = 0$ the identity matrix I is obtained, and thus no transformation is performed. Experimentally however, the phase modulation $\Phi(t)$ is time dependent, as the EOM is controlled by an AC-voltage. In this case, the phase modulation can be expressed as

$$\Phi(t) = A\sin(\omega t + \alpha), \tag{4.1.9}$$

where A and ω are the modulation amplitude and frequency, while α denotes the phase modulation in respect to $\Phi(t)$. These parameters can all be controlled experimentally, dependent on the required phase retardation. Here A is proportional to amplitude of the applied voltage, α is controlled electronically, while ω is fixed at half the frequency of the pulse repetition rate of the Mira-laser[2], $\omega = \frac{f_{rep}}{2} \approx 36$ MHz. The latter allows for different phase modulation of two subsequent pulses, which will become apparent in Section 4.3.

[2]For more information regarding the lasers employed in this thesis, see Appendix C.1 and Section 5.1.

4.2 The Excitation Interferometer

The excitation interferometer is responsible for the creation of two temporally separated pulses with equal intensity. This is realized by spitting a single optical pulse, generated by the Mira-laser, into two paths; the short and the long path. In addition to this, the relative phase between the two pulses is to be controlled, while keeping the other parameters constant. The latter allows the photonic qubit to be measured in different bases, which will be described in greater detail in Section 4.3.
The excitation interferometer is thus essential towards realizing the entanglement protocol, as it creates the optical π-pulses utilized for the excitation of the QD - hence its name.

4.2.1 Theoretical Analysis of the Excitation Interferometer

Through the use of the Jones formalism, the appropriate settings of the excitation interferometer will now be derived, for which the intensity between the two pulses remains equal, while sweeping the relative phase. A detail overview of the excitation interferometer is presented in Fig. 4.1, where the most essential components are shown.

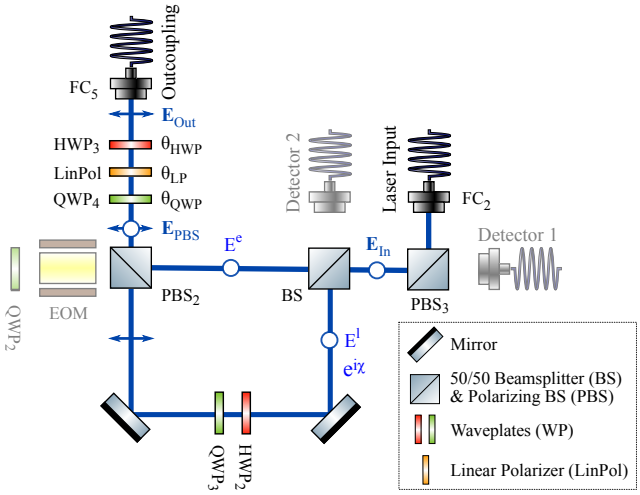

Figure 4.1: Schematic drawing of the excitation interferometer for generation of early and late pulses given a single pulse input. For simplicity, only the most relevant optical components are included (see Fig. B.1 for complete overview). See main text for detailed explanation of this setup.

Starting at the input of the excitation interferometer (FC_2), the E-field is given by

$$\vec{E}_{\text{In}} = \begin{pmatrix} 0 \\ 1 \end{pmatrix}, \tag{4.2.1}$$

which is vertically polarized and for simplicity has unit amplitude. The pulse is divided into two components at the BS; the *early* and the *late* pulse, separated by $\Delta\tau \approx 11.83$ ns upon recombining at PBS_2, due to the spatial difference in the two paths of the interferometer.

After the two pulses merge at PBS_2, the E-field for the early and late pulse are

$$\vec{E}^e_{\mathrm{PBS}} = E^e \begin{pmatrix} 0 \\ 1 \end{pmatrix} \qquad \text{and} \qquad \vec{E}^l_{\mathrm{PBS}} = e^{i\chi} E^l \begin{pmatrix} 1 \\ 0 \end{pmatrix}, \tag{4.2.2}$$

where the $e(l)$ superscript denotes early(late) and $E^e(E^l)$ is the transmission(reflection) of the E-field by the BS. Energy conservation is assumed for the latter, $|E^e|^2 + |E^l|^2 = 1$. Defining the phase of the short path to be zero, $e^{i\chi}$ is the total phase accumulated during the long interferometer path, since only the phase difference is relevant. Lastly, the waveplates in the long path (HWP_2 and QWP_3) are assumed to perfectly transform vertically- to horizontally-polarized light.
Next to consider is the total transformation after PBS_2 consisting of two waveplates QWP_4 and HWP_3, with a linear polarizer (LP) in between. The main object of interest is the rotation of QWP_4 and LP, since this configuration is the key ingredient fulfilling the requirements for the excitation interferometer. The angle of the final HWP is set to $\theta_{\mathrm{HWP}} = \frac{\theta_{\mathrm{LP}}}{2}$, whereby the output polarization is kept horizontal at all times when coupling into the fiber coupler. Thus, at the outcoupling of the excitation interferometer (at FC_5), the final transformation takes the form

$$M_{\mathrm{Tot}} = M_{\mathrm{HWP}}\left(\frac{\theta_{\mathrm{LP}}}{2}\right) M_{\mathrm{LP}}(\theta_{\mathrm{LP}}) M_{\mathrm{QWP}}(\theta_{\mathrm{QWP}}) \tag{4.2.3}$$

$$= \left(\frac{1+i}{2}\right) \begin{pmatrix} \cos(\theta_{\mathrm{LP}}) - i\cos(\theta_{\mathrm{LP}} - 2\theta_{\mathrm{QWP}}) & \sin(\theta_{\mathrm{LP}}) + i\sin(\theta_{\mathrm{LP}} - 2\theta_{\mathrm{QWP}}) \\ 0 & 0 \end{pmatrix}, \tag{4.2.4}$$

for which the E-field and corresponding intensity for both the early and late pulse reads

$$E^e_{Out} = M_{\mathrm{Tot}} \vec{E}^e_{\mathrm{PBS}} = \left(\frac{1+i}{2}\right) \left(\sin(\theta_{\mathrm{LP}}) + i\sin(\theta_{\mathrm{LP}} - 2\theta_{\mathrm{QWP}})\right) E^e, \tag{4.2.5}$$

$$E^l_{Out} = M_{\mathrm{Tot}} \vec{E}^l_{\mathrm{PBS}} = \left(\frac{1+i}{2}\right) \left(\cos(\theta_{\mathrm{LP}}) - i\cos(\theta_{\mathrm{LP}} - 2\theta_{\mathrm{QWP}})\right) e^{i\chi} E^l, \tag{4.2.6}$$

$$I^e_{Out} = |E^e_{Out}|^2 = \frac{|E^e|^2}{2} \left(\sin^2(\theta_{\mathrm{LP}}) + \sin^2(\theta_{\mathrm{LP}} - 2\theta_{\mathrm{QWP}})\right), \tag{4.2.7}$$

$$I^l_{Out} = \left|E^l_{Out}\right|^2 = \frac{\left|E^l\right|^2}{2} \left(\cos^2(\theta_{\mathrm{LP}}) + \cos^2(\theta_{\mathrm{LP}} - 2\theta_{\mathrm{QWP}})\right). \tag{4.2.8}$$

So far it has been assumed, that the 50/50 BS and PBS work perfectly, which is quite good assumption as the PBS experimentally has demonstrated an extinction ratio of at least 500, while the splitting ratio of the BS was found to be 49/51, i.e. close to ideal[3]. Under this assumption, one can approximate $E^e \approx E^l$, whereby the intensity difference can be expressed as

$$\Delta I_{Out} = I^e_{Out} - I^l_{Out} = \sin^2(\theta_{\mathrm{LP}}) - \cos^2(\theta_{\mathrm{LP}} - 2\theta_{\mathrm{QWP}}). \tag{4.2.9}$$

For equal intensities, i.e. $\Delta I_{Out} = 0$, two solutions exist

$$\text{(i)} \quad \theta_{\mathrm{QWP}} = \frac{\pi}{4} + \frac{\pi}{2} n \qquad \text{or} \qquad \text{(ii)} \quad \theta_{\mathrm{LP}} = \theta_{\mathrm{QWP}} + \frac{\pi}{4}(1+n), \qquad n \in \mathbb{Z}, \tag{4.2.10}$$

[3]The effects of the splitting ratio of the BS will be examined more closely in Chapter 5.

yielding two configurations whereby the intensity between the two pulses is kept constant. This concludes the first main result in this section. However, integrating the excitation interferometer with the entanglement protocol requires a way of altering the relative phase using one of the two settings in Eq. 4.2.10.

The phase difference $\delta\phi$ between the early and late pulse can be derived from

$$\delta\phi = \mathrm{Arg}(E^e_{Out}) - \mathrm{Arg}(E^l_{Out}) \tag{4.2.11}$$

where Arg() refers to the principal value of the argument applied to a complex number, $z = x + iy$. Often, when computing the argument, the function $\mathrm{atan2}(y, x) = \mathrm{Arg}(z)$ is interchangeably used instead. In this case, the principal value is given in the range $-\pi < \mathrm{atan2}(y, x) \leq \pi$, for which the function is defined as

$$\mathrm{atan2}(y,x) = \begin{cases} \arctan\left(\frac{y}{x}\right) & \text{if } x > 0, \\ \arctan\left(\frac{y}{x}\right) + \pi & \text{if } x < 0 \text{ and } y \geq 0, \\ \arctan\left(\frac{y}{x}\right) - \pi & \text{if } x < 0 \text{ and } y < 0, \\ +\pi/2 & \text{if } x = 0 \text{ and } y > 0, \\ -\pi/2 & \text{if } x = 0 \text{ and } y < 0, \\ \text{undefined} & \text{if } x = 0 \text{ and } y = 0. \end{cases} \tag{4.2.12}$$

In Fig. 4.2 a numerical calculation of $\delta\phi$ is shown, together with black contour lines for $\Delta I_{Out} = 0$. In accordance with Eq. 4.2.10, the vertical contour lines are represented by the first solution (i), while the diagonal lines represent the second solution (ii). From this figure is becomes clear, that only the first solution, i.e. $\theta_{\mathrm{QWP}} = \frac{\pi}{4} + \frac{\pi}{2}n$ satisfies the given requirements as the relative phase can be controlled, oppose to the second solution where it remains constant.

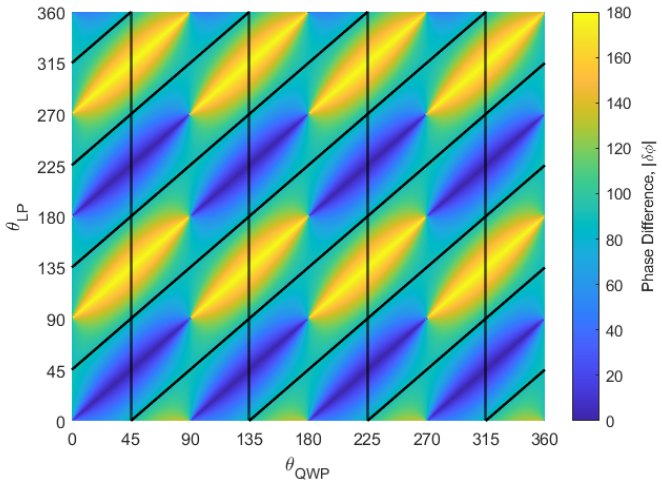

Figure 4.2: The phase difference between early and late pulse as a function of θ_{QWP} and θ_{LP} for $\chi = 0$. The black contour lines indicate where the intensity between the two pulses are equal. For $\theta_{\mathrm{QWP}} = \frac{\pi}{4} + \frac{\pi}{2}n$ the intensity remains constant, while the phase is altered by rotating θ_{LP}. All angles are in degrees.

Thus, a simple solution appears; keep QWP_4 constant at e.g. $\theta_{\mathrm{QWP}} = \pi/4$ and rotate the linear polarizer θ_{LP}, whereby two temporally separated pulses with equal intensity are created for which the relative phase can be controlled. This concludes the theoretical analysis of the excitation interferometer as all requirements towards to entanglement protocol are met.

4.2.2 Physical Characterization of the Excitation Interferometer

Based on the theoretical analysis of the excitation interferometer, this section seeks to quantify the performance of the actual setup, i.e. to what extent the theoretical model agrees with the measurements carried out with the excitation interferometer. In other words, characterizing the relative intensity and phase between the early and late pulse are of main interest. However, an examination of the phase will be presented in Section 4.3.2 as it requires an introduction to the detection interferometer as well.

Intensity of the Early and Late Pulse

Letting $I^e(I^l)$ denote the intensity of the early(late) pulse, the *visibility* is defined as

$$V = \frac{I^e - I^l}{I^e + I^l} \tag{4.2.13}$$

ranging from $-1 \leq V \leq 1$. For $V = 0$ the pulses are of equal intensity, whereas for $V = 1(V = -1)$ only the early(late) pulse is visible. This parameter can be measured directly by coupling the output fiber of FC_5 to a photodetector, while keeping track of the arrival time for each pulse. Experimentally, this is realised by the use of a Superconducting nanowire single-photon detector (SNSPD) and a Time Tagger from Swabian Instruments [43]. In order to keep the intensity low, the Mira-laser is greatly attenuated using neutral-density (ND) filters. Thus, the visibility between the early and late pulse can be found by measuring the total photon counts in each time-window as a function of the θ_{QWP} and θ_{LP}. Specifically, the time-window is set to two nanoseconds centered at the middle of each pulse, while the integration time is one second for each setting.
A measurement of this type is presented in Fig. 4.3 (a) by the two-dimensional color map, where the black contour lines indicate the theoretically predicted settings for $\Delta I = 0$, which appears to align with the areas for $V = 0$. In order to investigate this further, Fig. 4.3 (b) shows the visibility as a function of the linear polarizer for $\theta_{\mathrm{QWP}} = 45^o$ (blue) and 90^o (red). The latter should ideally oscillate between $V = \pm 1$ by

$$\Delta I_{Out}(\theta_{\mathrm{QWP}} = 90^o, \theta_{\mathrm{LP}}) = -\cos(2\theta_{\mathrm{LP}}), \tag{4.2.14}$$

while the former should remain constant at $V(\theta_{\mathrm{QWP}} = 45^o, \theta_{\mathrm{LP}}) = 0$ for all angles. However, as the blue data set indicates, a small oscillation is still present for $\theta_{\mathrm{QWP}} = 45^o$, whereby both are fitted with a cosine. From this data, the average visibility gives $V(\theta_{\mathrm{QWP}} = 45^o) = 0.009 \pm 0.029$, meaning the ratio between the intensities is slightly shifted towards that of the early pulse. The red curve however, yields a visibility of $V(\theta_{\mathrm{QWP}} = 90^o) = \pm 0.995$ at $\theta_{\mathrm{LP}} = \{90^o, 180^o\}$, indicating a good extinction ratio between the two pulses, i.e. the linear polarizer transmits only the early(late) pulse for $\theta_{\mathrm{LP}} = 90^o(180^o)$. In the entanglement protocol however, only the settings for $\theta_{\mathrm{QWP}} = 45^o$ are of interest.

There are basically two parameters, which influence the visibility, that is (i) the angle of the θ_{QWP} and (ii) the coupling efficiency of each pulse into FC_5. The first parameter is clearly shown in Fig. 4.3 (b) as the visibility varies from $V \approx 0$ to $V \approx \pm 1$ as θ_{QWP} is rotated by 45 degrees. Thus, finding the optimal angle of the QWP is crucial. Lastly, the combined loss for each of the two excitation paths may vary, which ones needs to take into account. It turns out the long interferometer arm has a loss of 6-8% compared to the short path. This is expected, as the long path consists of several optical components, mainly lenses ensuring the laser remains collimated, while none are present in the short path. Varying the coupling efficiencies for each pulse can thus compensate for this additional loss.
In practice this results in the early(late) pulse having a coupling efficiency of $\approx 80\%(87\%)$ at FC_5. In other words, any deviation from $\theta_{\mathrm{QWP}} = \frac{\pi}{4} + \frac{\pi}{2}n$ will hence increase the amplitude of the visibility, while unbalanced coupling efficiencies alters the mean. The combination of these parameters are the main reason for the oscillation shown by the blue curve in Fig. 4.3 (b).

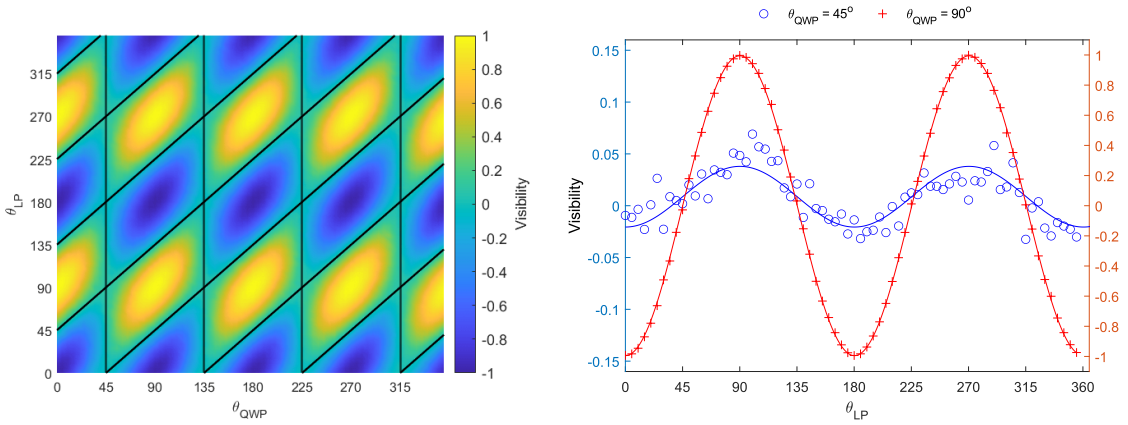

(a) Visibility as a function of θ_{QWP} and θ_{LP}.

(b) Visibility for $\theta_{\mathrm{QWP}} = 45^o$ (blue) and 90^o (red).

Figure 4.3: Experimental data: (a) The visibility as a function of the θ_{QWP} and θ_{LP}. The black contour lines presents the theoretical solution, whereby the relative intensity between the early and late pulse remains constant, i.e. $V = 0$. (b) The visibility as a function of θ_{LP} for two settings of QWP_4, each fitted with a cosine. For $\theta_{\mathrm{QWP}} = 45^o$ (blue) a slight deviation from $V = 0$ is present, due to imperfection in the experimental setup. Notice the varying scaling of the left/right y-axis.

4.3 The Detection Interferometer

The second part of the TBI consists of the so-called detection interferometer, responsible for the detection of the photons emitted by the QD upon relaxation.
Before going into the theoretical analysis, an essential part of the detection interferometer requires an introduction, namely the various time-bins and corresponding detection patterns. So far, the QD is said to emit a photon in two temporal modes, i.e. the early and late time-bin. This, however, requires some clarification once the photons propagate through the detection interferometer. Due to the fact that both the excitation- and

detection-interferometer share the same two paths[4], i.e. the short and the long path, a total of three time-bins are created in the detection interferometer, composed of four temporal modes. In terms of the photons arriving (e)arly or (l)ate in each interferometer, those are as follows:

$$|e\rangle : \{e, e\}, \qquad |m\rangle : \{e, l\} + \{l, e\}, \qquad |l\rangle : \{l, l\}.$$

Here the early(late) time-bin $|e\rangle$ ($|l\rangle$) corresponds to the short(long) path being taken in both interferometers, while the middle time-bin $|m\rangle$ corresponds to the short(long) path being taken in the excitation interferometer, and the long(short) path during the detection interferometer. In terms of the Bloch sphere, one may regard the $|e\rangle$ and $|l\rangle$ time-bin as the poles, while the middle time-bin $|m\rangle$ corresponds the equator as it consists of a superposition between $|e\rangle$ and $|l\rangle$.
Suppose there is a given setting, where each photon has an equal probability of taking the short or long path in the detection interferometer, thus 50% will go to the middle time-bin and 25% to the early and late time-bin - this setting will henceforth be known as *passive switching*. However, if one can choose whether the first and second photon should take either the short or long path, routing of photons into a desired time-bin is feasible, i.e. *active switching*. This principle is illustrated in Fig. 4.4, where the black line represents the passive switching. Following the Bloch sphere analogy, the green dashed line corresponds to active switching conducting measurements in the z-basis, while the blue dotted line corresponds to measurements performed in the x- and y-basis, i.e. around the equator. The main difference between to two methods is therefore the efficiency in which measurements can be executed by projecting the photonic qubits into a given basis. Experimentally this is realized by a QWP and an EOM, which will be explained in the next section.

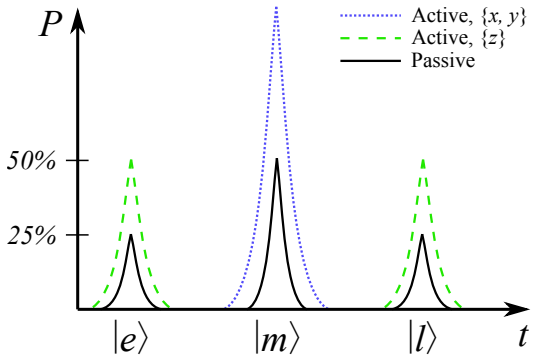

Figure 4.4: Illustration showing the difference between active- and passive-switching for the three time-bins. In the case of passive switching, the photon has an equal probability of taking either the short of long path of the detection interferometer. For active switching however, the photons are deterministically routed towards the desired time-bin.

Finally, is should be noted that sharing the same optical paths in both the excitation- and detection-interferometer, has the advantage of making it self-stabilizing. This means, any spatial change in the long or short path due to temperature variations or drifts in the position of the optical components does not affect the re-interference in the detection

[4]Once more, see Appendix B.1 for complete overview of the TBI.

interferometer. This assumption is only valid in the case where the spatial variations are on a timescale longer than the time it takes for the light to propagate through both parts of the TBI. As the latter is performed in the order of nanoseconds, this assumption should be accurate[5].

4.3.1 Theoretical Analysis of the Detection Interferometer

This section seeks to investigate the working principles of the detection interferometer in the same manner as were the case of the excitation interferometer. However, there are a few changes as one has to keep track of both the polarization and the temporal modes whereby the basis vector needs to be expanded to a four-dimensional vector space (see Eq. 4.1.7 for the new basis vector). Furthermore, in the classical Jones formalism utilized so far, the vector elements are proportional to the electric field, while the absolute square yields the intensity. For the entanglement protocol however, the input of the detection interferometer consists of single photons emitted by the QD. In this case, there is an important difference to the interpretation of these, that is the former being proportional to the *probability amplitude*, whereas the latter yields the *probability* of detection. Nevertheless, in order to keep the same notation and formalism used in the previous analysis, the classical Jones formalism will be utilized for this derivation and subsequently reinterpreted.

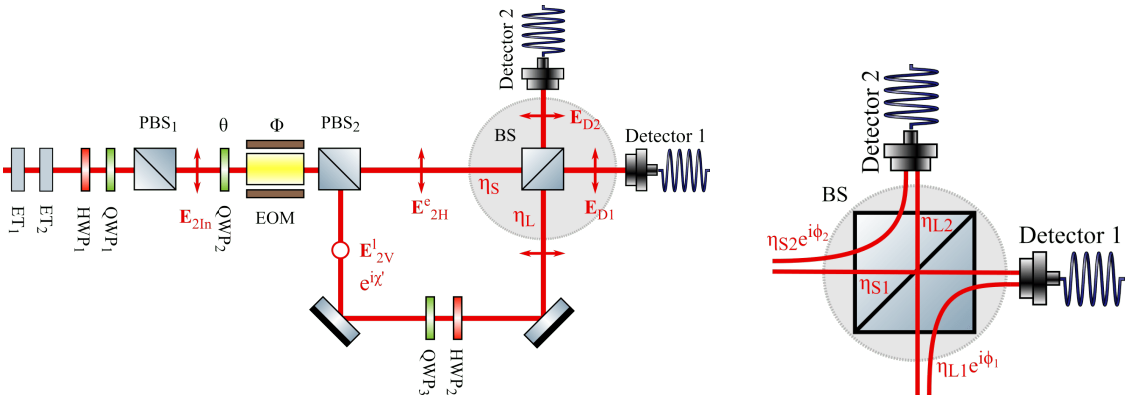

(a) Detection Interferometer. (b) Zoom-in at BS.

Figure 4.5: (a) Schematic drawing of the detection interferometer showing the most essential parts. Light is coupled into the interferometer from the left, where the beam once more is split into two paths at PBS_2. For full overview, see Fig. B.1 in Appendix B.1. (b) A zoom-in on the BS, showing the corresponding phase- and loss-parameters $\{\phi, \eta\}$ based on the path taken.

Following Fig. 4.5 (a), two etalons (ET) are placed at the beginning of the detection interferometer. These are used for frequency filtering[6], narrowing the spectral bandwidth to 1.91 GHz around the central frequency of the low energy transition of the QD, i.e. $|\Uparrow\rangle \leftrightarrow |\Uparrow\Downarrow, \uparrow\rangle$. The etalons are followed by two waveplates, enabling polarization control for maximal transmission by PBS_1. Hereafter, the E-field can be decomposed into an early

[5] An estimate on the actual stability will be given in Section 4.3.2.
[6] A more detailed description of the etalons, see Appendix C.2.

and late part, each being horizontally polarized

$$\vec{E}_{\text{2In}} = c_e \cdot \vec{E}^{e}_{\text{In,H}} + c_l \cdot \vec{E}^{l}_{\text{In,H}} = c_e \cdot \begin{pmatrix} 1 \\ 0 \\ 0 \\ 0 \end{pmatrix} + c_l \cdot \begin{pmatrix} 0 \\ 1 \\ 0 \\ 0 \end{pmatrix} = \begin{pmatrix} c_e \\ c_l \\ 0 \\ 0 \end{pmatrix}, \tag{4.3.1}$$

where the coefficients c_e and c_l are given in Eqs. 4.2.5 and 4.2.6, respectively.

Next is the QWP_2 and EOM, which is crucial to the detection interferometer as it enables the passive- and active-switching schemes by modulating the polarization and hence altering the amount of transmitted/reflected light by the following PBS. The concepts and workings of both the EOM and the switching schemes has previously been covered in Section 4.1.2 and at the beginning of this section. Thus, the total transformation due to the QWP and EOM yields[7]

$$M_{\text{EQ}}(\Phi_{\{e,l\}}, \theta) = \begin{bmatrix} C(\Phi_e)c_{HH}(\theta,\Phi_e) & 0 & C(\Phi_e)c_{VH}(\theta,\Phi_e) & 0 \\ 0 & C(\Phi_l)c_{HH}(\theta,\Phi_l) & 0 & C(\Phi_l)c_{VH}(\theta,\Phi_l) \\ C(\Phi_e)c_{HV}(\theta,\Phi_e) & 0 & C(\Phi_e)c_{VV}(\theta,\Phi_e) & 0 \\ 0 & C(\Phi_l)c_{HV}(\theta,\Phi_l) & 0 & C(\Phi_l)c_{VV}(\theta,\Phi_l) \end{bmatrix}, \tag{4.3.2}$$

where $\Phi_{\{e,l\}}$ denotes the retardation between the fast and slow axis of the EOM at the time of the early and late mode created in the excitation interferometer, while θ corresponds to the rotation of QWP_2. The matrix coefficients express the degree of polarization-transformation induced by QWP_2 and the EOM

$$c_{HH}(\theta,\Phi) = (1 - i\cos(2\theta))\cos(\Phi/2) + \sin(2\theta)\sin(\Phi/2), \tag{4.3.3}$$
$$c_{HV}(\theta,\Phi) = (i + \cos(2\theta))\sin(\Phi/2) - i\sin(2\theta)\cos(\Phi/2), \tag{4.3.4}$$
$$c_{VH}(\theta,\Phi) = (i - \cos(2\theta))\sin(\Phi/2) - i\sin(2\theta)\cos(\Phi/2), \tag{4.3.5}$$
$$c_{VV}(\theta,\Phi) = (1 + i\cos(2\theta))\cos(\Phi/2) + \sin(2\theta)\sin(\Phi/2), \tag{4.3.6}$$
$$C(\Phi) = \frac{e^{i(\pi/4-\Phi)}}{\sqrt{2}}, \tag{4.3.7}$$

where the first(second) subscript denotes the polarization of the incoming(outgoing) light, e.g. $c_{HV}(\theta,\Phi)$ yields to what extent the polarization is converted from horizontally into vertically. Thus, one can directly choose the basis of measurement by modulating the effective retardation of the QWP and EOM, which can be realised in various ways. However there are basically two methods

(i) Set $\theta = \pi/2$ and let the EOM work as a half-waveplate, i.e. $\Phi_\epsilon = \pi \cdot \epsilon$,

(ii) Set $\theta = \pi/4$ and let the EOM work as a quarter-waveplate, i.e. $\Phi_\epsilon = \pi/2 \cdot \epsilon$,

for $\epsilon = 1$. This parameter denotes the imperfections associated with the EOM[8].
Consequently, the greater the retardation between the fast and slow axis of the EOM, the

[7] This transformation in derived in Appendix B.2.

[8] The ϵ-parameter will be derived and described at the end of this section.

higher voltage is required. Thus, assuming the effective retardation is linear with the amplitude, the (ii) method requires only half the voltage compared to method (i).

Dependent of the retardation of the QWP and EOM, the incident light is once more split into two paths at PBS_2. As for the excitation interferometer, an additional phase χ' is introduced for the long path. If the TBI is truly self-stabilizing, the difference between χ and χ' should remain constant, i.e. $\frac{d}{dt}(\chi - \chi') = 0$. The corresponding operator, together with a PBS angled at 90 degrees w.r.t the incident beam, reads

$$M_{\mathrm{PL}} = \begin{bmatrix} 1 & 0 & 0 & 0 \\ 0 & 1 & 0 & 0 \\ 0 & 0 & e^{i\chi'} & 0 \\ 0 & 0 & 0 & e^{i\chi'} \end{bmatrix}, \qquad M_{\mathrm{PBS}} = \begin{bmatrix} t_H & ir_H & 0 & 0 \\ ir_H & t_H & 0 & 0 \\ 0 & 0 & t_V & ir_V \\ 0 & 0 & ir_V & t_V \end{bmatrix}. \tag{4.3.8}$$

Given a perfect PBS, i.e. $\{t_H, r_V\} = 1$ and $\{t_V, r_H\} = 0$, the E-field after PBS_2 is

$$\begin{aligned} \vec{E}_2 &= M_{\mathrm{PL}} M_{\mathrm{PBS}} M_{\mathrm{EQ}} \vec{E}_{2\mathrm{In}} && (4.3.9)\\ &= \vec{E}^e_{2\mathrm{H}} + \vec{E}^l_{2\mathrm{V}} && (4.3.10)\\ &= \begin{pmatrix} C(\Phi_e)c_{HH}(\theta, \Phi_{e,\epsilon})c_e \\ C(\Phi_l)c_{HH}(\theta, \Phi_{l,\epsilon})c_l \\ 0 \\ 0 \end{pmatrix} + \begin{pmatrix} 0 \\ 0 \\ C(\Phi_l)c_{HV}(\theta, \Phi_{l,\epsilon})e^{i\chi'}c_l \\ C(\Phi_e)c_{HV}(\theta, \Phi_{e,\epsilon})e^{i\chi'}c_e \end{pmatrix}, && (4.3.11) \end{aligned}$$

where vertically polarized light is assumed to transform perfectly into horizontally polarized during the long path. Thus, keeping track of the polarization is henceforth obsolete, since non of the remaining optical components are polarization depended. With this in mind, only the temporal modes are of interest at this point.

So far, only (e)arly and (l)ate mode has been considered. However, during the detection interferometer, a total of four temporal modes will be created as discussed in the beginning of this chapter. Thus, a changed of basis is required, keeping track of the temporal modes instead of the polarization. A such transformation is given by the following matrix, represented by the new basis $\{E_{SS}, E_{SL}, E_{LS}, E_{LL}\}$

$$M_{TP} = \begin{bmatrix} 1 & 0 & 0 & 0 \\ 0 & 0 & 0 & 1 \\ 0 & 1 & 0 & 0 \\ 0 & 0 & 1 & 0 \end{bmatrix}, \tag{4.3.12}$$

where the subscripts SS, SL/LS and LL denotes the short and long path for the excitation and detection interferometer, respectively. The E-field before the final BS is therefore expressed by

$$\vec{E}_{2el} = M_{TP}\vec{E}_2 = \begin{pmatrix} C(\Phi_e)c_{HH}(\theta, \Phi_{e,\epsilon})c_e \\ C(\Phi_e)c_{HV}(\theta, \Phi_{e,\epsilon})e^{i\chi'}c_e \\ C(\Phi_l)c_{HH}(\theta, \Phi_{l,\epsilon})c_l \\ C(\Phi_l)c_{HV}(\theta, \Phi_{l,\epsilon})e^{i\chi'}c_l \end{pmatrix} = \begin{pmatrix} E^e_{SS} \\ E^m_{SL} \\ E^m_{LS} \\ E^l_{LL} \end{pmatrix}. \tag{4.3.13}$$

Lastly, the mapping of the BS to Detector 1 (D_1) and Detector 2 (D_2) is required. Letting η_{ij} denote the accumulated loss, where the subscripts $i = \{S, L\}$ represents the Short/Long interferometer path and $j = \{1, 2\}$ denotes D_1/D_2, a total transformation can be constructed. Consequently, the matrix describing the transformation of the 50/50-BS and the corresponding loss-parameter is given by

$$M_{\mathrm{BS}}(\eta_{ij}, \phi_{\{1,2\}}) = \frac{1}{\sqrt{2}} \begin{bmatrix} \eta_{S1} & 0 & 0 & 0 \\ \eta_{S2} e^{i\phi_2} & 0 & 0 & 0 \\ 0 & \eta_{L1} e^{i\phi_1} & \eta_{S1} & 0 \\ 0 & \eta_{L2} & \eta_{S2} e^{i\phi_2} & 0 \\ 0 & 0 & 0 & \eta_{L1} e^{i\phi_1} \\ 0 & 0 & 0 & \eta_{L2} \end{bmatrix}, \tag{4.3.14}$$

where $0 \leq \eta_{ij} \leq 1$ and $\phi_{\{1,2\}}$ denotes the angle of incidence for the two paths, usually set to $\phi = \pi/2$ by default. As a general rule of thumb, it is expected that $\eta_L < \eta_S$, since more optical components are present in the long path. The loss-parameters are displayed in Fig. 4.5 (b), which can be measured directly in the laboratory.
Including the final transformation M_{BS}, the E-field at the two detectors read

$$\vec{E}_{D_{1,2}} = \begin{pmatrix} E^e_{D_1} \\ E^e_{D_2} \\ E^m_{D_1} \\ E^m_{D_2} \\ E^l_{D_1} \\ E^l_{D_2} \end{pmatrix} = M_{\mathrm{BS}}(\eta_{ij}, \phi_{\{1,2\}}) \vec{E}_{2el}. \tag{4.3.15}$$

Taking the absolute square of each vector element of $\vec{E}_{D_{1,2}}$ gives the intensity for a given temporal mode and detector. However, once the entanglement protocol is enabled, the E-field and intensity are not of interest, but instead the probability amplitude and corresponding probability of photon detection. Thus, converting the E-field calculated in Eqs. 4.2.5 and 4.2.6 into probability amplitudes for the early and late pulse, the total state after the excitation interferometer is given by

$$|\Psi\rangle_e = c_e |\psi\rangle_e + c_l |\psi\rangle_l = \begin{pmatrix} c_e \\ c_l \\ 0 \\ 0 \end{pmatrix}, \tag{4.3.16}$$

where the probability amplitude for the early and late pulse are expressed by the coefficients

$$c_e = \left(\frac{1+i}{2}\right) \left(\sin(\theta_{\mathrm{LP}}) + i\sin(\theta_{\mathrm{LP}} - 2\theta_{\mathrm{QWP}})\right), \tag{4.3.17}$$

$$c_l = \left(\frac{1+i}{2}\right) \left(\cos(\theta_{\mathrm{LP}}) - i\cos(\theta_{\mathrm{LP}} - 2\theta_{\mathrm{QWP}})\right) e^{i\chi}, \tag{4.3.18}$$

fulfilling the normalization requirement, $|c_e|^2 + |c_l|^2 = 1$. Applying all the transformation

matrices derived in this section, the final state of the detection interferometer reads

$$|\Psi\rangle_{D_{1,2}} = M_{\mathrm{BS}}(\eta_{ij}, \phi_{\{1,2\}} = \pi/2) M_{\mathrm{TP}} M_{\mathrm{PL}} M_{\mathrm{PBS}} M_{\mathrm{EQ}}(\Phi_{\{e,l\},\epsilon}, \theta) |\Psi\rangle_e \Rightarrow \tag{4.3.19}$$

$$\begin{pmatrix} |1^e_{D_1}, \emptyset^e_{D_2}\rangle \\ |\emptyset^e_{D_1}, 1^e_{D_2}\rangle \\ |1^m_{D_1}, \emptyset^m_{D_2}\rangle \\ |\emptyset^m_{D_1}, 1^m_{D_2}\rangle \\ |1^l_{D_1}, \emptyset^l_{D_2}\rangle \\ |\emptyset^l_{D_1}, 1^l_{D_2}\rangle \end{pmatrix} = \frac{1}{\sqrt{2}} \begin{pmatrix} \eta_{S1} C(\Phi_e) c_{HH}(\theta, \Phi_{e,\epsilon}) c_e \\ i\eta_{S2} C(\Phi_e) c_{HH}(\theta, \Phi_{e,\epsilon}) c_e \\ -\eta_{L1} C(\Phi_e) c_{HV}(\theta, \Phi_{e,\epsilon}) e^{i\chi'} c_e + \eta_{S1} C(\Phi_l) c_{HH}(\theta, \Phi_{l,\epsilon}) c_l \\ i\eta_{L2} C(\Phi_e) c_{HV}(\theta, \Phi_{e,\epsilon}) e^{i\chi'} c_e + i\eta_{S2} C(\Phi_l) c_{HH}(\theta, \Phi_{l,\epsilon}) c_l \\ -\eta_{L1} C(\Phi_l) c_{HV}(\theta, \Phi_{l,\epsilon}) e^{i\chi'} c_l \\ i\eta_{L2} C(\Phi_l) c_{HV}(\theta, \Phi_{l,\epsilon}) e^{i\chi'} c_l \end{pmatrix}, \tag{4.3.20}$$

expressing the probability amplitude of single photon detection at each detector $\{D_1, D_2\}$ and time-bin $\{|e\rangle, |m\rangle, |l\rangle\}$. This relation contains all the information of the TBI and concludes the derivation of the detection interferometer using the Jones formalism. The remaining part of the section investigates the probabilities in each detector under the influence of the passive- and active-switching scheme using the EOM. However, before this can be derived, the imperfections of the latter has to be examined more closely.

Limitations and Imperfections of the EOM

In the case where no voltage is applied across the EOM, no transformation should occur. It turns out, that experimentally this is *not* the case. It seems there is some arbitrary transformation in the system even when the EOM is off, which also affects the transformation once the EOM is turned on. Unfortunately, it has not been possible to identity the cause of the behaviour. It should therefore be emphasised, that the model presented in this section is *not* universal, as it cannot describe the EOM perfectly. In fact, this model assumes the EOM operating as a half-waveplate, while its imperfections are to be derived under the assumption of a quarter-waveplate. Nevertheless, this approach shows strong agreement between the mathematical model and the experimental results presented at the end of this chapter. This could be evidence of an intrinsic phase-retardation in the EOM, which is not accounted for in this simplified model.

In Table 4.1 the settings of the EOM and QWP for active switching are shown. For passive switching, the EOM is turned off and ideally the QWP is set to $\theta_{\mathrm{QWP}} = \pi/4$, hence reflecting and transmitting equal amounts by the following PBS. However, due to the intrinsic phase-retardation of the EOM, this angle was experimentally found to be $\theta_{\mathrm{QWP}} \approx 62^o$.

Active Switching	(i) Method			(ii) Method		
Basis	θ_{QWP}	Φ_e	Φ_l	θ_{QWP}	Φ_e	Φ_l
x- or y-basis	$\pi/2$	π	0	$\pi/4$	-$\pi/2$	+$\pi/2$
z-basis	$\pi/2$	0	π	$\pi/4$	+$\pi/2$	-$\pi/2$

Table 4.1: The ideal settings of the QWP_2 and EOM for different measurements bases while the active switching scheme is enabled.

Besides the intrinsic phase-retardation of the EOM, a limiting factor is the extinction ratio, i.e. how well it transforms one polarization into another. In the data sheet from

QUBIG [42], the manufacturer claims an AC extinction ratio of 1:26. For this particular setup, the ratio was measured to be 1:20, i.e. slightly lower than reported. In order to include this imperfection, an error term ϵ is introduced, which alters the phase parameters Φ_l and Φ_e and thereby simulates the effects of the finite extinction ratio

$$\Phi_{e,\epsilon} = \Phi_e \cdot \epsilon, \qquad \text{and} \qquad \Phi_{l,\epsilon} = \Phi_l \cdot \epsilon, \qquad 0 \leq \epsilon \leq 1. \tag{4.3.21}$$

The ϵ-parameter can be found by taking the ratio between the coefficients given in Eqs. 4.3.3 - 4.3.6 for the same temporal mode and tuning the EOM as a quarter-waveplate, i.e. (ii) method. For instance, looking at the early mode entering the detection interferometer, ϵ can be found by

$$\left|\frac{c_{VV}(\theta, \Phi_{e,\epsilon})}{c_{VH}(\theta, \Phi_{e,\epsilon})}\right|^2 = \left|\frac{c_{HH}(\theta, \Phi_{e,\epsilon})}{c_{HV}(\theta, \Phi_{e,\epsilon})}\right|^2 = R_e \Rightarrow \epsilon = 0.72, \tag{4.3.22}$$

where $R_e = 20$ is the experimentally determined extinction ratio, $\theta = \pi/4$ and $\Phi_{e,\epsilon} = \pi/2 \cdot \epsilon$ (i.e. measurement performed in z-basis). For the x- or y-basis one needs to take the reciprocal value, as the opposite transformation is required. The same applies for the late mode. Thus, a relation between the extinction ratio R_e and ϵ is established, which will be used to derive the probabilities in each detector and time-bin using Eq. 4.3.20. Furthermore, all of the following probabilities are henceforth derived using the (i) method presented in Table 4.1.

Active Switching - Measurements Performed in *x*- or *y*-basis

A measurement performed in the x or y-basis using the active switching scheme results in early(late) photons created by QD upon emission being reflected(transmitted) to the long(short) path of the detection interferometer. Thus, photons arrive in the middle time-bin. From Table 4.1, measurement performed in the x- or y-basis are given by

$$x\text{- or } y\text{-basis:} \qquad \theta = \pi/2, \quad \Phi_e = \pi, \quad \Phi_l = 0, \tag{4.3.23}$$

Inserting these values into Eq. 4.3.20, the probabilities of detecting a photon can be calculated. In the case of an ideal system with no losses or imperfections, the probabilities of photon detection are simplified to

$$P^m_{D1} = \left|\langle 1^m_{D_1}, \emptyset^m_{D_2}|\Psi\rangle_{D_{1,2}}\right|^2 = \frac{1}{2}\left|c_e - ic_l\right|^2, \tag{4.3.24}$$

$$P^m_{D2} = \left|\langle \emptyset^m_{D_1}, 1^m_{D_2}|\Psi\rangle_{D_{1,2}}\right|^2 = \frac{1}{2}\left|ic_e - c_l\right|^2, \tag{4.3.25}$$

for the middle time-bin, while the early and late yield $P^e_{D1} = P^e_{D2} = P^l_{D1} = P^l_{D2} = 0$, as expected. However, under the assumption of a lossy BS, non-unity coupling efficiencies and an imperfect EOM, the probabilities for the middle time-bins are expressed by

$$P^m_{D1,\epsilon} = \frac{1}{4}\left|(1-i)\Phi(\epsilon, \chi')\eta_{L1}c_e + i\sqrt{2}\eta_{S1}c_l\right|^2, \tag{4.3.26}$$

$$P^m_{D2,\epsilon} = \frac{1}{4}\left|(1+i)\Phi(\epsilon, \chi')\eta_{L2}c_e + \sqrt{2}\eta_{S2}c_l\right|^2, \tag{4.3.27}$$

while the early and late time-bins are given by

$$P^{e}_{D1,\epsilon} = \frac{1}{2}\left|\Theta(\epsilon)\eta_{S1}c_e\right|^2, \qquad P^{e}_{D2,\epsilon} = \frac{1}{2}\left|\Theta(\epsilon)\eta_{S2}c_e\right|^2, \tag{4.3.28}$$

$$P^{l}_{D1,\epsilon} = 0, \qquad P^{l}_{D2,\epsilon} = 0, \tag{4.3.29}$$

where the functions $\Theta(\epsilon)$ and $\Phi(\epsilon,\chi')$ read

$$\Theta(\epsilon) = \cos\left(\frac{\pi\epsilon}{2}\right)e^{\frac{\pi}{4}i(1-4\epsilon)}, \quad \Phi(\epsilon,\chi') = \sin\left(\frac{\pi\epsilon}{2}\right)e^{\frac{1}{4}i(\pi+4\chi'-4\pi\epsilon)}, \quad \text{for } 0\leq\epsilon\leq 1. \tag{4.3.30}$$

Thus, the probabilities in each time-bin and detector varies as a function of QWP_4 and LP in the excitation interferometer since $\Theta(\epsilon)$, $\Phi(\epsilon,\chi')$ and η_{ij} are constants defined by the imperfections in the optical setup. The latter is found experimentally by measuring the couplings efficiencies at each detector combined with the losses accumulated in the short and long interferometer paths. Generally, the couplings efficiencies are around 80%, while there is an additional 6-8% loss in the long interferometer path compared to the short. The corresponding detection probabilities in the middle time-bin are presented by the two-dimensional color map in Fig. 4.6 (a)-(b), showing each detector as a function of QWP_4 and LP. Note, these are normalized to present the relative detection probability.

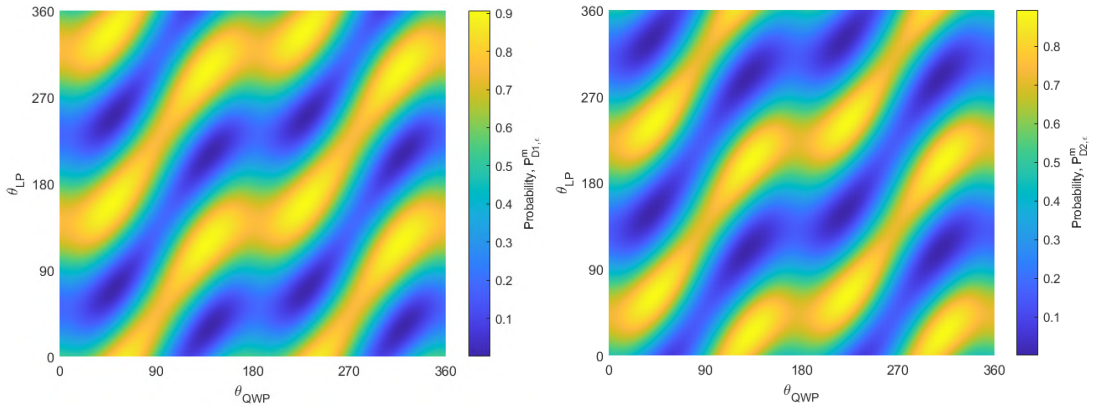

(a) Detector 1, Middle Time-bin.

(b) Detector 2, Middle Time-bin.

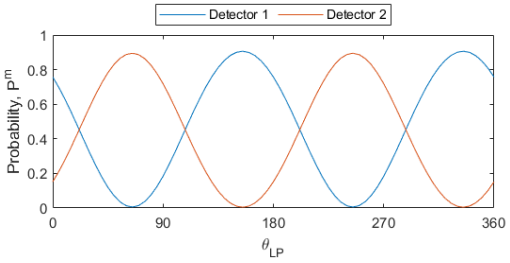

(c) Detection Probabilities for $\theta_{\mathrm{QWP}} = 45^o$.

Figure 4.6: Theoretical model with normalized detection probabilities: The probabilities $\{P^m_{D1,\epsilon}, P^m_{D2,\epsilon}\}$ of photon detection in detector $\{D_1, D_2\}$ as a function of θ_{QWP} and θ_{LP} for active switching in the middle time-bin using the x- or y-basis settings. Note the different scaling of the colorbars. Imperfections of the optical setup yield: $\eta_{S1} = 0.84$, $\eta_{S2} = 0.79$, $\eta_{L1} = 0.81$, $\eta_{L2} = 0.76$, $\epsilon = 0.72$ and $\chi = \chi' = 0$. All angles are presented in degrees.

From Fig. 4.6 (c), a clear anti-correlation between the two detectors becomes visible, due to the alternating phase-difference induced by QWP_4 and LP in the excitation interferometer. Furthermore, there is a slightly larger probability of getting a photon in Detector 1, as it has an better coupling efficiency, yielding a maximum(minimum) of 91% (0.5%) at $\theta_{\mathrm{LP}} = 155^o(65^o)$, while Detector 2 has a maximum(minimum) of 89% (0.4%) at $\theta_{\mathrm{LP}} = 65^o(155^o)$. The probabilities for the early time-bin are presented in Appendix B.3.

Active Switching - Measurements Performed in *z*-basis

Measurements carried out in the z-basis will result in photons arriving in the early and late time-bins. Therefore, using the following settings provided in Table 4.1

$$z\text{-basis:} \qquad \theta = \pi/2, \quad \Phi_e = 0, \quad \Phi_l = \pi, \tag{4.3.31}$$

the probabilities of photon detection takes the form

$$P^e_{D1,\epsilon} = \frac{1}{2}\left|\eta_{S1}c_e\right|^2, \qquad P^e_{D2,\epsilon} = \frac{1}{2}\left|\eta_{S2}c_e\right|^2, \tag{4.3.32}$$

$$P^m_{D1,\epsilon} = \frac{1}{2}\left|\Theta(\epsilon)\eta_{S1}c_l\right|^2, \qquad P^m_{D2,\epsilon} = \frac{1}{2}\left|\Theta(\epsilon)\eta_{S2}c_l\right|^2, \tag{4.3.33}$$

$$P^l_{D1,\epsilon} = \frac{1}{2}\left|\Phi(\epsilon,\chi')\eta_{L1}c_l\right|^2, \qquad P^l_{D2,\epsilon} = \frac{1}{2}\left|\Phi(\epsilon,\chi')\eta_{L2}c_l\right|^2. \tag{4.3.34}$$

For an ideal system the probabilities are reduced to the following simple expressions

$$P^e_{D1} = P^e_{D2} = \frac{1}{2}\left|c_e\right|^2, \qquad P^l_{D1} = P^l_{D2} = \frac{1}{2}\left|c_l\right|^2, \tag{4.3.35}$$

for the early and late time-bin, while the middle yields $P^m_{D1} = P^m_{D2} = 0$, as expected.
In the case where imperfections are included, the corresponding figure showing the probabilities of the early, middle and late time-bins are presented in Fig. B.3, Appendix B.3. Here the same detection pattern emerges from all the time-bins, but with different probabilities. Furthermore, Fig. B.5 in Appendix B.3 shows a data set using the EOM, which reveals the same detection pattern as predicted from the model.

Passive Switching

While passive switching is enabled (the EOM is off), the photons arrive in all time-bins. Therefore, using the following settings

$$\text{Passive:} \qquad \theta = \pi/4, \quad \Phi_e = 0, \quad \Phi_l = 0, \tag{4.3.36}$$

the probabilities of photon detection takes the form

$$P^e_{D1} = \frac{1}{4}\left|\eta_{S1}c_e\right|^2, \qquad P^e_{D2} = \frac{1}{4}\left|\eta_{S2}c_e\right|^2, \tag{4.3.37}$$

$$P^m_{D1} = \frac{1}{4}\left|\eta_{L1}e^{i\chi'}c_e - i\eta_{S1}c_l\right|^2, \qquad P^m_{D2} = \frac{1}{4}\left|\eta_{L2}e^{i\chi'}c_e + i\eta_{S2}c_l\right|^2, \tag{4.3.38}$$

$$P^l_{D1} = \frac{1}{4}\left|\eta_{L1}e^{i\chi'}c_l\right|^2, \qquad P^l_{D2} = \frac{1}{4}\left|\eta_{L2}e^{i\chi'}c_l\right|^2. \tag{4.3.39}$$

For an ideal system the probabilities for the middle time-bin are given by

$$P_{D1}^{m} = \frac{1}{4}\left|c_e - ic_l\right|^2, \qquad P_{D2}^{m} = \frac{1}{4}\left|c_e + ic_l\right|^2, \tag{4.3.40}$$

while $P_{D1}^{e} = P_{D2}^{e} = \frac{1}{4}\left|c_e\right|^2$ and $P_{D1}^{l} = P_{D2}^{l} = \frac{1}{4}\left|c_l\right|^2$ for the early and late time-bin.
This concludes the derivation of the detection probabilities using the active and passive switching schemes, whereby the performance of the TBI is examined in the following section.

4.3.2 Physical Characterization of the Detection Interferometer

This section presents an overview of the detection interferometer, linking the theoretical analysis with the experimental setup. This includes an examination of the relative phase between the early and late pulse and a demonstration of active switching. Furthermore, a way of estimating the stability of the TBI will be introduced. All characterizations are performed using a coherent state.

Phase Control and Stability

During the theoretical analysis of the excitation interferometer is was found that rotating the linear polarizer while keeping QWP_4 constant at $\theta_{\mathrm{QWP}} = \frac{\pi}{4} + \frac{\pi}{2}n$ allowed for equal intensity between the early and late pulse, while controlling the relative phase.
Experimentally, this can be verified by examining the middle time-bin. Operating the TBI under passive switching allows the early and late time-bin to be examined as well - their relative ratio should ideally remain constant, whereas the probability of photon detection in the middle time-bin oscillates between the two detectors. The latter can be derived from Eqs. 4.3.40, where the probability in each detector is proportional to $P_{D1}^{m} \propto |\cos(\theta_{\mathrm{LP}})|^2$ and $P_{D2}^{m} \propto |\sin(\theta_{\mathrm{LP}})|^2$. The corresponding oscillation is shown in Fig. 4.7 (a), where both detectors are fitted with a sine-squared as a function of the linear polarizer for $\theta_{\mathrm{QWP}} = 45^o$.

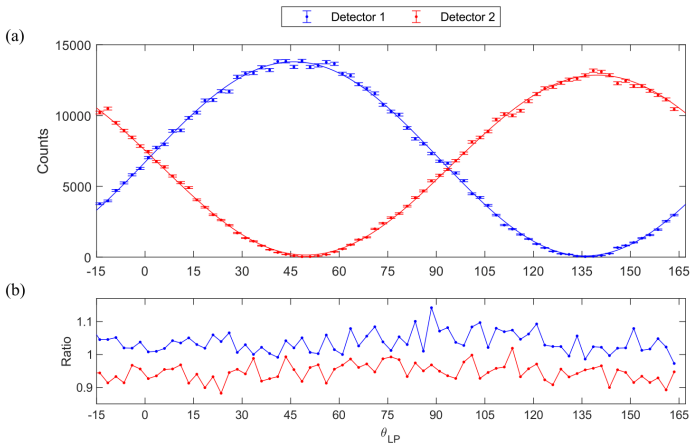

Figure 4.7: (a) Counts in the middle time-bin for each detector as a function of the angle of the linear polarizer, θ_{LP}. The measurements are performed using passive switching ($\mathrm{QWP}_2 = 62.8^o$) in the detection interferometer and $\theta_{\mathrm{QWP}} = \pi/4$. The errorbars assumes a Poisson-distribution, i.e. $\sigma = \sqrt{N}$, where N is to total counts for each setting. (b) The ratio between the early and late time-bin in each detector.

From the raw data, the maximum and minimum visibility using a classical field yields

$$V_{max}(\theta_{\mathrm{LP}} = 48.5^o) = 0.996 \pm 0.001, \qquad V_{min}(\theta_{\mathrm{LP}} = 136^o) = -0.995 \pm 0.001, \tag{4.3.41}$$

whereas the corresponding fit gives

$$V^f_{max}(\theta_{\mathrm{LP}} = 49.7^o) = 0.979 \pm 0.002, \qquad V^f_{min}(\theta_{\mathrm{LP}} = 136^o) = -0.987, \pm 0.001. \tag{4.3.42}$$

hence a slightly more conservative estimate. Furthermore, based on the corresponding angles of θ_{LP}, the two middle time-bins are approximately 87^o out of phase. This should ideally be 90^o, which could indicate a small imperfection in the optical setup. Additionally, due to different coupling efficiencies and non-perfect passive switching, there are less counts in the second detector. Comparing the total counts in each detector yields a difference of $\approx 5\%$, which agrees with the η_{ij}-parameters given in previous section.

In the context of the entanglement protocol, it should be noted that altering the relative phase between the early and late pulse corresponds to a rotation on the x-y-plane of the Bloch sphere. Hence, only a measurement performed in the middle time-bin allows the photonic qubits to be projected onto the x- or y-basis.
Furthermore, the stability of the TBI can be evaluated by monitoring the angle of θ_{LP} for either minimum or maximum visibility over a longer period of time. Leaving the TBI untouched for six days revealed a shift of 4.9 degrees, i.e. a little less than one degree per day. Putting this into the context of the theoretical section, this provides an estimate on $\frac{d}{dt}(\chi - \chi')$, which relates the accumulated phase of the two interferometer paths to one another. This parameter is sufficiently small for the implementation of the entanglement protocol, which typically takes several hours, after which the characterization can be repeated.

Finally, ahead of each measurement where passive switching is enabled, a calibration of QWP_2 is required in order to counter-balance the intrinsic transformation of the EOM. Ideally, there should be a point at which the ratio between counts in the early and late time-bin equals one, i.e. $D_1(C_e/C_l) = D_2(C_e/C_l) = 1$. However, due to different coupling efficiencies and losses in each path, one most find a compromise between each of the detectors. The data presented in Fig. 4.7 were measured after a calibration of this type yielding the following ratios: $D_1(e/l) = 1.037$ and $D_2(e/l) = 0.951$ for $\mathrm{QWP}_2 = 62.8^o$. Using this setting, the corresponding ratios in each detector are shown in Fig. 4.7 (b) as a function of the linear polarizer. The average ratio between the early and late time-bin gives

$$R_{D_1} = 1.038 \pm 0.031, \qquad R_{D_2} = 0.947 \pm 0.027. \tag{4.3.43}$$

Thus, slightly more counts are present in the early time-bin for Detector 1, while the opposite behavior is shown in Detector 2, which is comparable with the QWP_2 calibration.

Demonstration of Active Switching

The combination of the QWP_2 and EOM allows for active switching in the detection interferometer. A demonstration of its efficiency is presented in Fig. 4.8, showing the detection probabilities in the middle time-bin (using the x- and y-basis setting) as a function of QWP_4

and LP in the excitation interferometer. Each of the two waveplates are rotated stepwise by 7.5 degrees, after which there is an integration time of one second. The counts from every time-bin and detector are normalized to the total counts for each individual setting of the waveplates, which yields the relative detection probabilities in each detector.
A distinct feature of the middle time-bin is the "wave-like" detection pattern, which has the same shape as the model predicts (see Fig. 4.6). This is a direct consequence of the finite extinction ratio of the EOM, which in the model takes the form of the ϵ-parameter. However, if the EOM would operate perfectly, i.e. having an infinite extinction ratio, the corresponding detection pattern would consist of straight diagonal lines. For a complete overview of all time-bins, see Appendix B.3.3.

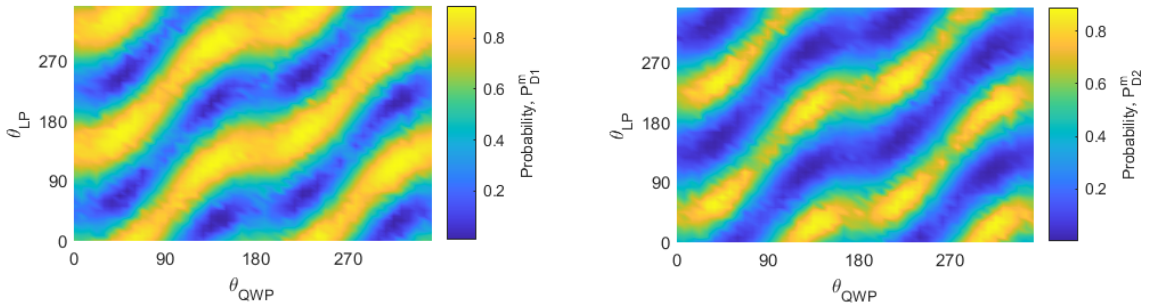

(a) Detector 1, Middle Time-bin.

(b) Detector 2, Middle Time-bin.

Figure 4.8: Experimental Data: The probabilities $\{P^m_{D1}, P^m_{D2}\}$ of photon detection in detector $\{D_1, D_2\}$ as a function of θ_{QWP} and θ_{LP} for active switching in the middle time-bin using the x- and y-basis settings. The data is normalized to all photon events for each setting of the waveplates. All angles are presented in degrees.

Particularly interesting are the angles of $\theta_{\text{QWP}} = \frac{\pi}{4} + \frac{\pi}{2}n$, as they provide the means of realizing the entanglement protocol, i.e. maintain equal intensity between the early and late excitation pulses. Hence, examining the photon detection events at e.g. $\theta_{\text{QWP}} = \frac{\pi}{4}$ gives a measure of the efficiency of the active switching scheme, with varying coupling efficiencies and losses for each detector and corresponding time-bin.
From the theoretical derivation, the detection probabilities for the middle time-bins are given by Eqs. 4.3.26 and 4.3.27. These are depicted at the solid lines in Fig. 4.9 (a), whereas each data-point corresponds to the detection probabilities for $\theta_{\text{QWP}} = \frac{\pi}{4}$, that is the measurement presented in the previous figure (Fig. 4.8). The data set for the middle time-bin yields a maximum(minimum) detection probability of $92.0 \pm 0.8\%$ ($1.2 \pm 0.1\%$) at $\theta_{\text{LP}} = 157.5^o(67.5^o)$ for Detector 1, while Detector 2 has a maximum(minimum) of $88.4 \pm 0.9\%$ ($0.6 \pm 0.1\%$) at $\theta_{\text{LP}} = 67.5^o(157.5^o)$ whereby the two detectors are 90^o out of phase as expected. Based on the maximum probability in each detector, this measurement demonstrates an average efficiency of $90.2 \pm 0.6\%$ for the active switching scheme.

The advantages of active switching become apparent if one considers the case of multiple qubits, i.e. introducing a stream of photonic qubits to the entanglement protocol. Under the assumption of an ideal system, the active switching enables deterministic routing of photons and the measurement basis of the photonic qubits may therefore be chosen directly by

the settings of the EOM. This is shown in Fig. 4.9 (b), displaying the detection efficiency as a function of the number of photonic qubits. The perfect EOM yields unit efficiency (blue) while passive switching (yellow) routes half the photons through the long/short path. However, as the EOM has an finite extinction ratio of $R_e = 20$, its efficiency reads 95% (red) if no losses or other imperfections are included. Thus, if one wishes to perform measurements using multiple photons, active switching is required as the detection efficiency otherwise drops rapidly.

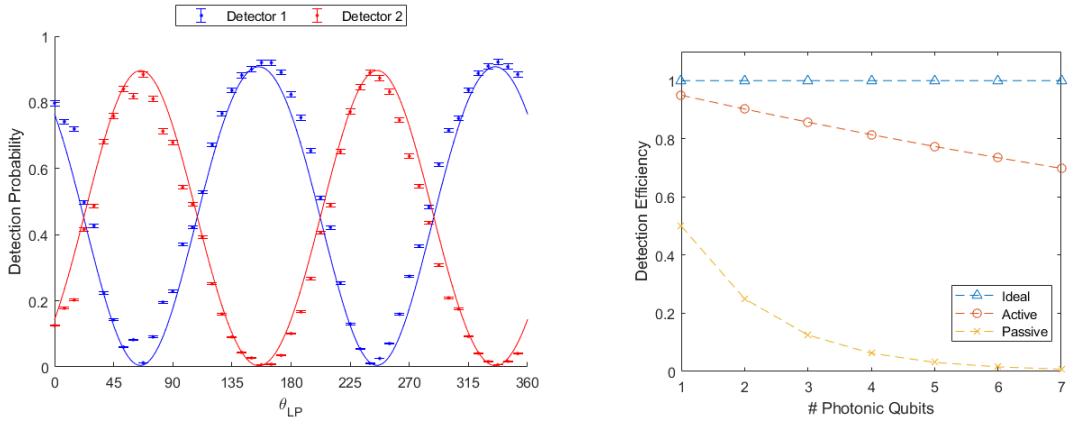

(a) Detection Probability, Middle Time-bin.

(b) Efficiencies.

Figure 4.9: (a) The normalized detection probabilities $\{P^m_{D1}, P^m_{D2}\}$ at $\theta_{\text{QWP}} = \frac{\pi}{4}$ as a function of θ_{LP} for active switching in the middle time-bin using the x- or y-basis settings. The solid lines corresponds to Eqs. 4.3.26 and 4.3.27. (b) Detection efficiencies for active and passive switching presented by the red and yellow lines, respectively.

4.4 Summary

The overall characterization of the TBI is best summarized by examining the excitation- and detection-interferometer individually.

The excitation interferometer generates two optical pulses separated by $\Delta\tau \approx 11.83$ ns, where the intensity and relative phase are controlled by a QWP and linear polarizer. Adjusting the former to $\theta_{\text{QWP}} = \frac{\pi}{4} + \frac{\pi}{2}n$ and sweeping the angle of the latter, alters the relative phase between the two pulses, while keeping the intensity constant. These findings has been verified experimentally, making the excitation interferometer a suitable system towards the realization of the optical π-pulses used for resonant excitation in entanglement protocol.

The detection interferometer creates three time-bins $\{|e\rangle, |m\rangle, |l\rangle\}$ upon the re-interference of the photons emitted by the QD. The measurement-basis of the photonic qubits can be altered by QWP_2 and the EOM and hence project the photonic qubits into the x, y, or z-basis using the switching schemes. The latter has been demonstrated experimentally and provides the means to scale the number of photonic qubits in a given sequence. Furthermore, the self-stabilizing effect of the TBI has been presented and the classical visibility was probed by a coherent state, yielding a visibility of $V = 0.995 \pm 0.001$ between the two detectors.

Chapter 5

Characterization of the Single-Photon Source

The quality of a single-photon source is mainly characterized by two parameters, namely its *purity* and *indistinguishability*. The former relies on photon statistics to quantify the performance of the emitter, i.e. assess the nature of the single-photons, while the latter is based on two-photon interference to determine the overlap of two wave-packets. The aim of this chapter is hence the investigation of those parameters, and how they readily can be measured by the Time-bin Interferometer. However, a fundamental requirement for both quantities is the resonant excitation of the QD, utilizing the optical pulses generated by the Mira-laser. Consequently, this chapter begins with a characterization of the latter, focusing on the optical π-pulses.

5.1 Characterization of the Excitation Pulse

The resonant excitation of X^+, i.e. the optical π-pulses used to excite the low-energy transition $|\Uparrow\rangle \rightarrow |\Uparrow\Downarrow, \uparrow\rangle$, are generated by the Mira-laser [44]. The latter has a broad bandwidth, emitting pulses of ≈ 4 ps duration with a repetition rate of $f_{rep} \approx 72$ MHz. However, in order to excite the correct transition, tuning the central frequency of the excitation pulse along its bandwidth is an essential requirement.
This can be achieved using tunable frequency filters allowing one to narrow down the spectra of the Mira-laser to make the optical excitation pulse compatible with the entanglement protocol. In this section, two filter types are used; a *Volume Bragg Grating* (VBG) and a custom made *Pulse stretcher*. The working principles of both devices are presented in Appendix C.3 and C.4, respectively.
The aim of this section is thus to consider the effects of these frequency filters in regards to the optical excitation of the low-energy transition, having a resonance frequency at $\nu_0 = 317.23$ THz (945.03 nm), see Table 2.1.

5.1.1 Resonant Excitation of the Positive Trion

In order to investigate the performance of the optical excitation, one must consider its ability to excite the correct transition. For the positive trion, the two vertical transitions

are of interest, namely (i) the low-energy transition $|\Uparrow\rangle \rightarrow |\Uparrow\Downarrow,\uparrow\rangle$ and (ii) the high-energy transition $|\Downarrow\rangle \rightarrow |\Uparrow\Downarrow,\downarrow\rangle$ (see Fig. 2.7). The excitation of the former is utilized in the entanglement protocol, however, dependent on the laser bandwidth the opposite transition might be accessed as well. Consequently, the performance of the excitation pulse can be probed by preparing either $|\Uparrow\rangle$ or $|\Downarrow\rangle$ through OSP (recall Fig. 2.7) and subsequently excite the low-energy transition. In the ideal case, no emission is expected if the initial spin-state was prepared in $|\Downarrow\rangle$. The performance is thus quantified by the *rejection ratio* R_r, i.e. the ratio between the emission coming from either of the two ground-states upon excitation.
The excitation scheme probing the rejection ratio can therefore be summarized to: (i) Prepare the X^+ using the ABB-laser, (ii) Initialize *either* $|\Uparrow\rangle$ *or* $|\Downarrow\rangle$ through OSP, (iii) excite the low-energy transition using the pulsed Mira-laser.

Experimentally, this is realised by fine-tuning the bias-voltage across the QD to match that of the low-energy transition, conditioned on the central wavelength determined by either the pulse stretcher or VBG. For the positive trion, this means a central wavelength around 945 nm (recall Section 2.1.1), which is measured using a spectrometer, yielding the central wavelength and its bandwidth. However, one most correct for the response of the spectrometer (the minimum resolution), to be sure the spectrometer itself is not the limiting factor. The response of spectrometer is characterized using a monochromatic-laser tuned to 945 nm, given a FWHM of 8.25 ± 0.12 GHz. The latter is included in the data presented in this section, that is, the bandwidths are extracted from the convolution between the Mira-pulses and the response function of the spectrometer - both having a Gaussian shape.

The Pulse Stretcher

In contrast to the VBG, the central wavelength *and* the bandwidth can be modified using the pulse stretcher (see Appendix C.4 for more information).
To analyse its effects in regards to the optical excitation, a total of eight different pulses are employed, defined by their bandwidth and central wavelength. The latter should ideally remain the same for all settings, but in practice this will vary slightly.
The effect of the pulse stretcher is best described by Fig. 5.1 (a), showing the photon counts as a function of the excitation power[1]. The solid (dashed) lines corresponds to the spin-state being prepared in $|\Uparrow\rangle$ ($|\Downarrow\rangle$) by OSP, while the coloring presents four different settings. The corresponding R_r is presented in Fig. 5.1 (b), from which it can be observed that the rejection ratio increases as the spectral bandwidth decreased. This correlation can be explained by the finite splitting of the ground states $\Delta_h = 7.29$ GHz (see Table 2.1) whereby the correct transition can be addressed with a higher degree of precision, owing to the narrowing bandwidth.
This effect becomes more clear in Fig. 5.1 (c), showing the correlation between the bandwidth and the rejection ratio, along with the maximum counts for each setting. Here, the maximum(minimum) rejection ratio yields $R_r = 23.9(2.5)$ at a bandwidth of 9.3(29.4) GHz. However, as the bandwidth becomes more narrow, the more light is lost in the pulse stretcher, resulting in a drop of the maximum photon count. For instance, consider the red curve in Fig. 5.1 (a), having a bandwidth of 27.7 pm (9.3 GHz). The maximum power

[1]The actual excitation power is much lower - this merely serves as a reference, measuring parts of the excitation pulse using a Powermeter.

achievable lies around 0.08 μW, and hence limited by the losses and inefficiencies of the pulse stretcher setup[2]. This is an issue, since the narrow-band pulses cannot reach a full π-pulse, which in this context results in the saturation of the photon counts presented in Fig. 5.1 (a), where only the black and green curves reach a maximum.
In other words, the pulse stretcher provides a method to examine the correlation between the spectral bandwidth and the rejection ratio. However, due to its inefficiency a VBG with a fixed bandwidth is used instead.

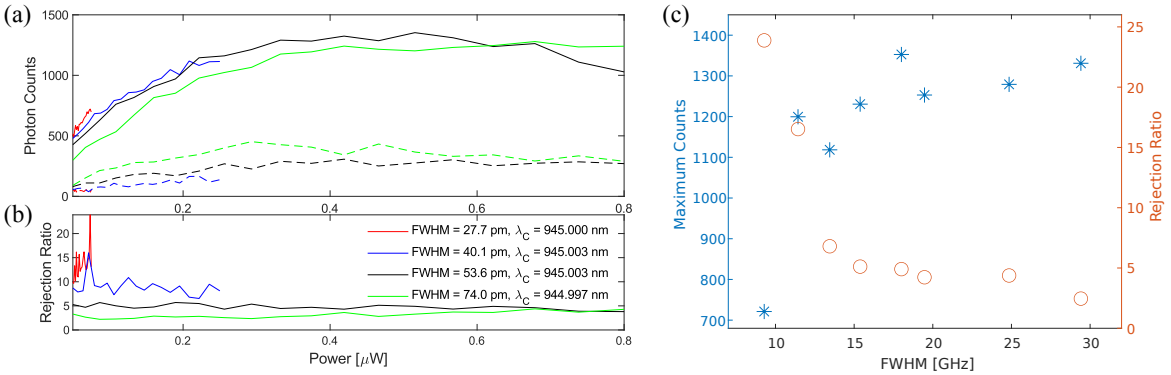

Figure 5.1: (a) Photon counts as a function of excitation power for a spin-state prepared in $|\Uparrow\rangle$ (solid-line) and $|\Downarrow\rangle$ (dashed-line). (b) The corresponding rejection ratios at various excitation powers. (c) Correlation between the rejection ratio and the FWHM of the excitation pulse at the position where the power yields the maximum photon counts.

The Volume Bragg Grating

The VBG is a diffraction grating which filters a given frequency from a broad spectrum. This device has a fixed bandwidth, which according to the manufacture OptiGrate, has a FWHM of 30 pm at a central wavelength of 956.039 nm (i.e. the "optimal" wavelength). Nevertheless, as stated in Appendix C.3, the central wavelength of the diffracted light can be controlled by altering the angle of incidence.
In this work, the angle of incidence yields a central wavelength of $\lambda_C = 945.03$ nm with a FWHM = 38.9 pm (13.1 GHz). The corresponding photon counts as a function of the excitation power is presented in Fig. 5.2 (a). The black(blue) lines represents measurements using the long(short) path of the excitation interferometer to excite the QD. The dashed black vertical lines mark an area where the photon counts saturates, corresponding to an optical π-pulse. This interval ranges from 0.3 - 0.45 μW, giving an average rejection ratio of $R_r = 15.2 \pm 3.1$ (15.3 ± 4.9) for the long path (short path).
Increasing the excitation power even further, drives the population between the ground state and the excited state of the two-level system, yielding the Rabi-oscillations shown in Fig. 5.2 (b). If the laser frequency is at resonance, the probability of populating the excited state oscillates as

$$P_e(t) = \sin(\Omega_R t/2)^2, \tag{5.1.1}$$

[2]It was found that up to 98 % of the incident light was lost by the pulse stretcher setup, making it impossible to achieve enough power with Mira-laser.

where Ω_R is the Rabi-frequency [45]. The fitted curve in Fig. 5.2 (b) corresponds to Eq. 5.1.1, showing a clear oscillation in the photon counts as a function of the excitation power. Thus, a π-pulse can be realised for excitation-powers at ≈ 0.3 μW with a weighted average rejection ratio of $R_r = 15.2 \pm 2.6$.

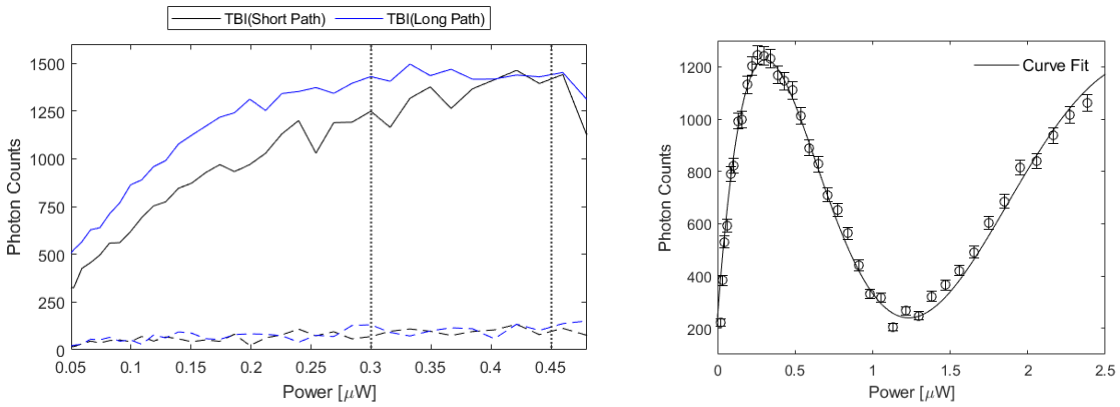

(a) Photon Counts and Rejection Ratios.

(b) Rabi Oscillation.

Figure 5.2: (a) Photon counts as a function of excitation power for a spin-state prepared in $|\Uparrow\rangle$ (solid-line) and $|\Downarrow\rangle$ (dashed-line). The two vertical lines mark the interval, whereby the average rejection ratio of both interferometer paths gives $R_r = 15.2 \pm 2.6$. (b) Rabi-oscillations as a function of the excitation power. The fitted curved is given by Eq. 5.1.1, presenting the population of the excited state in a two-level system.

Bandwidth and Pulse Duration

Varying the spectral bandwidth alters the duration of the excitation pulse as these are inversely proportional to one another. Assuming a Gaussian pulse shape, the relation between the FWHM of the spectral bandwidth $\Delta\lambda$ and the corresponding pulse duration $\Delta\mathcal{T}$, is given by

$$\Delta\mathcal{T} = \frac{\lambda_C^2 \cdot \mathcal{G}}{\Delta\lambda \cdot c}, \tag{5.1.2}$$

where λ_C denotes the central wavelength, $\mathcal{G} = 0.441$ is the time-bandwidth product for a Gaussian pulse and c is the speed of light in vacuum. Inserting the values determined by the VBG, yields a pulse duration of $\Delta\mathcal{T} = 33.8$ ps.

From Ref. [11], the radiative decay rate of the X^+ is $\gamma_0^{(+)} = (3.07 \pm 0.06)$ ns^{-1} (see Table 2.1). The corresponding lifetime $\tau_0^{(+)}$ is therefore

$$\tau_0^{(+)} = \frac{1}{\gamma_0^{(+)}} = 326 \pm 6 \text{ ps}, \tag{5.1.3}$$

i.e. an order of magnitude larger than the pulse duration. Ideally, $\Delta\mathcal{T} \ll \tau_0^{(+)}$ to avoid re-excitation errors induced by a long excitation pulse. Consequently, there is a constant trade-off between a large rejection ratio and a small probability of re-excitation. The latter could potentially result in two photons being emitted from the same excitation pulse and hence affect the purity of single-photon source.

5.2 Single-Photon Purity

A two-level quantum system should ideally emit single photons if resonantly excited. The quality of the single-photon emitter can hence be determined by looking at the photon statistics, i.e. examining the correlations between a continuous stream of photons generated by the single-photon source. Experimentally, this is realized through the use of a beam-splitter, dividing the light into two separate detectors $\{D_1, D_2\}$, each recording the arrival time of the photon events. Comparing events occurring at times t in one detector and $t+\tau$ in the opposite detector, allows one to evaluate the normalized second-order correlation function defined by

$$g^{(2)}(t,\tau) = \frac{\langle \hat{a}^\dagger(t)\hat{a}^\dagger(t+\tau)\hat{a}(t+\tau)\hat{a}(t)\rangle}{\langle \hat{a}^\dagger(t)\hat{a}(t)\rangle^2}, \tag{5.2.1}$$

where $\hat{a}^\dagger(\hat{a})$ is the creation(annihilation) operator of the optical mode [5]. Especially the case where the time-delay is zero, i.e. $\tau = 0$, is of great interest. For *Fock*-states (or number-states) the second-order correlation function takes the form

$$g_F^{(2)}(\tau = 0) = 1 - 1/n, \qquad \text{for } n \geq 1, \tag{5.2.2}$$

where n is the photon number. Hence, the ideal single-photon source yields $g_F^{(2)}(\tau = 0) = 0$, which is outside the classical bound of $g^{(2)}(\tau = 0) \geq 1$, and therefore a non-classical phenomenon [45]. In addition to this, a *Coherent*-state gives $g^{(2)}(\tau = 0) = 1$, while a single mode *Thermal*-state reads $g^{(2)}(\tau = 0) = 2$. Thus, determining the second-order correlation function yields a technique of quantifying the photon statistics and hence estimate the single-photon purity along with a method of distinguishing various quantum states.

5.2.1 Experimental Analysis of Single-Photon Purity

The single-photon purity can be assessed by the use of a Hanbury Brown and Twiss (HBT)-like setup [46], measuring the correlation between two separate detectors, each placed at the output port of a 50/50 beam-splitter. Fortunately, the TBI meets these requirements whereby a HBT-measurement readily can be implemented without any further alterations to the existing setup. Ideally, the early and late time-bins created by the detection interferometer (recall Fig. 4.4), contains single-photon events whereas events caused by two-photon interference makes up the middle time-bin. Consequently, operating the detection interferometer under passive switching allows one to perform correlations measurements in both the early and late time-bins separately, while simultaneously conduct a HOM-measurement on the middle time-bin. The latter will be introduced in Section 5.3.
Once more, the Time Tagger from Swabian Instruments [43] is employed to keep track of the time-bins. This device records the timetags of each event triggered by the Superconducting nanowire single-photon detectors (SNSPDs), enabling high precision time-resolution at the order of pico-seconds. A continuous stream of photons are generated by the resonant excitation of the pulsed Mira-laser, from which a histogram of the coincidence counts between the two detectors can be constructed, one for each time-bin. However, only the early and late time-bins are of interest in this analysis. The normalized second-order correlation function can thus be obtained from the correlations at times $\tau = 0$ and $\tau \to \infty$, where the latter provides a means of normalization, i.e. all information in regards to the first event is gone.

For this analysis two different excitation schemes are implemented; (i) the "Non-Entanglement sequence" and (ii) the "Entanglement sequence", see Fig. 5.3 (a). The difference lies in the preparation of the spin-state utilizing the principles of OSP (recall Section 2.3.1). The former pumps the high-energy transition $|\Downarrow\rangle \rightarrow |\Uparrow\Downarrow, \downarrow\rangle$ shelving the hole-spin in $|\Uparrow\rangle$ directly (see Fig. 5.3 (b)), while the latter drives the low-energy transition $|\Uparrow\rangle \rightarrow |\Uparrow\Downarrow, \uparrow\rangle$ shelving the hole-spin in $|\Downarrow\rangle$, following by a π-rotation of the hole-spin, i.e. rotating into $|\Uparrow\rangle$. The outcome is the same, however it is two different techniques, whereby the influence of the spin-rotation may be examined in regards to the single-photon purity. Since spin-rotations constitutes an essential part of the entanglement protocol, the "Entanglement sequence" resembles that of the protocol - hence its name. Common for both schemes are the initialization of X^+ at the beginning of each sequence using an ABB-laser for 100 ns and the optical excitation of the low-energy transition by the Mira-pulses generated in the TBI. Moreover, each scheme is repeated every $T_{rep} = 606$ ns over a duration of several minutes[3], whereby the coincidence counts for the early and late time-bin are found by analysing the entire stream of photons as described in Section 5.2.

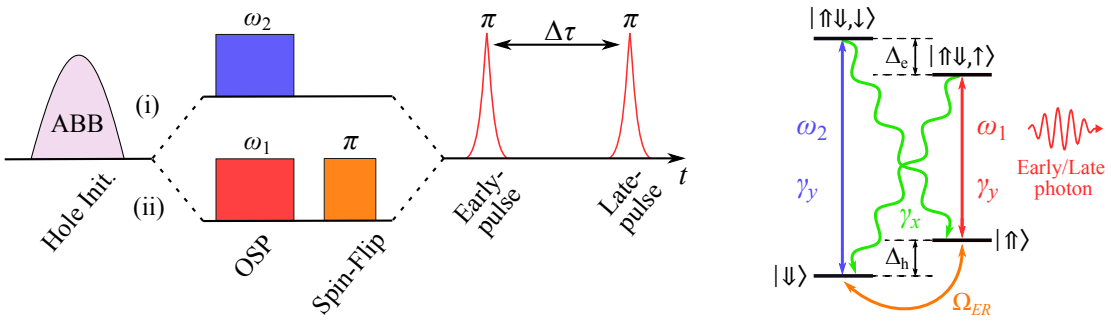

(a) Two pulse sequences preparing $|\Uparrow\rangle$.

(b) Energy diagram of X^+.

Figure 5.3: (a) Two different pulse sequences used for the characterization of the single-photon source. Sequence (i) pumps the high-energy transition, initializing the hole-spin directly into $|\Uparrow\rangle$, while (ii) pumps the low-energy transition and applies an additional spin-rotation. (b) Energy diagram of X^+, showing the various optical transitions and rotations.

Each time-bin is associated with a given integration window, i.e. a time-interval that defines its length and position. These are presented in Fig. 5.4 (a), showing a histogram of the total counts in each time-bin for the non-entanglement sequence, where the vertical red line marks the beginning of the integration window while the black lines show various integration-lengths, i.e. ranging from 0.5 to 3 ns. For comparison, the middle time-bin is included as well.
It turns out that $g^{(2)}(\tau = 0)$ is quite sensitive to the integration window, which is clearly visible in Fig. 5.4 (b), where sequence (i) (sequence (ii)) is shown as the blue (red) graphs, while the early (late) time-bin are presented as dashed (solid) lines. Here it can be observed,

[3]The repetition time T_{rep} is fixed to 606 ns, corresponding to the duration of one repetition in the entanglement protocol presented in Section 3.3. The repetition time has been found experimentally and it includes the duration of the ABB-laser, OSP, spin-rotations and optical excitation.

that the (ii) sequence yields a generally larger $g^{(2)}(\tau = 0)$, especially at the narrow (0.5 ns) and wide (3 ns) integration window. The latter could be explained by the integration window exceeding the pulse area (see Fig. 5.4 (a)) whereby the signal-to-noise ratio (SNR) decreases in the presence of any potential noise, e.g. laser scattering. This will be examined more closely in the following paragraph discussing impurities caused by laser background and the resulting affect on the single-photon purity.

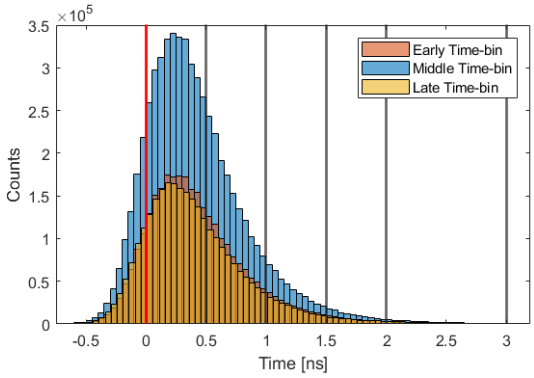

(a) Histogram showing the distribution of the three time-bins.

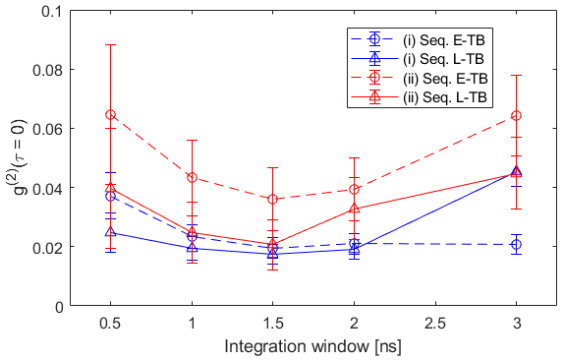

(b) $g^{(2)}(\tau = 0)$ at varying integration windows.

Figure 5.4: (a) Histogram showing the three time-bins and corresponding integration windows. The red line marks the beginning, while the black lines indicate the end of each window. (b) $g^{(2)}(0)$ dependence for the two pulse sequences at varying integration lengths.

The data presented in 5.4 (b) is found by analysing the two-photon correlation histogram, employing the Swabian Time Tagger. An example is shown in Fig. 5.5 (a) for sequence (i), using an integration window of 1.5 ns, which accounts for 85% of the entire counts in each time-bin. The small peak at $T_{rep} = 0$, see Fig. 5.5 (b), presents the coincidence counts at $\tau = 0$, while Fig. 5.5 (c) shows the coincidences at $T_{rep} = 1$.

Taking the ratio of the coincidence counts at $T_{rep} = 0$ and $T_{rep} \to \infty$ yields the single-photon purity[4]. Thus, given an integrating window of 1.5 ns, the normalized second-order correlation at $\tau = 0$ reads

$$\text{(i) Sequence:} \quad g_e^{(2)}(0) = 0.0196 \pm 0.0034, \quad g_l^{(2)}(0) = 0.0175 \pm 0.0033, \tag{5.2.3}$$

$$\text{(ii) Sequence:} \quad g_e^{(2)}(0) = 0.0361 \pm 0.0106, \quad g_l^{(2)}(0) = 0.0206 \pm 0.0085, \tag{5.2.4}$$

where the uncertainties are estimated using error-propagation assuming Poisson-distributed noise, i.e. $\sigma = \sqrt{N}$, where N is to total counts for each time-bin. In regards to Fig. 5.4 (b), this yields the best single-photon purity for both time-bins and sequences. The values obtained in the non-entanglement sequence are comparable with previous work by Uppu *et al.* [47], demonstrating a single-photon purity of $g^{(2)} = 0.015 \pm 0.005$ using a QD embedded in a PCW. Furthermore, the coincidence counts in the late time-bin is on average 7.7 % lower than the early time-bin and hence comparable with the finite cyclicity of the X^+, which in theory should give a reduction of approximately 7 %.

[4]In this analysis, $T_{rep} \to \infty$ corresponds to coincidence counts further than $30 \cdot T_{rep} \approx 18.18$ μs away.

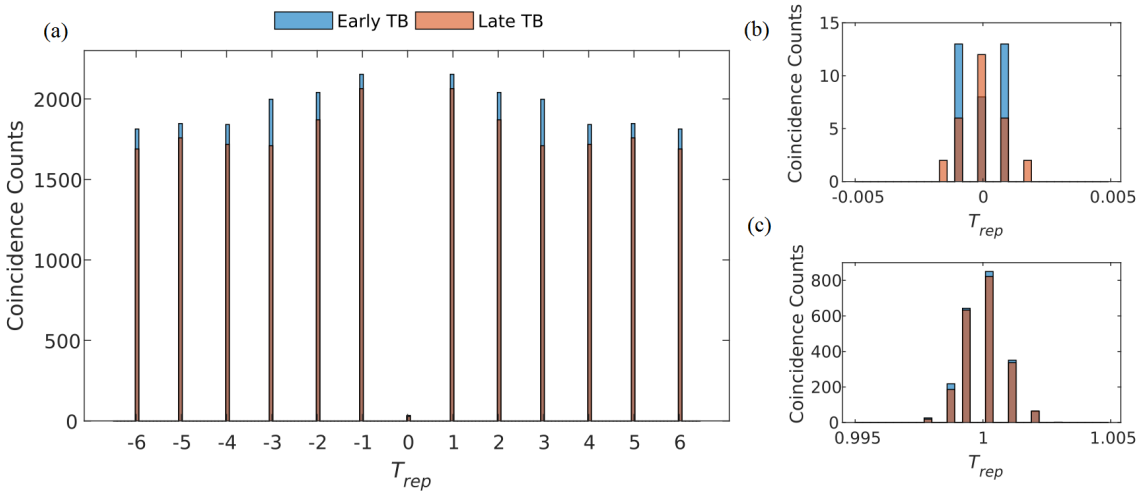

Figure 5.5: (a) Two-photon coincidence counts in the early and late time-bin (TB) for the (i) sequence with an integration window of 1.5 ns. (b) A histogram with a greater time-resolution, showing the coincidence counts around $T_{rep} = 0$ and (c) $T_{rep} = 1$. The plotting range of (b) and (c) corresponds to 6.06 ns.

Impurity

Altering the bias voltage allows one to tune the QD in and out of resonance (see Section 2.1.1). Consequently, performing an experiment where the QD is off-resonance with the excitation laser, i.e. the Mira-pulses, provides a method to investigate the background scattering into the waveguide-mode. Naturally, the latter should be at a minimum for an ideal system containing a single-photon source. Thus, the *impurity* quantifies the ratio between the single-photon counts in the resonant and non-resonant case

$$\mathcal{I} \equiv \frac{\sum C_{nres}}{\sum C_{res} - \sum C_{nres}}, \tag{5.2.5}$$

where $(\sum C_{nres})$ $\sum C_{res}$ is the total counts for (non)-resonant excitation. The impurity of the previous measurements is presented in Fig. 5.6, where the total counts in each time-bin was found for both the resonant and non-resonant case. On average, the entanglement sequence yields a slightly larger impurity compared to the non-entanglement sequence

$$\mathcal{I}_{\text{(i)}} = 0.0025 \pm 0.0004, \qquad \mathcal{I}_{\text{(ii)}} = 0.0037 \pm 0.0006, \tag{5.2.6}$$

which could be a contributing factor to the $g^{(2)}$-analysis.
Following Kako *et al.* [48], the single-photon purity can be related to the impurity by

$$g^{(2)}(\tau = 0) \approx 2\mathcal{I} - \mathcal{I}^2, \tag{5.2.7}$$

under the assumption of a statistical mixture between the single-photon source and a small contribution from the background, following poissonian statistics. Inserting the impurities found in Eq. 5.2.6 into this relation, provides a method to investigate its affect on the single-photon purity in each sequence

$$g^{(2)}_{\text{(i)}}(\tau = 0) \approx 0.0050 \pm 0.0008, \qquad g^{(2)}_{\text{(ii)}}(\tau = 0) \approx 0.0074 \pm 0.0012. \tag{5.2.8}$$

Thus, comparing these values to the single-photon purities obtained in Eqs. 5.2.3 - 5.2.4, the contribution from the impurity is generally more predominant in the entanglement sequence, which may originate from the additional π-rotation of the ground states. However, based on this analysis, the impurity is *not* the limiting factor, whereby one cannot eliminate other parameters like re-excitation errors caused by the optical excitation pulses.

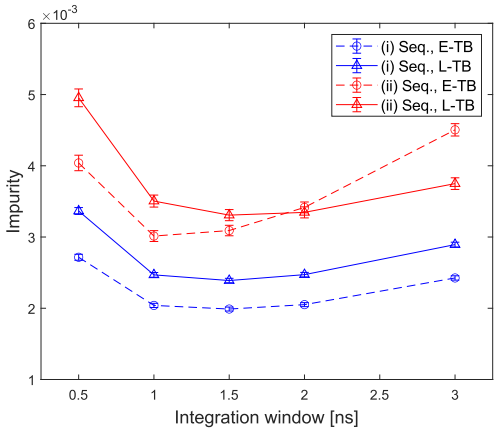

Figure 5.6: Impurity as a function of the integration window. The impurity of the entanglement (non-entanglement) sequence is shown by the red(blue) lines.

Blinking

Photon-bunching at long timescales (100 ns or longer) can be assigned to a phenomenon known as *blinking*[5]. This process affects the emission of QD resulting in a bunching effect that can be observed in the $g^{(2)}$-analysis, where an increase in the two-photon coincidence counts (CC) is visible around both sides at $T_{rep} = 0$. This effect is clearly illustrated in Fig. 5.7 (a), presenting the histogram from the previous measurement with larger timescales.

Fitting an exponential function to the normalized CC, i.e. normalized to the average CC obtained further than $30 \cdot T_{rep}$ away, yields the timescale of the blinking process τ_B, see Fig. 5.7 (b). Thus, taking the average value obtained from both time-bins give

$$\bar{\tau}_B = (0.36 \pm 0.02)\ T_{rep} = 218 \pm 14 \text{ ns}, \tag{5.2.9}$$

which demonstrates the need to normalize $g^{(2)}(\tau = 0)$ at $\tau \to \infty$ in order to determine the single-photon purity correctly.

[5]Blinking may arise from uncontrolled spin-flips processes or tunneling of carriers [5].

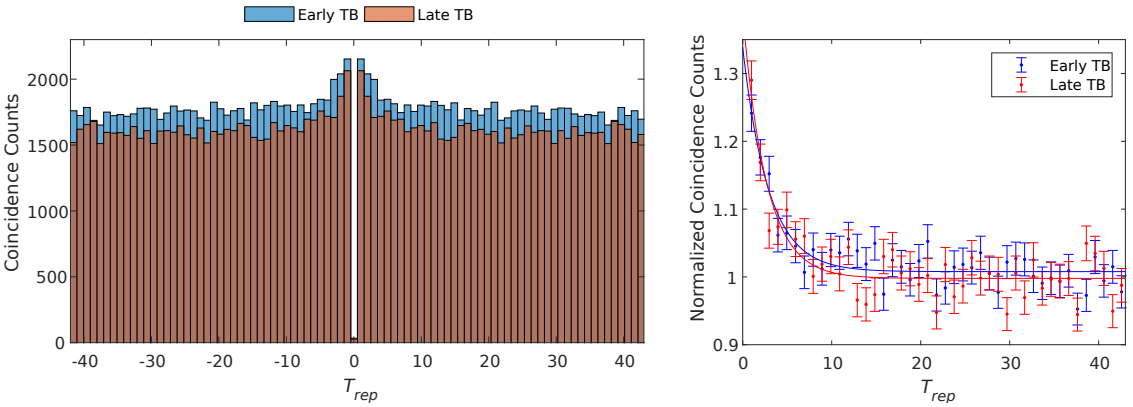

(a) Histogram of coincidence counts at longer timescales.

(b) Exponential fit for $\tau > 0$.

Figure 5.7: (a) Two-photon CC in the early and late time-bin (TB) for the (i) sequence with an integration window of 1.5 ns. The time scaling is widened to display the effects of blinking. (b) Exponential fit to the normalized CC, whereby the normalization factor is calculated by the average CC over 30 repetitions away from $\tau = 0$.

5.3 Photon Indistinguishability

Highly indistinguishable photons are fundamental for most applications in quantum information processing and is therefore an essential figure of merit for an ideal single-photon source. The degree of indistinguishably can be quantified by measuring the Hong-Ou-Mandel (HOM) interference [49], i.e. extracting the visibility from two photons interfering at a BS. Thus, reviewing the transformation of the latter in context of two incident photons is a good starting point towards the characterization of indistinguishability.

Following the notation presented in Section 4.1.2, the quantum-mechanical input-output relation of a BS reads

$$\begin{bmatrix} \hat{a}_3 \\ \hat{a}_4 \end{bmatrix} = \begin{pmatrix} t & r'e^{i\xi_2} \\ re^{i\xi_1} & t' \end{pmatrix} \begin{bmatrix} \hat{a}_1 \\ \hat{a}_2 \end{bmatrix}, \tag{5.3.1}$$

where $\hat{a}_{\{1,2\}}(\hat{a}_{\{3,4\}})$ are the two input(output) modes. The annihilation/creation operators obey the commutation relations, given by

$$[\hat{a}_i, \hat{a}_j] = \left[\hat{a}_i^\dagger, \hat{a}_j^\dagger\right] = 0, \qquad \left[\hat{a}_i, \hat{a}_j^\dagger\right] = \delta_{ij}, \tag{5.3.2}$$

where δ_{ij} is the Kronecker delta function. For a lossless 50/50 BS, the "inverse" relations involving the creation operators takes the form

$$\hat{a}_1^\dagger = \frac{1}{\sqrt{2}}\left(\hat{a}_3^\dagger + i\hat{a}_4^\dagger\right), \qquad \hat{a}_2^\dagger = \frac{1}{\sqrt{2}}\left(i\hat{a}_3^\dagger + \hat{a}_4^\dagger\right), \qquad \xi_{\{1,2\}} = \pi/2, \tag{5.3.3}$$

where the creation operator transforms a Fock-state according to $\hat{a}^\dagger |n\rangle = \sqrt{n+1}\,|n+1\rangle$. The output of two identical photons arriving simultaneously at each input port of the BS is hence given by

$$|1\rangle_1 |1\rangle_2 = \hat{a}_1^\dagger \hat{a}_2^\dagger |\emptyset\rangle_1 |\emptyset\rangle_2 \xrightarrow{BS} \frac{1}{2}\left(\hat{a}_3^\dagger + i\hat{a}_4^\dagger\right)\left(i\hat{a}_3^\dagger + \hat{a}_4^\dagger\right)|\emptyset\rangle_{3,4} \tag{5.3.4}$$

$$= \frac{i}{2}\left(\hat{a}_3^\dagger \hat{a}_3^\dagger + \hat{a}_4^\dagger \hat{a}_4^\dagger\right)|\emptyset\rangle_{3,4} \tag{5.3.5}$$

$$= \frac{i}{\sqrt{2}}\left(|2\rangle_3 |\emptyset\rangle_4 + |\emptyset\rangle_3 |2\rangle_4\right). \tag{5.3.6}$$

Consequently, both photons merge together into the *same* output port and thus arrive in pairs - a phenomenon known as *photon-bunching*. This effect is only visible if the photons are identical or *indistinguishable*, i.e. having the same polarization, frequency and temporal(spatial) mode. Should the two photons be distinguishable, e.g in terms of polarization, there are an additional two transformations which may occur, namely the cases where both photons are transmitted or reflected. As a direct consequence, one may probe the degree of indistinguishability by examining the coincidence counts between two detectors for a continuous steam of photons; truly indistinguishable photons will not trigger any coincidences, while distinguishable photons lead to coincidences between the detectors.

5.3.1 Experimental Analysis of Photon Indistinguishability

Experimentally, there are several configurations allowing one to examine the two-photon interference. In most cases however, the basic principle can be described by a balanced Mach-Zehnder Interferometer, i.e. a BS converting a single input into two paths with equal lengths, which are interfered at a second BS followed by two detectors at each output. Thus, the photon indistinguishability can be measured by examining the middle time-bin created by the TBI, as this provides a means of investigating the two-photon interference. The data presented in this section is hence extracted from the same measurements as presented in Section 5.2.1, due to the properties of passive switching, though the analysis is slightly different.

The level of indistinguishability is quantified by the HOM visibility, which usually is defined by the ratio between the minimum and maximum coincidence counts [50]

$$\mathcal{V}_{\text{HOM}} = 1 - \frac{C_{min}}{C_{max}}, \qquad 0 \leq V \leq 1, \tag{5.3.7}$$

at varying arrival-times for one of the two photons interfering at the BS. However, as the arrival time of the photons in the TBI is fixed, i.e. the length of either the short or long interferometer path cannot be changed, an alternative approach is required.
Letting $\sum C^{(m)}(\tau = 0)$ denote the total sum of coincidence counts in the middle time-bin at $\tau = 0$, the visibility for the TBI is found by

$$\mathcal{V}_{\text{HOM}} = 1 - \frac{\sum C^{(m)}(\tau = 0)}{\sum \bar{C}^{(el)}(\tau = \pm\Delta\tau)}, \tag{5.3.8}$$

where $\Delta\tau \approx 11.83$ ns is given by the spatial difference of the short and long interferometer path while the denominator is defined as

$$\sum \bar{C}^{(el)}(\tau = \pm\Delta\tau) \equiv \frac{\sum C^{(e)}(\tau = -\Delta\tau) + \sum C^{(l)}(\tau = +\Delta\tau)}{2}, \tag{5.3.9}$$

i.e. the average coincidence counts for the early and late time-bins at $\tau = \pm\Delta\tau$.
Intuitively, this can be understood by considering Fig. 5.8, showing the photon-emission from two subsequent excitations created from two pulse-sequences separated by T_{rep}. The early(late) photon $e_i(l_i)$ comes from the optical excitation of the early(late) pulse generated by the excitation interferometer.

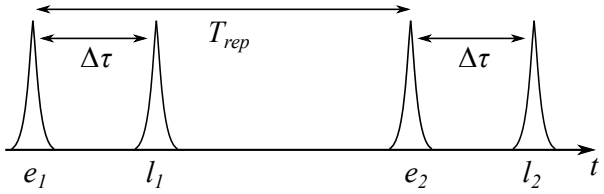

Figure 5.8: Stream of photons going to the detection interferometer. Here $e_i(l_i)$ denotes the early(late) photons created from the optical excitation of the ith excitation pulse. The repetition time of the excitation pulse is T_{rep}, while e_i and l_i are separated by $\Delta\tau$.

Going through the detection interferometer, the photons can take either the (S)hort or (L)ong path, e.g. (e_1, S) denotes the early photon from the first pulse taking the short path of the detection interferometer. Thus, the following coincidences between Detector 1 and Detector 2 are (ideally) possible, each having the same probability using passive switching:

- Coincidence at $\tau = 0$:

$$|m\rangle : \underbrace{\{\overbrace{(e_1, L)}^{\text{1. Event}}, \overbrace{(l_1, S)}^{\text{2. Event}}\}}_{\text{Coincidence pair}} + \underbrace{\{\overbrace{(e_2, L)}^{\text{1. Event}}, \overbrace{(l_2, S)}^{\text{2. Event}}\}}_{\text{Coincidence pair}}, \tag{5.3.10}$$

  which only occurs if the photons *are* distinguishable. Otherwise, photon-pair goes to the *same* detector.

- Coincidence at $\tau = \pm\Delta\tau$:

$$|e\rangle : \{(e_1, S),\ (l_1, S)\} + \{(e_2, S),\ (l_2, S)\}, \tag{5.3.11}$$
$$|l\rangle : \{(e_1, L),\ (l_1, L)\} + \{(e_2, L),\ (l_2, L)\}, \tag{5.3.12}$$

  where the early(late) time-bin $|e\rangle$ ($|l\rangle$) results in coincidence at $\tau = -\Delta\tau(+\Delta\tau)$. These coincidences do not rely on two-photon interference as they are temporally separated. Thus, the indistinguishability of photons interfered in the middle time-bin can be extracted using these time-bins as reference (or normalization).

As a result of the possible combinations of coincidence pairs, the HOM visibility can be found using Eq. 5.3.8, as it yields the ratio between the coincidences in the middle time-bin and the two adjacent time-bins. Note, the sum of coincidence pairs in the early and late time-bin gives twice the combinations compared to the middle time-bin, hence the factor of two in the denominator of Eq. 5.3.9.

The two-photon correlation histogram between the middle time-bin and the stream of photons is shown in Fig. 5.9 (a). In contrast to the previous analysis of the single-photon

purity presented in Section 5.2.1, this analysis is conditioned on a two-fold coincidence between the middle time-bin and *any* other event prior or posterior to the latter. As a direct consequence, coincidences at $\tau = \pm\Delta\tau$ are accessible, which is shown in Fig. 5.9 (b).

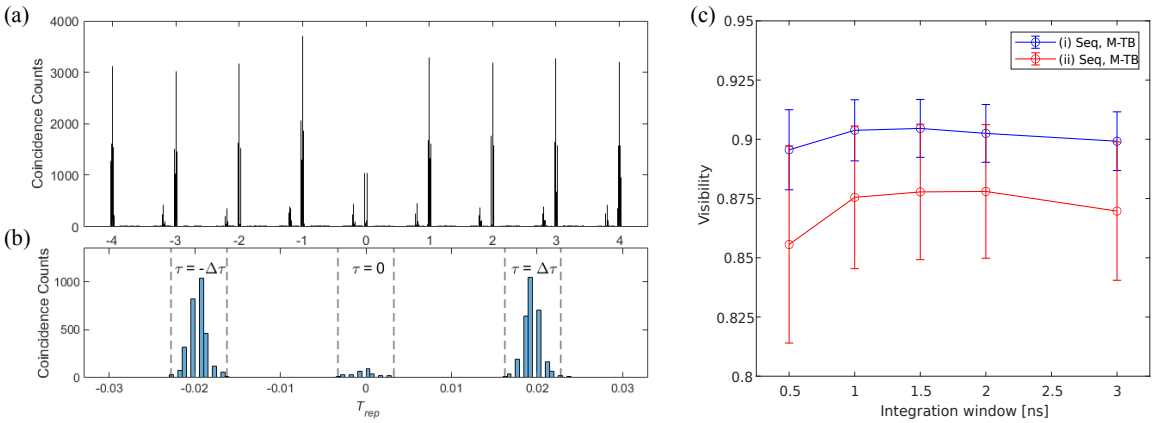

Figure 5.9: (a) Two-photon coincidence counts between the middle time-bin (defined by an integration window of 1.5 ns) and the stream of photons for the (i) sequence. (b) A histogram with a greater time-resolution, showing the coincidence counts around $T_{rep} = 0$ for the early, middle and late time-bin, respectively. Each time-bin is marked by the vertical dashed lines. (c) The HOM visibility for both sequences as a function of the integration window of the middle time-bin.

Following Eq. 5.3.8, the total coincidence counts for each time-bin around $T_{rep} = 0$ are extracted, whereby the corresponding visibility for the two sequences, given an integration window of 1.5 ns, reads

$$\text{(i) Sequence:} \quad \mathcal{V}_{\text{HOM}} = 0.9046 \pm 0.0122, \tag{5.3.13}$$

$$\text{(ii) Sequence:} \quad \mathcal{V}_{\text{HOM}} = 0.8778 \pm 0.0286, \tag{5.3.14}$$

while the HOM visibility for varying integration windows are presented in Fig. 5.9 (c). As were the case for the analysis of the single-photon purity, the highest visibility appears at 1.5 ns, while the narrow and large integration windows yield a lower visibility.
So far, the analysis is based on the ideal case, where all coincidence pairs at $\tau = 0$ are events of the type presented in Eq. 5.3.10. However, if two photons were to come from the same excitation, one would not be able to distinguish between these coincidence events and actual two-photon interferences. In other words, the single-photon purity affects the visibility - an imperfection which one can rectify if the purity is determined.

Intrinsic Indistinguishability

The degree of indistinguishability defined by Eq. 5.3.8, provides a basic, yet slightly incomplete estimate of the visibility, as limitations and imperfections of the experimental setup are not taken into account. Following Santori *et al.* [51], the HOM visibility is affected by a total of three parameters

(i) The reflection (R) and transmission (T) coefficients of the BS (and PBS),

(ii) The classical interference fringe contrast $V_C \equiv (1-\epsilon)$,

(iii) The purity of the single-photon source $g^{(2)}(\tau = 0)$.

The latter was quantified in Section 5.2 (Eqs. 5.2.3 - 5.2.4), providing an estimate on the single-photon purity using both the early and late time-bin. The second parameter can be extracted from Section 4.3.2, yielding a lower bound on the classical visibility by $V_C = (1-\epsilon) = 0.995 \pm 0.001$ (from Eq. 4.3.41). Finally, the performance of BS used in this particular setup was characterized, demonstrating a reflection(transmission) coefficient of $R = 0.513$ ($T = 1 - R = 0.487$). In contrast to Ref. [51], the splitting ratio of PBS_2 has to be considered as well. However, under passive switching the PBS acts as a 50/50 BS, where the splitting ratio is mainly dominated by the loss in the long interferometer path. Thus, one can approximate the reflection(transmission) coefficient of the PBS to $R_P = 0.485$ ($T_P = 0.515$), assuming a loss of 6 %.
Based on these parameters, the *intrinsic* or *corrected* visibility can be derived, removing any imperfections introduced by the experimental setup.

Following Ref. [51], the sum of all coincidence counts in the middle time-bin at $\tau = 0$ is proportional to

$$\sum C^m(\tau = 0) \propto \left[(R_P T_P R^2 + R_P T_P T^2)(1+2g) - 2(1-\epsilon)^2 R_P T_P R T \mathcal{V}\right], \tag{5.3.15}$$

while the corresponding coincidence counts in the early and late time-bin takes the form

$$\sum C^e(\tau = -\Delta\tau) \propto \left[T_P^2 T R(1+2g) + R_P^2 R T\right], \tag{5.3.16}$$

$$\sum C^l(\tau = +\Delta\tau) \propto \left[T_P^2 T R + R_P^2 R T(1+2g)\right], \tag{5.3.17}$$

all having the same factor of proportionality. Based on Eq. 5.3.9, the average coincidence counts in the early and late time-bin is thus

$$\sum \bar{C}^{(el)}(\tau = \pm\Delta\tau) \propto RT(R_P^2 + T_P^2)(g+1), \tag{5.3.18}$$

whereby the influence of the parameters (i)-(iii) can be determined using Eq. 5.3.8, under the assumption of a perfect visibility (i.e. $\mathcal{V} = 1$)

$$\mathcal{V}_{\mathrm{HOM}}^P = 1 - \frac{\sum C^{(m)}(\tau = 0, \mathcal{V} = 1)}{\sum \bar{C}^{(el)}(\tau = \pm\Delta\tau)} \tag{5.3.19}$$

$$= 1 - \frac{R_P T_P \left[(2g+1)(R^2+T^2) - 2RT(1-\epsilon)^2\right]}{RT(R_P^2 + T_P^2)(g+1)}. \tag{5.3.20}$$

In the case of an ideal system, i.e. $R_P = T_P = R = T = 1/2$, $\epsilon = 0$ and $g = 0$, no corrections are required, which means that $\mathcal{V}_{\mathrm{HOM}}^P = 1$. However, imperfections caused by any of the three parameters listed above, affects the measurements characterizing the actual indistinguishability of the emitted photons, making $\mathcal{V}_{\mathrm{HOM}}^P < 1$. For this particular setup, the dominant factor is the single-photon purity, which becomes clear from Table 5.1, showing the impact of each individual parameter.

Corrections to the Visibility	Impact on $\mathcal{V}^P_{\mathrm{HOM}}$
(i) Unbalanced Splitting Ratio	0.14 %
(ii) Classical Interference Contrast	0.99 %
(iii) Single-photon Purity	3.44 - 12.15 %

Table 5.1: Corrections to the HOM visibility by each of the three parameters. The range of the single-photon purity is calculated using the lowest(highest) value of $g^{(2)} = 0.0175$ ($g^{(2)} = 0.0647$), derived in previous section.

The intrinsic HOM visibility can therefore be expressed by

$$\mathcal{V}^I_{\mathrm{HOM}} = \frac{\mathcal{V}_{\mathrm{HOM}}}{\mathcal{V}^P_{\mathrm{HOM}}}, \tag{5.3.21}$$

correcting for the limitations and imperfections of the experimental setup. This relation can thus be utilized to evaluate the intrinsic indistinguishability of the photons emitted by the QD. From the single-photon purities derived in Eqs. 5.2.3 - 5.2.4 and the HOM visibilities from Eqs. 5.3.13 - 5.3.14, the intrinsic HOM visibilities for each sequence is

$$\text{(i) Sequence:} \quad \mathcal{V}^I_{\mathrm{HOM}} = 0.9500 \pm 0.0137, \tag{5.3.22}$$

$$\text{(ii) Sequence:} \quad \mathcal{V}^I_{\mathrm{HOM}} = 0.9371 \pm 0.0330, \tag{5.3.23}$$

for an integration window of 1.5 ns. Here, the single-photon purity in the middle time-bin is derived from the weighted average of $g_e^{(2)}(\tau = 0)$ and $g_l^{(2)}(\tau = 0)$. The same derivation is completed for the other integration windows, shown in Fig. 5.10. Ideally, the intrinsic HOM visibility should remain constant for all integration windows, which is true within the limit of the errorbars.

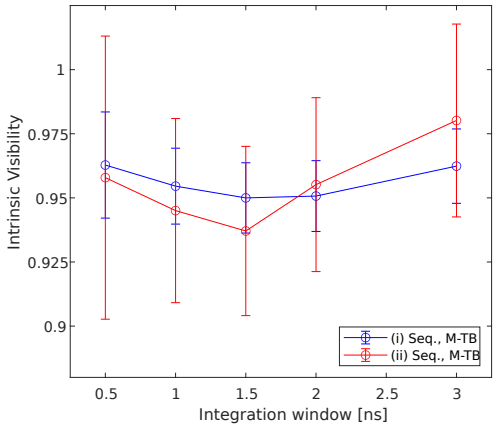

Figure 5.10: The intrinsic HOM visibility for both sequences as a function of the integration window of the middle time-bin.

Finally, a weighted average for each sequence, based on the visibilities presented in Fig. 5.10, yields

$$\text{(i) Sequence:} \quad \bar{\mathcal{V}}^I_{\mathrm{HOM}} = 0.9551 \pm 0.0067, \tag{5.3.24}$$

$$\text{(ii) Sequence:} \quad \bar{\mathcal{V}}^I_{\mathrm{HOM}} = 0.9535 \pm 0.0167, \tag{5.3.25}$$

which quantifies the indistinguishability of the emitted photons. These finding are also comparable with previous work, demonstrating an intrinsic visibility of $\mathcal{V} = 96 \pm 2\%$ [47]. As this point, the indistinguishability is primarily limited by the interaction between phonons and the QD, which is unavoidable due to the solid-state nature of the system. These processes are often occurring at timescales much faster than the radiative decay and are highly dependent on the temperature. Thus, going to lower cryogenic temperatures ($T < 4$ K) could potentially improved the indistinguishability, as the pure-dephasing processes induced by phonon-interactions are suppressed even further [5].

5.4 Summary

This chapter included an examination of the optical excitation pulse, having a central wavelength of $\lambda_C = 945.03$ nm with a 38.9 pm bandwidth. The latter corresponds to a pulse duration of $\Delta\mathcal{T} = 33.8$ ps, being an order of magnitude smaller than the radiative lifetime of the positive trion. Additionally, the rejection ratio between the two vertical transitions $|\Downarrow\rangle \rightarrow |\Uparrow\Downarrow, \downarrow\rangle$ and $|\Uparrow\rangle \rightarrow |\Uparrow\Downarrow, \uparrow\rangle$ was found to be $R_r = 15.2 \pm 2.6$, quantifying the ability to excite the correct transition, i.e. low-energy transition of the X^+.

Furthermore, the single-photon purity was examined using the early and late time-bins generated by the TBI, while the two-photon interference of the middle time-bin provided a method the investigate the indistinguishability. Both parameters were probed by two different excitation schemes, relying on the hole-spin being prepared directly through OSP or a combination of OSP and optical spin-rotations.
The single-photon purity was analysed by the second-order correlation function, demonstrating purities down to $g^{(2)}(0) = 0.0175 \pm 0.0033$, while the indistinguishability was quantified by the two-photon interference of the middle time-bin, yielding an average visibility of $\bar{\mathcal{V}}^I_{\mathrm{HOM}} = 95.51 \pm 0.67\%$ ($95.35 \pm 1.67\%$) for the (i) and (ii) sequence, respectively.

Chapter 6

Conclusion

In this thesis, the main ingredients towards spin-multiphoton entanglement has been presented, based on the interaction between time-bin encoded photonic qubits and a hole-spin residing in a solid-state quantum dot embedded in a photonic crystal waveguide.

The efficient integration between the positively charged trion X^+ and the photonic nanostructure has proven a promising system towards spin-photon entanglement, owing to the advantageous properties of the photonic environment, including an enhanced cyclicity of the optical transition addressed in this work [11]. Successful implementation of optical spin manipulation schemes such as optical spin pumping and coherent spin control through Raman transitions, make the two ground states $\{|\Downarrow\rangle, |\Uparrow\rangle\}$ of the X^+ ideal for realizing a "stationary" qubit.
The framework for generating and detecting time-bin encoded photonic qubits has been presented, employing the excitation- and detection-interferometer, respectively. By design, both interferometers share the same optical paths, making the Time-bin Interferometer self-stabilizing and hence optimal for long measurement sequences. The principles behind passive- and active-switching has been studied, demonstrating the ability to efficiently scale the number of photonic qubits in each entanglement sequence. Consequently, the Time-bin Interferometer satisfies all the requirements towards a robust system, capable of creating and analyzing the "flying" qubits, based on the arrival time in the three time-bins $\{|e\rangle, |m\rangle, |l\rangle\}$.
A characterization of the single-photon emitter has been conducted, probing the nature of the photons utilized as photonic qubits. The single-photon purity was quantified through a second-order correlation measurement, examining the photon statistics in the early and late time-bins, yielding a purity of $g^{(2)}(0) = 0.0175 \pm 0.0033$. Additionally, the indistinguishability was measured by the two-photon interference in the middle time-bin, demonstrating an intrinsic visibility up to $\mathcal{V}_{\mathrm{HOM}} = 95.51 \pm 0.67$ %, making the quantum dot a source of high-quality photons.
In conclusion, this thesis has presented all the essential components to successfully implement the entanglement protocol generating multi-photon entangled states such as the GHZ- and Cluster-state.

Outlook

The current setup allows multiple photonic qubits to be projected into the x, y, or z-basis, which is sufficient to analyse the GHZ state and measure its fidelity (see Section 3.4). However, to characterize the Cluster states the measurement basis has to be switched between each subsequent photonic qubit, i.e. a measurement sequence like $\{\sigma_x^{(1)}, \sigma_z^{(2)}, \sigma_x^{(3)}, \sigma_z^{(4)}, ...\}$. Thus, in order to fully analyze the multi-photon Cluster state a second EOM should be implemented, which would allow one to switch projection basis from one photonic qubit to another. It should be noted, that only switching between z-basis *and* x- *or* y-basis is possible with an additional EOM. The current setup *cannot* switch between x- and y-basis for two subsequent photons, as these are defined by the waveplates of the excitation interferometer.

A further optimization of the single-photon purity and indistinguishability would potentially increase the fidelity of the multi-photon states. As mentioned in the final paragraph of Section 5.3.1, the indistinguishability is mainly limited by phonon interactions. Thus, cooling the sample to lower cryogenic temperatures would strongly suppress the latter. Reducing the impurity or possible re-excitation errors can enhance the single-photon purity, which may be achieved by modifying the spatial profile or altering the duration of the excitation pulse. Additionally, high photon transmission and detection efficiencies is crucial towards deterministic multi-photon entanglement generation. However, the efficiency of the setup is strongly limited by the collection optics. Further improvements might include a one-sided photonic crystal waveguide which would double the current collection efficiency.

While this thesis was written, indications of the spin-photon entanglement has been demonstrated, using the Time-bin Interferometer and the spin-photon interface presented in this work. These measurements were conducted under passive switching and hence no EOM was utilized to modulate the polarization of the incident photons of the detection interferometer. Increasing the number of photons will inevitably require the implementation of the active switching scheme, as it enhances the probability of projecting the multi-photon states into the right bases (see final section of Chapter 4).
Consequently, additional spin-photon entanglement experiments will reveal how far this protocol may be extended and it will be truly interesting to see the number of entangled photons one can generate using the experimental setup presented in this thesis.

Bibliography

[1] T. Ladd, F. Jelezko, R. Laflamme, Y. Nakamura, C. Monroe, and J. L. O'Brien, "Quantum computers," *Nature*, vol. 464, pp. 45–53, 2010.

[2] C. H. Bennett and G. Brassard, "Quantum cryptography: Public key distribution and coin tossing," *Theoretical Computer Science*, vol. 560, pp. 7–11, 2014.

[3] L. K. Grover, "A fast quantum mechanical algorithm for database search," arXiv:quant-ph/9605043v3, pp. 1-8, 1996.

[4] S. M. Barnett, *Quantum Information*. Oxford University Press, 2009.

[5] P. Lodahl, S. Mahmoodian, and S. Stobbe, "Interfacing single photons and single quantum dots with photonic nanostructures," *Reviews of Modern Physics*, vol. 87, pp. 347–400, 2015.

[6] R. J. Warburton, "Single spins in self-assembled quantum dots," *Nature materials*, vol. 12, pp. 483–493, 2013.

[7] R. Uppu, F. T. Pedersen, Y. Wang, C. T. Olesen, C. Papon, X. Zhou, L. Midolo, S. Scholz, A. D. Wieck, A. Ludwig, and P. Lodahl, "Scalable integrated single-photon source," *arXiv:2003.08919*, pp. 1–17, 2020.

[8] O. Gywat, H. J. Krenner, and J. Berezovsky, *Spins in Optically Active Quantum Dots*, First Edition. Wiley, 2010.

[9] A. Javadi, *Quantum electrodynamics with 1D artificial atoms: from Purcell enhancement to single-photon nonlinearities*, Ph.D. Thesis. University of Copenhagen, 2015.

[10] P. A. Dalgarno, J. M. Smith, J. McFarlane, B. D. Gerardot, K. Karrai, A. Badolato, P. M. Petroff, and R. J. Warburton, "Coulomb interactions in single charged self-assembled quantum dots: Radiative lifetime and recombination energy," *Physical Review B - Condensed Matter and Materials Physics*, vol. 77, 2008.

[11] M. H. Appel, A. Tiranov, A. Javadi, M. C. Löbl, Y. Wang, S. Scholz, A. D. Wieck, A. Ludwig, R. J. Warburton, and P. Lodahl, "Coherent spin-photon interface with waveguide induced cycling transitions," *Physical Review Letters*, vol. 126, 2021.

[12] L. A. Coldren, S. W. Corzine, and M. L. Masanovic, *Diode Lasers and Photonic Integrated Circuits*, Second Edition. John Wiley & Sons, 2012.

[13] J. Dreiser, M. Atatüre, C. Galland, T. Müller, A. Badolato, and A. Imamoglu, "Optical investigations of quantum dot spin dynamics as a function of external electric and magnetic fields," *Physical Review B - Condensed Matter and Materials Physics*, vol. 77, 2008.

[14] E. Rosencher and B. Vinter, *Optoelectronics*, English Edition. Cambridge University Press, 2004.

[15] M. Arcari, I. Söllner, A. Javadi, S. Lindskov Hansen, S. Mahmoodian, J. Liu, H. Thyrrestrup, E. H. Lee, J. D. Song, S. Stobbe, and P. Lodahl, "Near-unity coupling efficiency of a quantum emitter to a photonic crystal waveguide," *Physical Review Letters*, vol. 113, 2014.

[16] Attocube, *Attodry1000*, Website: `https://www.attocube.com/application/files/7115/5360/6799/attoDRY.pdf`, Accessed: December, 2020.

[17] D. A. Steck, *Quantum and Atom Optics*, Department of Physics, University of Oregon. Lecture Notes: `https://atomoptics-nas.uoregon.edu/~dsteck/teaching/quantum-optics/`, 2019.

[18] J. H. Bodey, R. Stockill, E. V. Denning, D. A. Gangloff, G. Éthier-Majcher, D. M. Jackson, E. Clarke, M. Hugues, C. L. Gall, and M. Atatüre, "Optical spin locking of a solid-state qubit," *Quantum Information*, vol. 5, 2019.

[19] E. Schrödinger, "Discussion of probability relations between separated systems," *Cambridge Philosophical Society*, vol. 31, pp. 555–563, 1935.

[20] M. A. Nielsen and I. L. Chuang, *Quantum Computation and Quantum Information*, 10th Anniversary Edition. Cambridge University Press, 2010.

[21] J. Preskill, *Quantum Information - Chapter 2*, California Institute of Technology. Lecture Notes for Ph219/CS219, 2015.

[22] C. H. Bennett and S. J. Wiesner, "Communication via one- and two-particle operators on einstein-podolsky-rosen states," *Physical Review Letters*, vol. 69, no. 20, pp. 2281–2884, 1992.

[23] K. Mattle, H. Weinfurter, P. G. Kwiat, and A. Zeilinger, "Dense coding in experimental quantum communication," *Physical Review Letters*, vol. 76, no. 25, pp. 4656–4659, 1996.

[24] C. H. Bennett, G. Brassard, C. Crépeau, R. Jozsa, A. Peres, and W. K. Wootters, "Teleporting an unknown quantum state via dual classical and einstein-podolsky-rosen channels," *Physical Review Letters*, vol. 70, no. 13, pp. 1895–1899, 1993.

[25] N. Gisin, G. Ribordy, W. Tittel, and H. Zbinden, "Quantum cryptography," *Reviews of Modern Physics*, vol. 74, pp. 145–195, 2002.

[26] O. Gühne, *Detecting Quantum Entanglement: Entanglement Witnesses and Uncertainty Relations*, Ph.D. Thesis. University of Hannover, 2004.

[27] Y. Yeo and W. K. Chua, "Teleportation and dense coding with genuine multipartite entanglement," *Physical Review Letters*, vol. 96, p. 060 502, 2006.

[28] J. F. Haase, A. Smirne, J. Kolodyński, R. Demkowicz-Dobrzański, and S. F. Huelga, "Precision limits in quantum metrology with open quantum systems," *arXiv:1807.11882v4*, 2018.

[29] R. Raussendorf, D. E. Browne, and H. J. Briegel, "Measurement-based quantum computation on cluster states," *Physical Review A*, vol. 68, 2003.

[30] H. J. Briegel, D. E. Browne, W. Dür, R. Raussendorf, and M. Van Den Nest, "Measurement-based quantum computation," *Nature Physics*, vol. 5, pp. 19–36, 2009.

[31] H. J. Briegel and R. Raussendorf, "Persistent entanglement in arrays of interacting particles," *Physical Review Letters*, vol. 86, pp. 910–913, 2001.

[32] K. Tiurev, P. L. Mirambell, M. B. Lauritzen, M. H. Appel, A. Tiranov, P. Lodahl, and A. S. Sørensen, "Fidelity of time-bin entangled multi-photon states from a quantum emitter," arXiv:2007.09298v3, pp. 1-21, 2020.

[33] N. H. Lindner and T. Rudolph, "Proposal for pulsed on-demand sources of photonic cluster state strings," *Physical Review Letters*, vol. 103, 2009.

[34] G. Tóth and O. Gühne, "Entanglement detection," *arXiv:0811.2803v3*, 2009.

[35] O. Gühne, C.-Y. Lu, W.-B. Gao, and J.-W. Pan, "Toolbox for entanglement detection and fidelity estimation," arXiv:0706.2432v3, pp. 1-5, 2018.

[36] L.-K. Chen, Z.-D. Li, X.-C. Yao, *et al.*, "Observation of ten-photon entanglement using thin BiB3O6 crystals," *Optica*, vol. 4, pp. 77–83, 2017.

[37] H.-S. Zhong, Y. Li, W. Li, *et al.*, "12-photon entanglement and scalable scattershot boson sampling with optimal entangled-photon pairs from parametric down-conversion," *Physical Review Letters*, vol. 121, p. 250 505, 2018.

[38] G. Tóth and O. Gühne, "Detecting genuine multipartite entanglement with two local measurements," *Physical Review Letters*, vol. 94, p. 060 501, 2005.

[39] K. Tiurev *et al.*, "To be published," 2021.

[40] R. Uppu, T. A. W. Wolterink, T. B. H. Tentrup, and P. W. H. Pinkse, "Quantum optics of lossy asymmetric beam splitters," *Optics Express*, vol. 24, no. 15, pp. 16 440–16 449, 2016.

[41] Thorlabs, *Electro-Optic Modulator*, Website: `https://www.thorlabs.com/newgrouppage9.cfm?objectgroup_id=2729`, Accessed: November, 2020.

[42] QUBIG, *Free Space Resonant EOM*, Website: `https://www.qubig.com/products/electro-optic-modulators-230/amplitude-modulators/am8-nir.html`, Accessed: December, 2020.

[43] SwabianInstruments, *Swabian Time Tagger*, Website: `https://www.swabianinstruments.com/time-tagger/`, Accessed: January, 2021.

[44] Coherent, *Mira 900*, Website: `https://www.coherent.com/lasers/laser/mira-900`, Accessed: January, 2021.

[45] C. Gerry and P. Knight, *Introductory Quantum Optics*. Cambridge University Press, 2004.

[46] R. Hanbury Brown and R. Q. Twiss, "Correlation between photons in two coherent beams of light," *Nature*, vol. 117, pp. 27–29, 1956.

[47] R. Uppu, F. T. Pedersen, Y. Wang, C. T. Olesen, C. Papon, X. Zhou, L. Midolo, S. Scholz, A. D. Wieck, A. Ludwig, and P. Lodahl, "Scalable integrated single-photon source," *Science Advances*, vol. 6, 2020.

[48] S. Kako, C. Santori, K. Hoshino, S. Götzinger, Y. Yamamoto, and Y. Arakawa, "A gallium nitride single-photon source operating at 200k," *Nature Materials*, vol. 5, pp. 887–892, 2006.

[49] C. K. Hong, Z. Y. Ou, and L. Mandel, "Measurement of subpicosecond time intervals between two photons by interference," *Physical Review Letters*, vol. 59, no. 18, pp. 2044–2046, 1987.

[50] F. Bouchard, A. Sit, Y. Zhang, R. Fickler, F. M. Miatto, Y. Yao, F. Sciarrino, and E. Karimi, "Two-photon interference: The Hong-Ou-Mandel effect," *arXiv:2006.09335v1*, pp. 1–21, 2020.

[51] C. Santori, D. Fattal, J. Vučković, G. S. Solomon, and Y. Yamamoto, "Indistinguishable photons from a single-photon device," *Nature*, vol. 419, pp. 594–597, 2002.

Appendix A

Entangled Quantum States

A.1 The Bell States

Through the derivation of the density matrix and the reduced density matrix, it can be shown that the Bell states are in fact maximally entangled and pure. As an example, consider the following Bell state compose of subsystem A and B

$$\left|\Phi^+\right\rangle_{AB} = \frac{1}{\sqrt{2}}\left(|0_A 0_B\rangle + |1_A 1_B\rangle\right), \tag{A.1.1}$$

in which case the density matrix takes the form (omitting the A and B labels)

$$\begin{aligned}
\rho_{\Phi^+} &= \left|\Phi^+\right\rangle\left\langle\Phi^+\right| && \text{(A.1.2)}\\
&= \frac{1}{2}\left(|00\rangle\langle 00| + |00\rangle\langle 11| + |11\rangle\langle 00| + |11\rangle\langle 11|\right) && \text{(A.1.3)}\\
&= \frac{1}{2}\begin{pmatrix} 1 & 0 & 0 & 1 \\ 0 & 0 & 0 & 0 \\ 0 & 0 & 0 & 0 \\ 1 & 0 & 0 & 1 \end{pmatrix}, && \text{(A.1.4)}
\end{aligned}$$

where each qubit are represented by the two-dimensional basis $\{|0\rangle, |1\rangle\}$, whereas the basis for the matrix representation is given by $\{|00\rangle, |01\rangle, |10\rangle, |11\rangle\}$. The reduced density matrix for subsystem A can be now be derived, using Eq. 3.1.4

$$\begin{aligned}
\rho_A &= \sum_{j=1}^{2}\left(I_a \otimes \langle b_j|\right)\rho_{\Phi^+}\left(I_a \otimes |b_j\rangle\right) && \text{(A.1.5)}\\
&= \frac{1}{2}\begin{pmatrix} 1 & 0 \\ 0 & 1 \end{pmatrix}. && \text{(A.1.6)}
\end{aligned}$$

Thus, the corresponding Bell state is in fact a pure maximally entangled state, as $\mathrm{Tr}[\rho^2_{\Phi^+}] = 1$ and $\rho_A = \frac{1}{2}I$, while the subsystem is a maximally mixed state. It goes without saying, that this derivation can be carried out for all the remaining Bell states, giving the same result.

Appendix B

Time-bin Interferometer

B.1 Full Overview of Experimental Setup

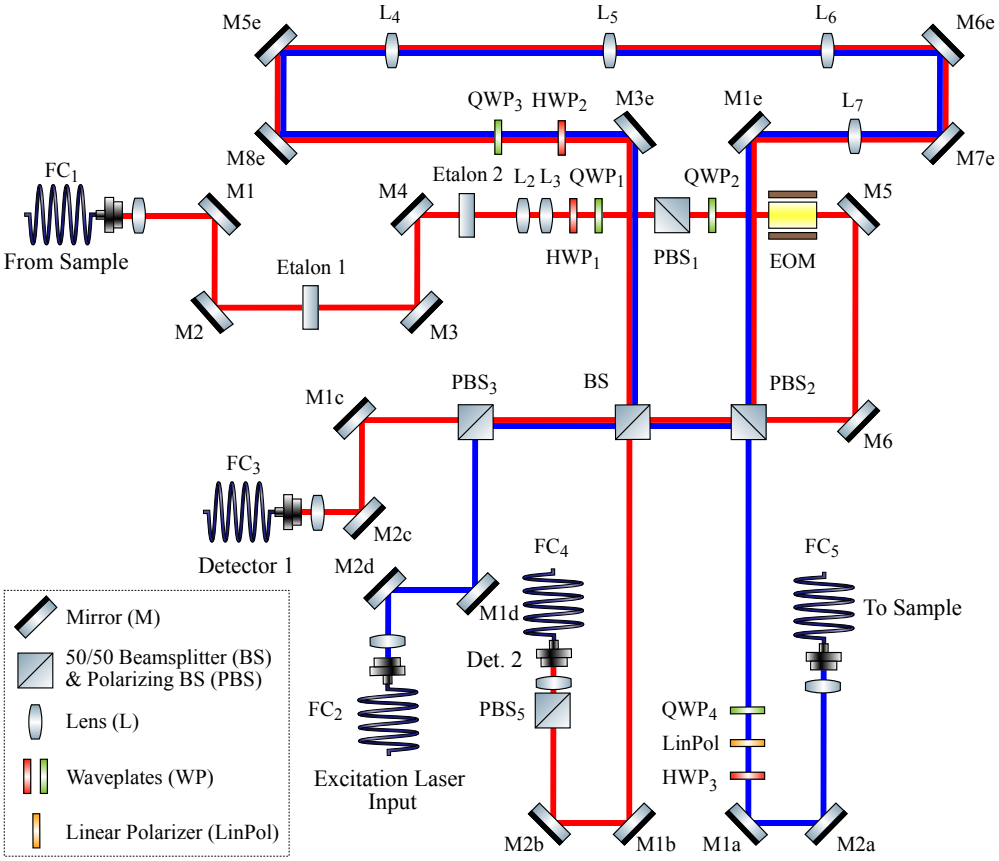

Figure B.1: Schematic drawing of the Time-bin Interferometer for generation and detection of early and late pulses given a single pulse input. The blue(red) lines represent the excitation(detection) path starting at fiber coupler FC_2(FC_1). The excitation path ends at FC_5 going to the sample, while the detection path goes to Detector 1 or 2, i.e. FC_3 or FC_4. Short and long path are defined as the distance between BS and PBS_2.

B.2 Derivation of QWP-EOM Transformation

Crucial for the analysis of the detection interferometer is the QWP-EOM transformation, which enables the passive/active switching of the measurements basis for the photonic qubits. The following derivation is based on Eqs. 4.1.4 and 4.1.8, describing the Jones matrix for the QWP and EOM, respectively.

The total transformation of horizontally polarized light due to a QWP and EOM reads

$$M_{\mathrm{EQ}}(\Phi,\theta)\vec{E}_H = M_{\mathrm{EOM}}(\Phi)M_{\mathrm{QWP}}(\theta)\begin{bmatrix}1\\0\end{bmatrix} \tag{B.2.1}$$

$$= \frac{e^{i(\pi/4-\Phi)}}{\sqrt{2}}\begin{bmatrix}(1-i\cos(2\theta))\cos(\Phi/2)+\sin(2\theta)\sin(\Phi/2)\\(i+\cos(2\theta))\sin(\Phi/2)-i\sin(2\theta)\cos(\Phi/2)\end{bmatrix}, \tag{B.2.2}$$

which is the case in this particular setup, as the input will be horizontally polarized due to PBS_1. For vertically polarized light however, the following transformation occurs

$$M_{\mathrm{EQ}}(\Phi,\theta)\vec{E}_V = M_{\mathrm{EOM}}(\Phi)M_{\mathrm{QWP}}(\theta)\begin{bmatrix}0\\1\end{bmatrix} \tag{B.2.3}$$

$$= \frac{e^{i(\pi/4-\Phi)}}{\sqrt{2}}\begin{bmatrix}(i-\cos(2\theta))\sin(\Phi/2)-i\cos(\Phi/2)\sin(2\theta)\\(1+i\cos(2\theta))\cos(\Phi/2)+\sin(2\theta)\sin(\Phi/2)\end{bmatrix}. \tag{B.2.4}$$

Extending this formalism to the four-dimensional vector space introduced by Eq. 4.1.7, the matrix accounting for the QWP and EOM given an arbitrary polarization takes the form

$$M_{\mathrm{EQ}}(\Phi_{\{e,l\}},\theta) = \begin{bmatrix} C(\Phi_e)c_{HH}(\theta,\Phi_e) & 0 & C(\Phi_e)c_{VH}(\theta,\Phi_e) & 0\\ 0 & C(\Phi_l)c_{HH}(\theta,\Phi_l) & 0 & C(\Phi_l)c_{VH}(\theta,\Phi_l)\\ C(\Phi_e)c_{HV}(\theta,\Phi_e) & 0 & C(\Phi_e)c_{VV}(\theta,\Phi_e) & 0\\ 0 & C(\Phi_l)c_{HV}(\theta,\Phi_l) & 0 & C(\Phi_l)c_{VV}(\theta,\Phi_l)\end{bmatrix}, \tag{B.2.5}$$

where the coefficients express the degree of polarization-transformation performed by this ensemble

$$C(\Phi) = \frac{e^{i(\pi/4-\Phi)}}{\sqrt{2}}, \tag{B.2.6}$$

$$c_{HH}(\theta,\Phi) = (1-i\cos(2\theta))\cos(\Phi/2)+\sin(2\theta)\sin(\Phi/2), \tag{B.2.7}$$

$$c_{HV}(\theta,\Phi) = (i+\cos(2\theta))\sin(\Phi/2)-i\sin(2\theta)\cos(\Phi/2), \tag{B.2.8}$$

$$c_{VH}(\theta,\Phi) = (i-\cos(2\theta))\sin(\Phi/2)-i\sin(2\theta)\cos(\Phi/2), \tag{B.2.9}$$

$$c_{VV}(\theta,\Phi) = (1+i\cos(2\theta))\cos(\Phi/2)+\sin(2\theta)\sin(\Phi/2). \tag{B.2.10}$$

In order to keep track of the temporal modes, $\Phi_{\{e,l\}}$ denotes the retardation between the fast and slow axis of the EOM at the time of the early and late mode, while θ corresponds to the rotation of the QWP_2.

B.3 Photon Detection Probabilities

The following figures show the relative detection probabilities for a photon in either Detector 1 (D_1) or Detector 2 (D_2) in the three time-bins $\{|e\rangle, |m\rangle, |l\rangle\}$, as a function of QWP_4 and LP in the excitation interferometer. Section B.3.1 and B.3.2 presents the theoretical model for active switching, while Section B.3.3 and B.3.4 shows a measurement using the EOM for photon routing.

B.3.1 Theoretical Model for Active Switching in x- or y-basis

The probabilities derived in Eqs. 4.3.26 - 4.3.29 at the end of Section 4.3.1 are shown in Fig. B.2. Ideally, photons should only be routed towards the middle time-bin. However, as this model includes the relative losses and imperfections, where will be a small probability of photon detection in the early time-bin. The late time-bin is not included, as it is zero for all combinations of θ_{QWP} and θ_{LP}. Note, the probabilities shown in Fig. B.2 are normalized, such that each waveplate setting yields unity probability.

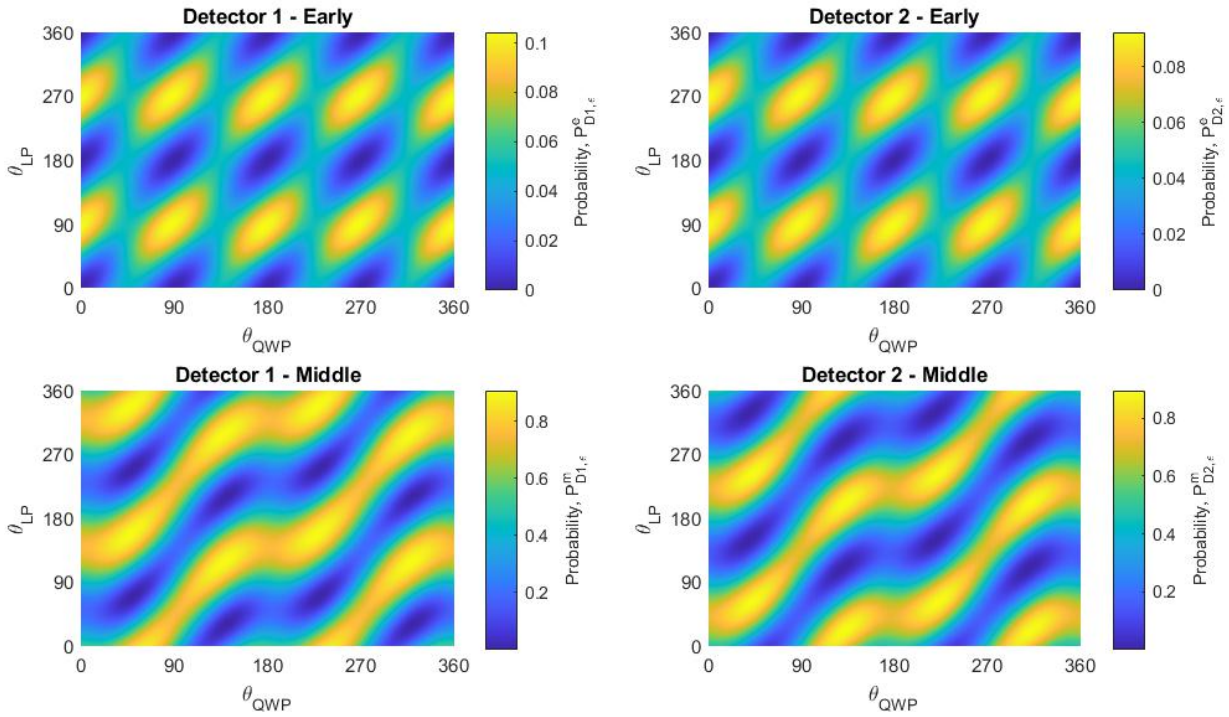

Figure B.2: Theoretical Model: The normalized probability of photon detection in D_1 and D_2 as a function of θ_{QWP} and θ_{LP} for active switching using the x- or y-basis settings. Note the different scaling of the colorbars. Imperfections: $\eta_{S1} = 0.84$, $\eta_{S2} = 0.79$, $\eta_{L1} = 0.81$, $\eta_{L2} = 0.76$, $\epsilon = 0.72$ and $\chi = \chi' = 0$.

B.3.2 Theoretical Model for Active Switching in z-basis

Figure B.3 presents the probabilities derived in Eqs. 4.3.32 - 4.3.34 at the end of Section 4.3.1. Ideally, photons should only be routed towards the early and late time-bin. However, as this model includes the relative losses and the imperfection of the EOM, where will be a small probability of photon detection in the middle time-bin. In contrast to Fig. B.2, the same detection pattern emerges for all detectors and time-bins.

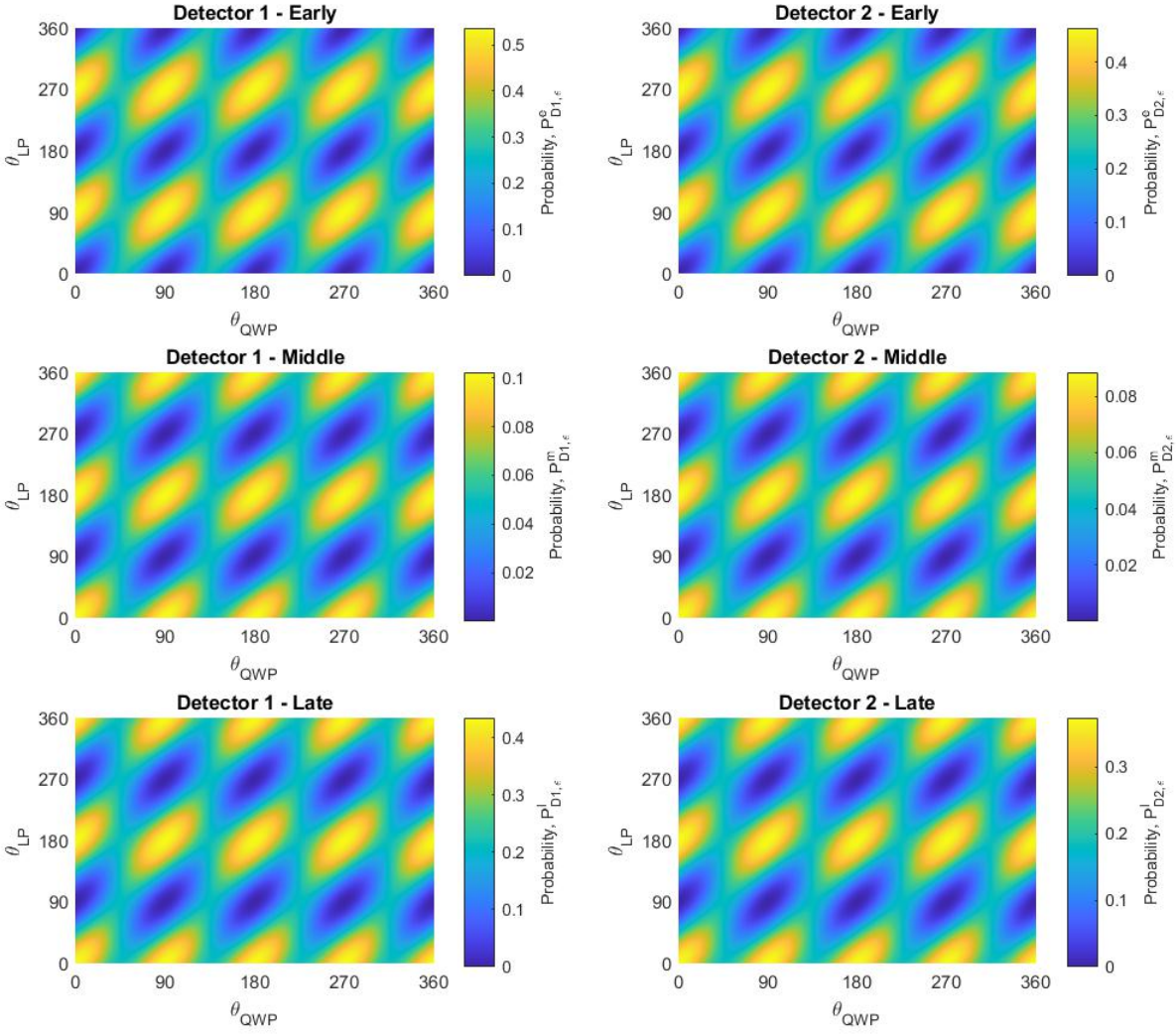

Figure B.3: Theoretical Model: The normalized probability of photon detection in D_1 and D_2 as a function of θ_{QWP} and θ_{LP} for active switching using the z-basis settings. Note the different scaling of the colorbars. Imperfections: $\eta_{S1} = 0.84$, $\eta_{S2} = 0.79$, $\eta_{L1} = 0.81$, $\eta_{L2} = 0.76$, $\epsilon = 0.72$ and $\chi = \chi' = 0$.

B.3.3 Experimental Data for Active Switching in x- or y-basis

Figure B.4 presents a measurement showing the detection probabilities in the x- or y-basis as a function of θ_{QWP} and θ_{LP}.
In comparison with the theoretical model in Fig. B.2, the two detection patterns are similar in appearance. Especially the late time-bin corresponds very well with the model, predicting a probability of zero. Furthermore, the wave-like appearance of the middle time-bin is a direct consequence of the finite extinction ratio of the EOM, which in the model takes the form of the ϵ-parameter.

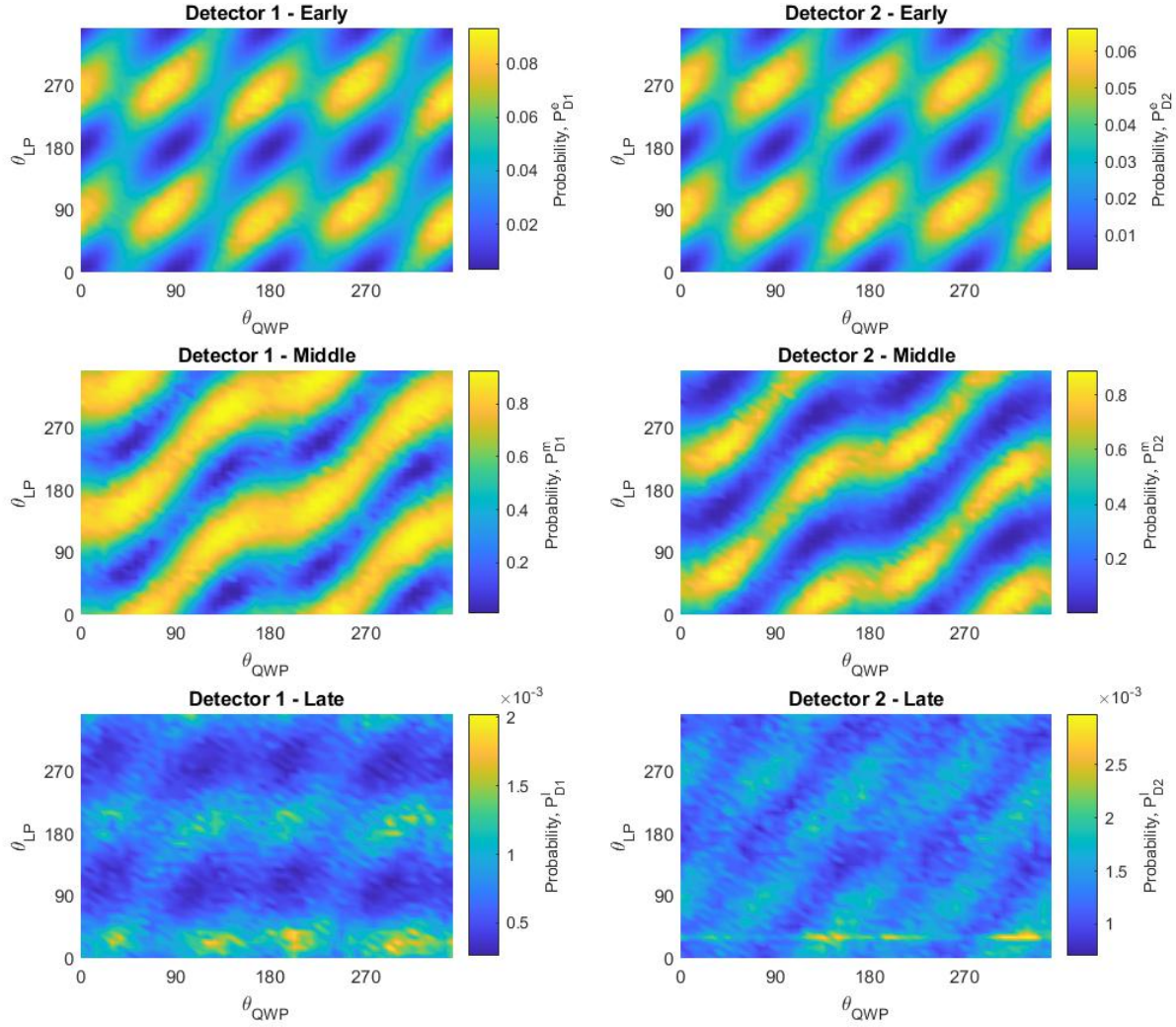

Figure B.4: Experimental Data: The normalized probability of photon detection in D_1 and D_2 as a function of θ_{QWP} and θ_{LP} for active switching using the x- or y-basis settings. Note the different scaling of the colorbars. The relative losses and coupling efficiencies are given by the η_{ij}-parameter: $\eta_{S1} = 0.84$, $\eta_{S2} = 0.79$, $\eta_{L1} = 0.81$, $\eta_{L2} = 0.76$.

B.3.4 Experimental Data for Active Switching in z-basis

Figure B.5 presents a measurement showing detection probabilities in the z-basis as a function of θ_{QWP} and θ_{LP}. The dot-shaped pattern shows agreement between the experimental setup and the theoretical model. The probability in Detector 1 is generally larger due to better coupling efficiency, while the same is true for the early time-bins due to fewer optical components in the short interferometer path.

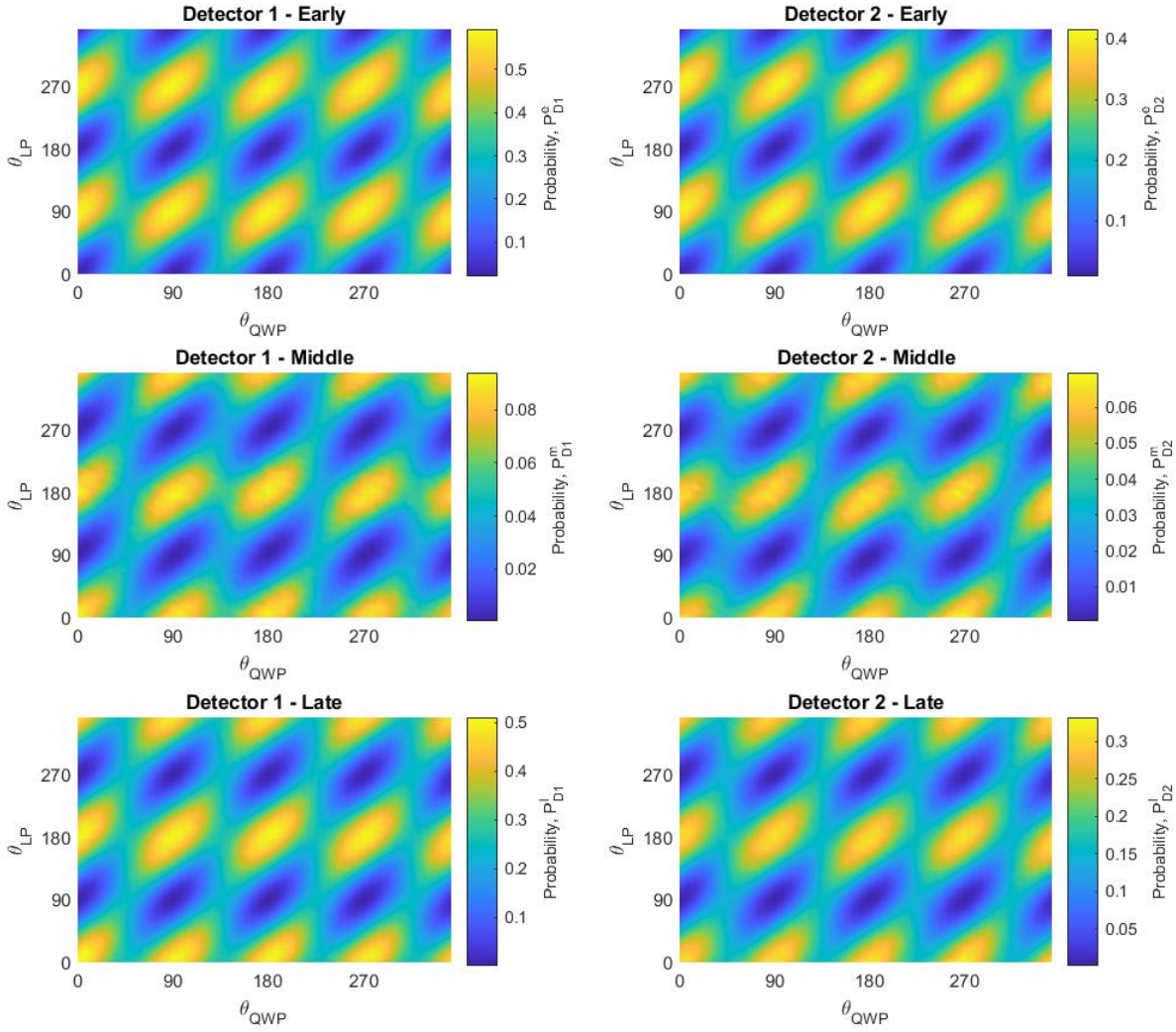

Figure B.5: Experimental Data: The normalized probability of photon detection in D_1 and D_2 as a function of θ_{QWP} and θ_{LP} for active switching using the z-basis settings. Note the different scaling of the colorbars. The relative losses and coupling efficiencies are given by the η_{ij}-parameter: $\eta_{S1} = 0.84$, $\eta_{S2} = 0.79$, $\eta_{L1} = 0.81$, $\eta_{L2} = 0.76$.

Appendix C

Experimental Equipment

This appendix seeks to give a brief introduction to some of the optical components and devices presented in this work.

C.1 Lasers

A total of four lasers are employed in this work, each utilized for the realization of the entanglement protocol. In Table C.1 a list of these lasers are presented, along with its properties.

Types of Lasers	Central Wavelength/Frequency	Duration	Applied for
Laser Diode	830.00 nm (361.20 THz)	100 ns	Above-Band Excitation
DL-Pro	945.03 nm (317.23 THz)	200 ns	Optical Spin Pumping
CTL	$\Delta \approx 260$ GHz	tens of ns	Spin Rotation
Mira	945.03 nm (317.23 THz)	tens of ps	Optical Excitation

Table C.1: List of lasers and their applications for the entanglement sequence. Here Δ denotes the detuning from the central frequency.

- The Laser Diode: The laser diode or the above-band laser has a central wavelength fixed at 830 nm, and is only used for above-band excitation of the QD, hence the name.
- The DL-Pro: Tunable Diode Laser from Toptica Photonics. Wavelength ranging from 915-985 nm. Utilized for OSP around a central wavelength of 945.03 nm.
- The CTL: The Continuous Tuneable Laser (CTL) has a range of 915-985 nm with a narrow bandwidth. Utilized for spin-rotations in the entanglement protocol, and hence detuned from the resonance frequency.
- The Mira-Laser: The Mira 900 Ti:sapphire laser, enables the emission of ultra-short pulses at a wavelength of approximately 700-1000 nm [44]. The central wavelength, used for optical excitation, is adjusted to 945.03 nm, while the pulse repetition rate is $f_{rep} \approx 72$ MHz.

C.2 Etalons

Two etalons (ET_1 and ET_2) are placed at the input of the detection interferometer. If mounted correctly, each etalon allows narrow frequency filtering with a bandwidth of 3 GHz. A temperature controller is attached to both devices, whereby the central frequency of transmission can be adjust by modulating the temperature. The goal is thus to match the central frequency of both etalons with the resonant frequency of the low energy transition of the QD, i.e $|\Uparrow\rangle \leftrightarrow |\Uparrow\Downarrow, \uparrow\rangle$. Using two etalons allows for an even narrower filter, whereby most unwanted light is blocked, i.e. reflections and emissions from non-resonant transitions. The transition spectra of the first etalon is shown Fig. C.1, fitted with a lorentzian curve (black). Furthermore, the combination of both the first and second etalon is presented as well (red). The central frequency and FWHM are summarized in Table C.2, revealing a FWHM of 1.91 GHz for two etalons in series.

Etalons	Central Frequency	FWHM
ET_1	317.2365 THz	3.11 GHz
ET_1 + ET_2	317.2365 THz	1.91 GHz

Table C.2: Properties of the two etalons. Note: The central frequency of transmission is slightly higher than the 317.23 THz as previously stated. Experimentally, is was found that a higher bias voltage (resulting in a higher frequency) improved the spin-initialization.

However, placing multiple etalons will contribute to the overall losses of the system, as some fraction will not be transmitted. The efficiency of each etalon can be derived by comparing the intensity in front and after each device. Using a powermeter, the first etalon (second etalon) was found to have an efficiency of 92.8 % (97.1 %), given a total efficiency of 90%.

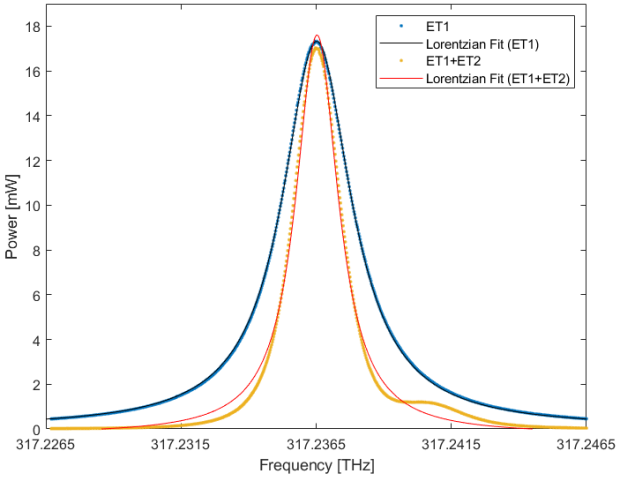

Figure C.1: Characterization of the two etalons ET_1 and ET_2. Each dataset is fitted with a lorentzian curve, giving a central frequency and a FWHM. Putting two etalons in series narrows the FWHM to 1.91 GHZ, while the FWHM of the first etalon ET_1 is 3.11 GHz. The central frequency remains constant at 317.2365 THz for both cases.

C.3 Volume Bragg Grating

A Volume Bragg Grating (VBG) is a diffraction grating with a periodic modulation of the refractive index, see Fig. C.2. Dependent on the orientation of this device, it either transmits or reflects an incident beam if the Bragg's condition is meet

$$\lambda_B = 2\bar{n}\Lambda\cos(\theta + \phi), \tag{C.3.1}$$

where λ_B is the diffracted wavelength, $\bar{n}$ is the average refractive index of the material and Λ is the grating period [12]. Furthermore, θ is the angle between incident beam with respect to the normal of the entrance surface $\mathbf{N}$, while ϕ denotes the angle between the latter and the grating vector $\mathbf{g}$. The VBG works as either a transmission- or reflection-grating for $\phi = \pi/2$ and $\phi = 0$, respectively. The latter being the case in this work.
Consequently, altering the angle of θ tunes the central wavelength of the reflected light λ_B, i.e. one may selectively choose a particular wavelength from a broad spectrum.

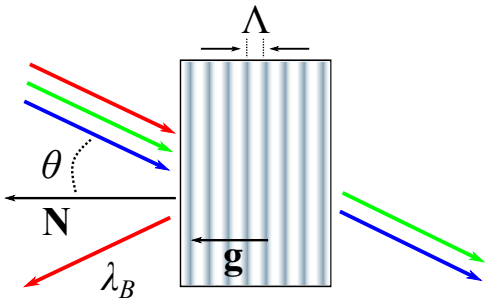

Figure C.2: Schematic drawing of a VBG for $\phi = 0$. The incident beam gets diffracted, reflecting and transmitting different wavelength dependent on the angle θ.

The VBG utilized is this work is manufactured by OptiGrate, promising an diffraction efficiency of 95% and a FWHM of 0.03 nm at a central wavelength of 956.039 nm.

C.4 Pulse Stretcher

The basic principle of the pulse stretcher can be understood by considering Fig. C.3. The incident beam propagates through a beam expander (BE) followed by a diffraction grating. The latter separates the beam into different wavelengths, which can be selected by the following slit. In other words, the position of the slit determines the central wavelength of the outgoing beam, while the slit-width alters the spectral bandwidth. Consequently, the temporal bandwidth of the outgoing pulse is stretched - hence the name.

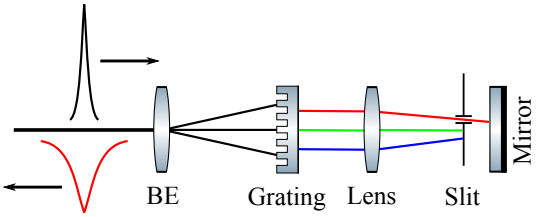

Figure C.3: Schematic drawing of the pulse stretcher.